ABSTRACT

GIBSON, NATHAN LOUIS Terahertz-Based Electromagnetic Interrogation Techniques for Damage Detection. (Under the direction of Professor H. Thomas Banks.)

We apply an inverse problem formulation to determine characteristics of a defect from a perturbed electromagnetic interrogating signal. A defect (gap) inside of a dielectric material causes a disruption, via reflections and refractions at the material interfaces, of the windowed interrogating signal. We model these electromagnetic waves inside the material with Maxwell's equations. In order to resolve the dimensions and location of the defect, we use simulations as forward solves in our Newton-based, iterative scheme which optimizes an innovative cost functional appropriate for reflected waves where phase differences can produce ill-posedness in the inverse problem when one uses the usual ordinary least squares criterion. Our choice of terahertz frequency allows good resolution of desired gap widths without significant attenuation. Numerical results are given in tables and plots, standard errors are calculated, and computational issues are addressed.

An inverse problem formulation is also developed for the determination of polarization parameters in heterogeneous Debye materials with multiple polarization mechanisms. For the case in which a distribution of mechanisms is present we show continuous dependence of the solutions on the probability distribution of polarization parameters in the sense of the Prohorov metric. This in turn implies well-posedness of the corresponding inverse problem, which we attempt to solve numerically for a simple uniform distribution. Lastly we address an alternate approach to modeling electromagnetic waves inside of materials with highly oscillating dielectric parameters which involves the technique of homogenization. We formulate our model in such a way that homogenization may be applied, and demonstrate the necessary equations to be solved.

Terahertz-Based Electromagnetic Interrogation Techniques for Damage Detection

by

Nathan Louis Gibson

A dissertation submitted to the Graduate Faculty of
North Carolina State University
in partial satisfaction of the
requirements for the Degree of
Doctor of Philosophy

Department of Mathematics

Raleigh

2004

Approved By:

Dr. Kazufumi Ito	Dr. Negash G. Medhin
Dr. H. Thomas Banks Chair of Advisory Committee	Dr. Hien T. Tran

Biography

Nathan Louis Gibson was born in Bowling Green, Kentucky on July 25, 1976. He graduated from Gallatin High School, Gallatin, Tennessee, in 1994. He received a Bachelor of Science degree with Distinction in Mathematics from Worcester Polytechnic Institute in 1998. In August 2001, he graduated from the University of Tennessee, Knoxville with a Master of Science degree in Applied Mathematics. He received his Doctorate in Philosophy in Computational Mathematics from North Carolina State University in August, 2004, and has accepted a National Institute of Aerospace post-doctoral position to continue research at the Center for Research in Scientific Computation.

Acknowledgements

I would like to most sincerely thank my adviser, Dr. H. T. Banks for invaluable professional and personal support throughout the development of this thesis. I also greatly appreciate the efforts of the other members of my committee: Dr. Hien T. Tran, Dr. Kazufumi Ito, and Dr. Negash G. Medhin. I am grateful to each of them for their interest in this research and their helpful suggestions.

This research would not have been possible without the guidance and expertise of Drs. William P. Winfree and Buzz Wincheski of NASA Langley Research Center, and the financial support of the NASA Graduate Student Researchers Program. Additionally, Dr. Richard Albanese of the Air Force Research Laboratory has provided helpful suggestions and insightful observations.

The continuous support and intellectual stimulation provided by the tight-knit group of researchers and staff in the Center for Research and Scientific Computation at NCSU has been integral to the success of this work. It would be easier to list the names of those members that I have not yet had the privilege of working with than to mention individually all that have helped me these past few years. I am grateful to each one, and look forward to continuing to work with each of them.

I am eternally indebted to my family and friends who have encouraged my aspirations, strengthened my resolve, supported my efforts, congratulated my accomplishments, and most recently, forgiven my lack of communication while I finished this work. Thank you to my mother for showing me the value of scholarship. Finally, I would like to recognize my grandfather, Charles Skaggs. Although he is no longer with us, his belief in me as a child gave me the enduring confidence to succeed.

Contents

List of Figures

List of Tables

Chapter 1

Introduction

Electromagnetic interrogation is a powerful method for non-destructive detection of damage inside of dielectric materials. The problem we consider is that of detecting a gap inside of a dielectric material using high frequency (terahertz) electromagnetic interrogation.

The idea is to observe the reflected and/or transmitted signals and use this data in an inverse problem formulation to determine certain characteristics of the gap, e.g., width and/or location inside the material. Possible applications of this procedure include quality assurance in fabrication of critical dielectric materials, or damage detection in aging materials for safety concerns. Further applications of electromagnetic interrogation, as well as additional problem formulations and solutions, can be found in [BBL00].

The particular motivation for this research is the detection of defects in the insulating foam on the fuel tanks of the space shuttles in order to help eliminate the separation of foam during shuttle ascent. There are two distinct types of damage that are of importance: gaps that form in the interior of the foam, or "voids", and "delamination", or separation of the foam from the aluminum fuel tank (see Figure 1.1).

For the latter, we address the problem of detecting a gap formed between a dielectric medium and a supra-conducting backing representing the foam and the metallic tank, respectively. However, first we develop our methodology on the slightly simpler problem of a gap formed in the interior of the foam, where for simplicity, we ignore the reflections from the back boundary (i.e., we impose absorbing boundary conditions instead). We also allow for the possibility in this case that the foam has been removed for testing, and therefore we

are able to place sensors both on the front and back sides of the foam.

To be applicable to real world problems we must eventually be able to solve these inverse problems with length scales on the order of $20cm$ for the thickness of the foam, $.2mm$ for the width of the gap, and a wavelength of about $3mm$. This wavelength corresponds to a frequency of $100GHz$, which is the lower end of the terahertz frequency range ($.1 \sim 10 \times 10^{12} Hz$). The rationale for using this choice of frequency is that higher frequencies are significantly attenuated in the materials which we are interested in interrogating. Furthermore, lower frequencies (larger wavelengths) have less resolution in detecting small gaps, and are less capable of sharply distinguishing between air and foam which may have a high air content.

Recent advances in terahertz generation and detection technologies have allowed the realization of practical and efficient applications of this unique frequency band (for more information, see [M03]). However, numerical techniques for specifically treating wavelengths of this size have yet to be developed. In particular, computing inside a large domain while needing to resolve a small wavelength results in a very large discretized problem. Therefore, in order to solve these problems here efficiently, we make certain simplifying assumptions. First we consider our pulsed interrogating signal to be linearly polarized, and exactly incident upon the material and the metallic backing, which reduces the problem to one spatial dimension. We model the electric field inside the material with the standard Maxwell's equations. However, as a preliminary approach leading to a proof of concept for this method, we model the polarization inside the dielectric material as if it were a simple Debye medium, with relaxation time τ. Lastly, for simplicity, we assume the region outside of the material, including inside the gap, may be sufficiently modeled as a vacuum.

We may then define an inverse problem for determining the gap's dimensions. We assume that we have data from sensors, located in front of and/or behind the material, that record the electromagnetic signal after it is reflected from (or passes through) the material. The gap inside the material causes disruptions, via reflections and refractions at the material interfaces, of the windowed interrogating signal. By solving our mathematical model, we compute simulated signals using approximations to the gap's characteristics. Then we apply an optimization routine to a modified least squares error between these simulated signals and the given data. Thus the optimization routine finds those gap characteristics which generate a simulated signal that most closely matches the given data. In this sense we determined an estimate to the "true" gap characteristics.

The bulk of this research explores the feasibility of this geometric inverse problem, including understanding the effects that random observation noise, both relative and constant variance, has on the confidence of our solutions. Some detail of the numerical methods used is provided, and when appropriate, justification for our choice of methods. However, in the interest of addressing the real life application, we begin to explore more realistic modeling approaches that can eventually be integrated into this geometric inverse problem formulation.

One of the more obvious oversimplifications we have assumed is the homogeneity of the dielectric material. In actuality, the insulating foam under consideration is comprised of at least two distinct substances (e.g., polyurethane and freon), presumably with very different dielectric parameters and generally in unknown volume distributions. We discuss two modeling approaches to deal with heterogeneous materials: homogenization and distributions of parameters. With respect to the former, Chapter 6 studies the behavior of the electromagnetic field in a material presenting heterogeneous microstructures which are described by spatially periodic parameters. We replace such a material by a new material characterized by homogeneous parameters. Regarding the distributions of parameters, Chapter 3 demonstrates with examples the necessity in some cases of multiple polarization parameters (i.e., a discrete distribution with multiple atoms), specifically multiple relaxation times for a heterogeneous Debye medium.

The use of distributions of polarization parameters is further explored in the context of a parameter identification problem. In particular, 4 demonstrate the well-posedness of the inverse problem involving a general polarization term which includes uncertainty in the dielectric parameters. Using the theory as a basis for our computational method, we solve several examples of the parameter identification problem in the context of a Debye polarization model in Chapter 5. In these examples we use a discrete distribution with two atoms, as it most directly pertains to our problem at hand, as well as a simple uniform distribution.

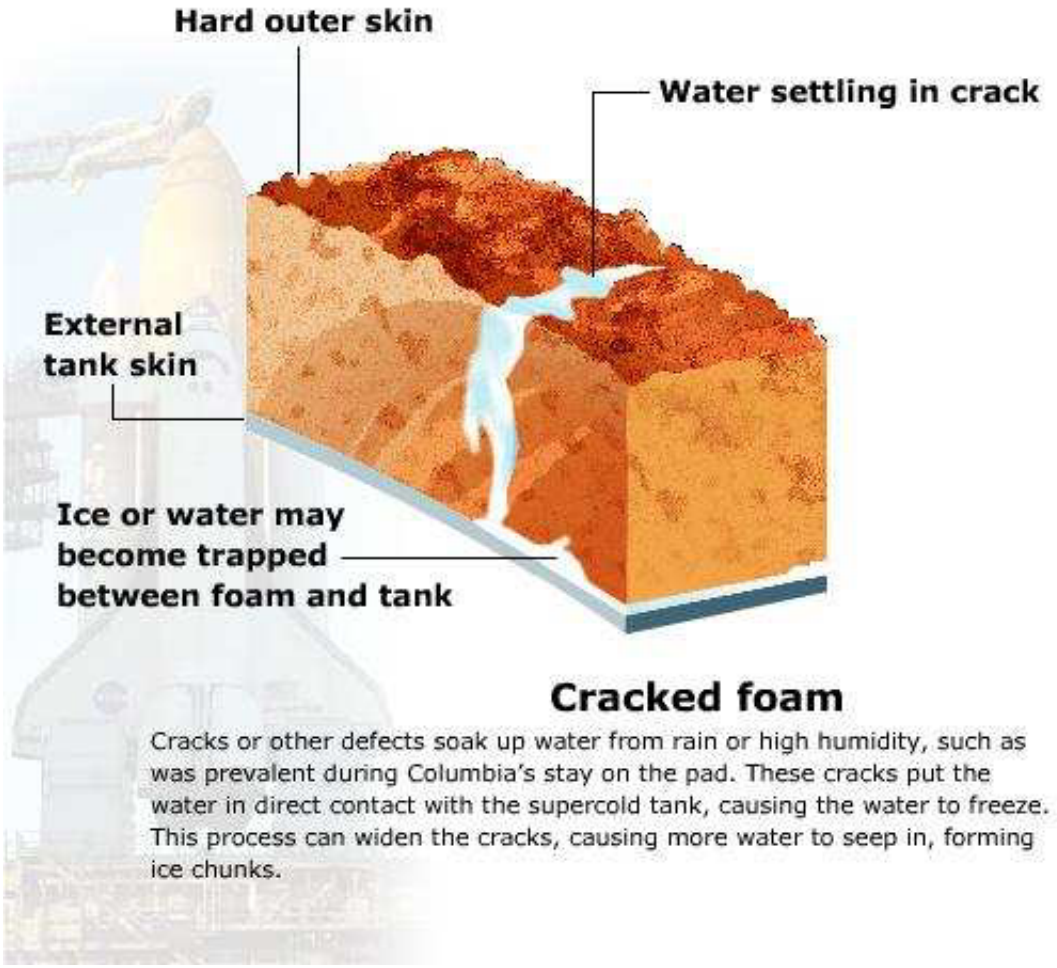

Figure 1.1: Graphic demonstrating delamination (separation) of foam from fuel tank due to water seepage (Copyright Florida Today, 2002).

Chapter 2

Gap Detection Problems

In this Section we apply an inverse problem formulation to determine the geometric characteristics of a defect (gap) inside of a dielectric material (see also [BGW03]). The gap causes a perturbation of the windowed electromagnetic interrogating signal due to reflections and refractions at the material interfaces. We model the electromagnetic waves inside the material with Maxwell's equations and use a Debye equation to model the polarization effects. Using simulations as forward solves, our Newton-based, iterative optimization scheme resolves the dimensions and location of the defect.

In Section 2.1 we define the equations that we have chosen in order to model the electromagnetic waves inside the material. We also distinguish between the two distinct problem types that we will address, namely the "void" problem (*Problem 1* and the "delamination" problem *Problem 2*). Section 2.2 contains the details of our numerical methods for the simulations. We introduce the inverse problem formulation for *Problem 1* in Section 2.3, and later improve upon it in Section 2.3.5. Numerical results of the inverse problem are displayed in Section 2.3.6.

In Section 2.4 we begin addressing *Problem 2*. Similarities and differences between the computational issues between the two problems are pointed out. A more sophisticated optimization method is described in Section 2.4.3 and associated numerical results are given in Section 2.4.5. Sections 2.4.6 and 2.4.7 explore the effects of adding random noise to the data, both relative and constant variance. In the latter, we compute standard error estimates.

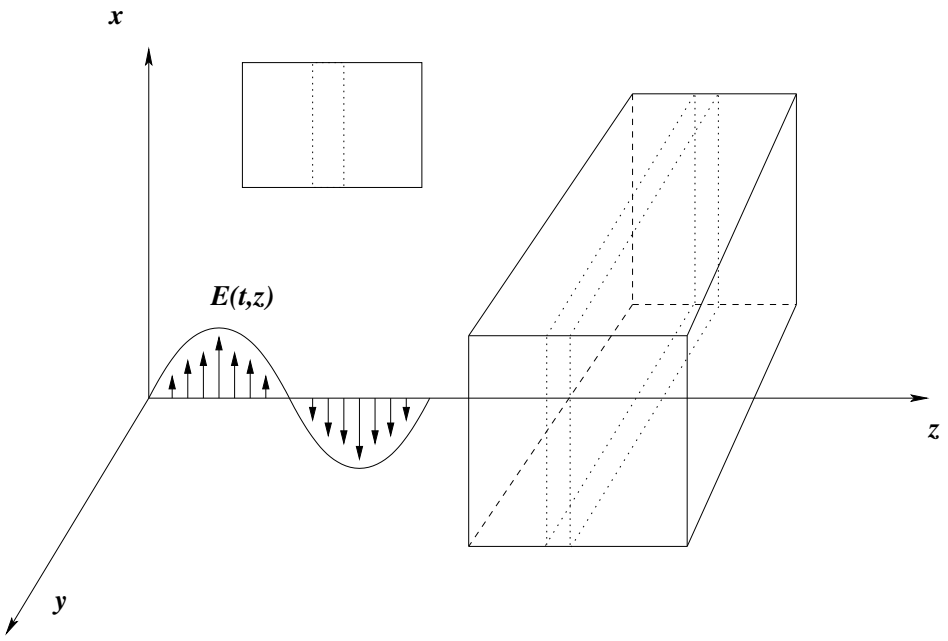

Figure 2.1: *Problem 1*: Dielectric slab with a material gap in the interior. Possible sensors in front and behind.

2.1 Problem Description

We interrogate an (infinitely long) slab of homogeneous nonmagnetic material by a polarized, windowed signal (see [BBL00] for details) in the THz frequency range (see Figure 2.1). We employ a wave normally incident on a slab which is located in $\Omega = [z_1, z_4]$, ($0 < z_1 < z_4 < 1$) with faces parallel to the x-y plane (see Figure 2.2). We denote the vacuum outside of the material to be Ω_0. The electric field is polarized to have oscillations in the x-z plane only. Restricting the problem to one dimension, we can write the electric and magnetic fields, $\vec{E}$ and $\vec{H}$ respectively, as follows

$$\vec{E}(t, \vec{x}) = \hat{i}E(t, z)$$
$$\vec{H}(t, \vec{x}) = \hat{j}H(t, z),$$

so that we are only concerned with the scalar values $E(t, z)$ and $H(t, z)$.

Maxwell's equations become:

$$\frac{\partial E}{\partial z} = -\mu_0 \frac{\partial H}{\partial t} \tag{2.1a}$$
$$-\frac{\partial H}{\partial z} = \frac{\partial D}{\partial t} + \sigma E + J_s, \tag{2.1b}$$

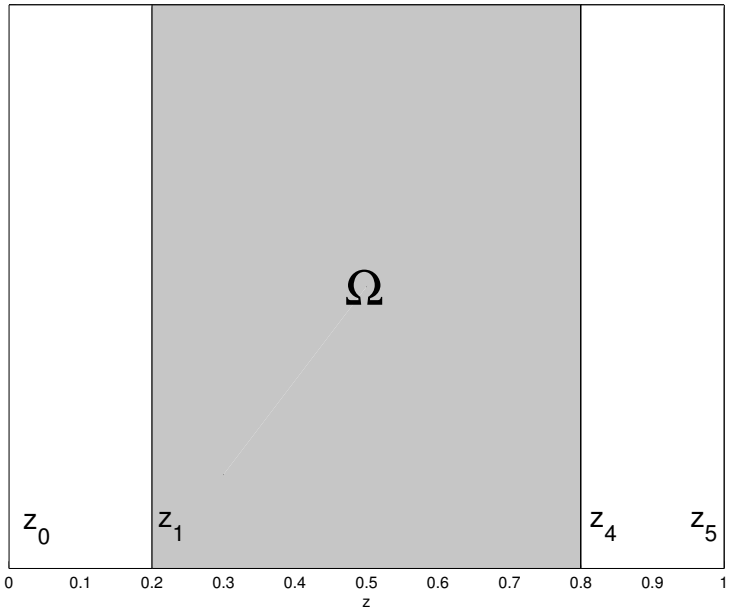

Figure 2.2: The domain of the material slab: $\Omega = [z_1, z_4]$.

where $D(t, z)$ is the electric flux density, μ_0 is the magnetic permeability of free space, σ is the conductivity, and J_s is a source current density (determined by our interrogating signal). We take the partial derivative of Equation (2.1a) with respect to z, and the partial of Equation (2.1b) with respect to t. Equating the $\frac{\partial^2 H}{\partial z \partial t}$ terms in each, and thus eliminating the magnetic field H, we have:

$$E'' = \mu_0 \left(\ddot{D} + \sigma \dot{E} + \dot{J}_s \right),$$

(where $'$ denotes z derivatives and $\dot{}$ denotes time derivatives).

Note that we have neglected magnetic effects and we have let the total current density be $J = J_c + J_s$, where $J_c = \sigma E$ is the conduction current density given by Ohm's law.

For our source current, J_s, we want to simulate a windowed pulse, i.e., a pulse that is allowed to oscillate for one full period and then is truncated. Further, we want the pulse to originate only at $z = 0$, simulating an infinite antenna at this location. Thus we define

$$J_s(t, z) = \delta(z) sin(\omega t) I_{[0, t_f]}(t)$$

where ω is the frequency of the pulse, $t_f = 2\pi/\omega$ is fixed, $I_{[0,t_f]}(t)$ represents an indicator function which is 1 when $0 \leq t \leq t_f$ and zero otherwise, and $\delta(z)$ is the Dirac delta distribution.

Remark 1 *Computationally, having a truncated signal introduces discontinuities in the first derivatives which are not only problematic in the numerical simulations (producing spurious oscillations), but are also essentially non-physical. Therefore in our implementation we actually multiply the sine function by an exponential function (see Figure 2.3) rather than the traditional indicator function. The exponential is of the form*

$$exp\left(-\left(\frac{t-\theta\frac{t_f}{2}}{\alpha}\right)^{\beta}\right),$$

where θ controls the horizontal shift, α determines the width and β determines the steepness of the sides. A value of $\theta = 2$ provides a sufficient buffer before the signal to avoid leading oscillations due to the initial discontinuity. For notational consistency we will continue to denote this function as $I_{[0,t_f]}(t)$.

The electric flux density inside the material, given by $D = \epsilon_0\epsilon_\infty E + P$, is dependent on the polarization, P. Note that ϵ_0 is the permittivity of free space and ϵ_∞ is the relative permittivity in the limit of high frequencies (thus the notation of ∞). For computational testing we assume for this presentation that the media is Debye and thus we use the following polarization model inside Ω:

$$\tau\dot{P} + P = \epsilon_0(\epsilon_s - \epsilon_\infty)E$$

where ϵ_s is the static relative permittivity and τ is the relaxation time. We also assume $P(0, z) = 0$. Note that in the vacuum outside of Ω, $P = 0$.

In order to represent D in the entire domain, we use the indicator function I_Ω which is 1 inside Ω and zero otherwise. Thus

$$D = \epsilon_0 E + \epsilon_0(\epsilon_\infty - 1)I_\Omega E + I_\Omega P.$$

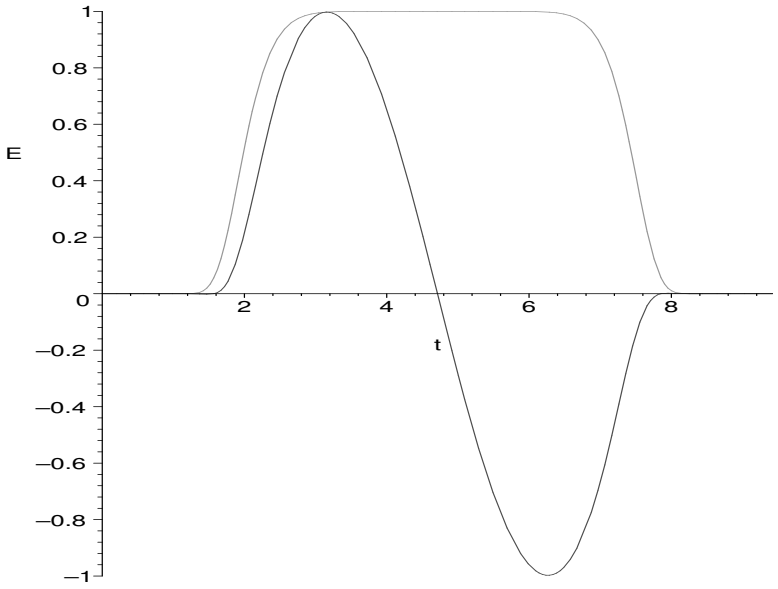

Figure 2.3: Our choice of a smooth indicator function and the resulting (smoothly truncated) interrogating signal. In this example $\theta = 2$, $\alpha = .9$, and $\beta = 10$.

In order to have a finite computational domain, we impose absorbing boundary conditions at $z = 0$ and $z = 1$, which are modeled as

$$\left[\dot{E} - cE'\right]_{z=0} = 0$$
$$\left[\dot{E} + cE'\right]_{z=1} = 0.$$

With these boundary conditions, any incident signal passes out of the computational domain, and does not return, i.e., we force it to be absorbed by the boundary. Also we assume zero initial conditions:

$$E(0, z) = 0$$
$$\dot{E}(0, z) = 0.$$

Thus our entire system can be written

$$\begin{aligned}
\mu_0\epsilon_0(1+(\epsilon_\infty-1)I_\Omega)\ddot{E}+\mu_0 I_\Omega\ddot{P}+\mu_0\sigma\dot{E}-E'' &= -\mu_0\dot{J}_s && \text{in } \Omega\cup\Omega_0\\
\tau\dot{P}+P &= \epsilon_0(\epsilon_s-\epsilon_\infty)E && \text{in } \Omega\\
[\dot{E}-cE']_{z=0} &= 0\\
[\dot{E}+cE']_{z=1} &= 0\\
E(0,z) &= 0\\
\dot{E}(0,z) &= 0
\end{aligned}$$

with

$$J_s(t,z)=\delta(z)sin(\omega t)I_{[0,t_f]}(t).$$

In this formulation we have initially assumed a single slab of a dielectric contained in $\Omega=[z_1,z_4]$. Thus $I_\Omega=1$ if $z_1<z<z_4$, and zero otherwise. We now introduce a gap (crack) consisting of a vacuum in the interior of the material as depicted in Figure 2.4. If the gap is (z_2,z_3) then we redefine $\Omega=\{z|z_1\le z\le z_2 \text{ or } z_3\le z\le z_4\}$. We will refer to this formulation as *Problem 1* (recall Figure 2.1). Later we will discuss a second formulation, *Problem 2*, where the gap is between the dielectric slab and a metallic (supra-conducting) backing, as shown in Figure 2.5. This will require slightly different boundary conditions (reflecting instead of absorbing at $z=1$, where the metal backing begins), but otherwise the numerical solution methods and analysis are the same.

2.2 Numerical Solution

2.2.1 Finite Elements

We apply a Finite Element method using standard linear one dimensional basis elements [J95] to discretize the model in space. Let N be the number of intervals in the discretization of z, and $h=1/N$, then the Finite Element discretization has an order of accuracy of $O(h^2)$. For implementation we scale time by $\tilde{t}=ct$ and the polarization by $\tilde{P}=P/\epsilon_0$ for convenience. The resulting system of ordinary differential equations after the

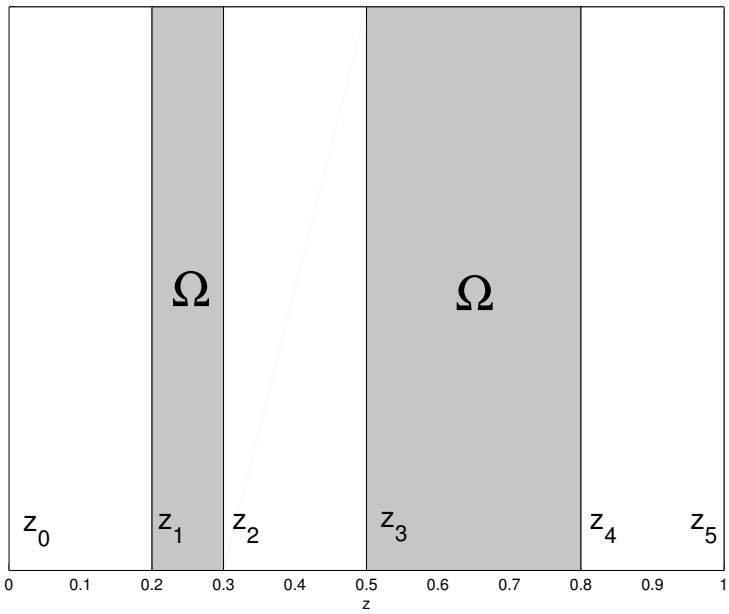

Figure 2.4: The domain of the material slab with an interior gap between z_2 and z_3: $\Omega = \{z | z_1 \leq z \leq z_2 \text{ or } z_3 \leq z \leq z_4\}$.

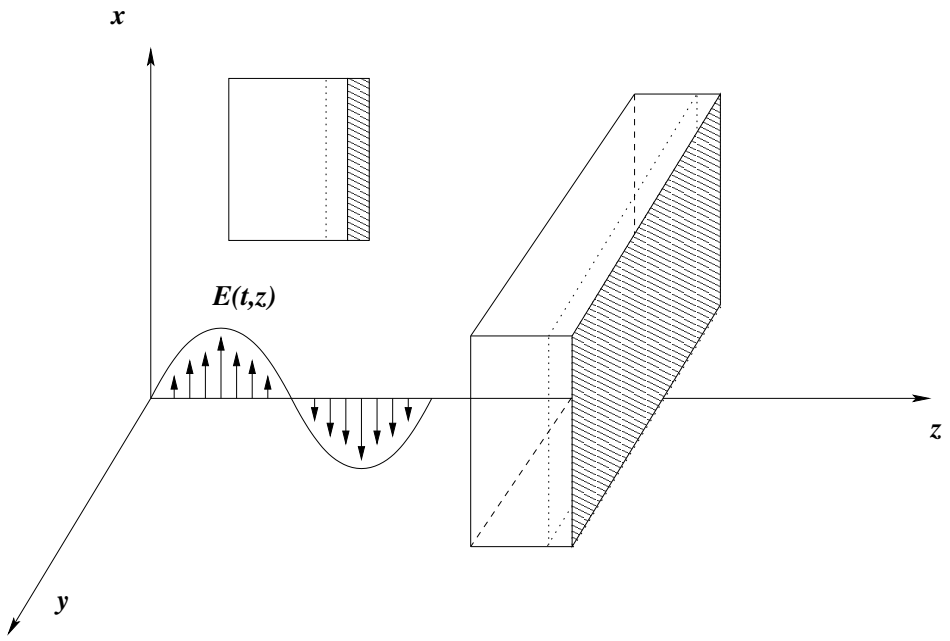

Figure 2.5: *Problem 2*: Dielectric slab and metallic backing with a gap in between. Possible sensors only in front.

spatial discretization is the semi-discrete form

$$\epsilon_r M\ddot{e} + M^{\Omega}\ddot{p} + (\eta_0\sigma M + D + B)\dot{e} + Ke = \eta_0 J \tag{2.2a}$$

$$M^{\Omega}\dot{p} + \lambda M^{\Omega} p = \epsilon_d \lambda M^{\Omega} e, \tag{2.2b}$$

where $\epsilon_r = (1 + (\epsilon_\infty - 1)I_\Omega)$, $\epsilon_d = \epsilon_s - \epsilon_\infty$, $\lambda = \frac{1}{c\tau}$, and $\eta_0 = \sqrt{\mu_0/\epsilon_0}$. Also e and p are vectors representing the values of E and P, respectively, at the nodes $\tilde{z}_i = ih$. The mass matrix M has entries

$$M_{ij} = \langle \phi_i, \phi_j \rangle \ := \int_0^1 \phi_i \phi_j dz$$

where $\{\phi_i\}_{i=1}^N$ are the basis functions (M^Ω is the mass matrix integrated only over Ω), while the stability matrix K has entries

$$K_{ij} = \langle \phi_i', \phi_j' \rangle \ := \int_0^1 \phi_i' \phi_j' dz.$$

The matrices D and B result from the boundary conditions where

$$D_{1,1} = 1$$

$$B_{N+1,N+1} = 1$$

and all other entries are zero. Finally, J is defined as

$$J_i = -\langle \phi_i, \dot{J}_s \rangle \ := -\int_0^1 \dot{J}_s \phi_i dz.$$

Note that by differentiating (2.2b) we can substitute into (2.2a) and obtain an equation only dependent explicitly on P (two substitutions are required to eliminate $\ddot{P}$ and $\dot{P}$):

$$\epsilon_r M\ddot{e} + (\eta_0\sigma M + D + B + \epsilon_d\lambda M)\dot{e} + (K - \epsilon_d\lambda^2 M)e + \lambda^2 M^{\Omega} p = \eta_0 J.$$

Using shorthand we can write our entire coupled system as

$$M_1\ddot{e} + M_2\dot{e} + M_3 e + \lambda^2 \bar{p} = \eta_0 J \tag{2.3a}$$

$$\dot{\bar{p}} + \lambda\bar{p} = \epsilon_d \lambda M^{\Omega} e \tag{2.3b}$$

where $\bar{p} = M^{\Omega} p$. It is important to mention that each matrix is tridiagonal due to the choice of the linear finite elements.

2.2.2 Finite Differences

In order to solve the semi-discrete form of our equations we consider two distinct finite difference methods for comparison. In the first method we convert the coupled second order system of equations into one larger first order system and simply apply a theta method (unless otherwise stated, we use $\theta = \frac{1}{2}$). In the second method we solve first for the polarization with a forward differencing scheme using the initial conditions and then use that to update a second order central difference scheme for the magnitude of the electric field. We then continue this process iteratively, alternating between solving for P and for E.

Both methods are second order in time and space for appropriately smooth data (and with $\Delta t = O(h)$). We compare the errors (when available) and the runtimes of the two methods and make observations on other characteristics that may be of practical concern.

2.2.3 Method 1

First we convert (2.3a) and (2.3b) into one large system of first order equations by introducing $\dot{e}$ as a variable and creating the large vector $x = [e; p; \dot{e}]$. Thus we write our large system as

$$A\dot{x} + Bx = C.$$

We apply a θ-method to obtain

$$Ax_{n+1} = Ax_n + \Delta t(-Bx_{n+\theta} + C_{n+\theta}),$$

where, for example, $C_{n+\theta} = (1-\theta)C_n + \theta C_{n+1}$ and $[x_n]_j \approx E(t_n, \tilde{z}_j)$ with $\tilde{z}_j = jh$. Solving for the x_{n+1} term yields

$$\bar{M}x_{n+1} = \bar{M}x_n + \Delta t(C_{n+\theta} - Bx_n)$$

where $\bar{M} = A + \Delta t\theta B$. Thus if

$$x_{n+1} = x_n + \Delta t y_n$$

then

$$\bar{M}y_n = C_{n+\theta} - Bx_n.$$

We solve for the LU factorization [BF93] of $\bar{M}$ at the beginning and use back substitution at each time step to solve for y_n.

For $\theta = \frac{1}{2}$ this method will be second order in time if the corresponding solution is C^3 in time. We inherit $O(h^2)$ from the FEM formulation, thus overall this approximation method is $O(h^2)$ when $\Delta t = O(h)$. Further, since Crank-Nicolson is unconditionally stable [QSS00], this choice of time step is allowable.

2.2.4 Method 2

In our second method we use a second order central difference scheme to solve (2.3a). Thus we must first find an approximation to e_2. Note that approximating E with its Taylor expansion around $t_1 = 0$ and applying the initial conditions and ODE we obtain

$$E(t_2, z) \approx -\frac{\Delta t^2}{2}\mu_0 \dot{J}_s(0, z).$$

Our approach is to first solve for p using a θ-method, and then use that approximation to solve for e at the next time step. Thus, our finite difference approximation for (2.3b) is

$$\begin{aligned} Mp_{n+1} &= Mp_n - \Delta t\lambda M p_{n+\theta} + \Delta t\lambda\epsilon_d M e_{n+\theta} \\ Mp_{n+1} &= Mp_n + \frac{\lambda\Delta t}{1+\lambda\Delta t\theta} M(\epsilon_d e_{n+\theta} - p_n), \end{aligned}$$

and using $[\bar{p}_n]_j \approx M^\Omega P(t_n, \tilde{z}_j)$:

$$\bar{p}_{n+1} = \bar{p}_n + \frac{\lambda\Delta t}{1+\lambda\Delta t\theta}(\epsilon_d M^\Omega e_{n+\theta} - \bar{p}_n). \tag{2.4}$$

where $e_{n+\theta} = \theta e_n + (1-\theta)e_{n+1}$ is a weighted average of e_n and e_{n+1} added for relaxation to improve the stability of the method. Once we have $\bar{p}_{n+1}$ we can solve for e_{n+2}. Applying second order central difference with averaging to (2.3a) gives

$$\frac{1}{\Delta t^2}M_1(e_n - 2e_{n+1} + e_{n+2}) + \frac{1}{2\Delta t}M_2(e_{n+2} - e_n) + \frac{1}{4}M_3(e_n + 2e_{n+1} + e_{n+2}) = \eta_0 J_{n+1} - \lambda^2 \bar{p}_{n+1}.$$

Solving for the e_{n+2} term we have

$$\left[M_1 + \frac{\Delta t}{2}M_2 + \frac{\Delta t^2}{4}M_3\right] e_{n+2} = \left[2M_1 - \frac{\Delta t^2}{2}M_3\right] e_{n+1} + \left[-M_1 + \frac{\Delta t}{2}M_2 - \frac{\Delta t^2}{4}M_3\right] e_n + \Delta t^2\eta_0 J_{n+1} - \lambda^2\Delta t^2 \bar{p}_{n+1}$$

or equivalently,

$$A_1 e_{n+2} = A_2 e_{n+1} + A_3 e_n + \Delta t^2\eta_0 J_{n+1} - \lambda^2\Delta t^2 \bar{p}_{n+1}. \tag{2.5}$$

Note that in this case A_1 is tridiagonal and the matrix is the same for each time step, so we may store the Crout LU factorization and use back substitution to solve the system at each time step. For tridiagonal matrices the factorization and the back substitution are both order $O(N)$ [BF93].

Again, for $\theta = \frac{1}{2}$, (2.4) will be second order in time if the corresponding solution is C^3 in time. Equation (2.5) is also second order in time assuming an exact solution for P, and that E has four continuous time derivatives (for the second order difference approximation). The truncation error for this approximation is

$$T(t_n) = \Delta t^2 \left(\frac{1}{12} e^{(4)} + \frac{1}{6} e^{(3)} + \frac{1}{4} e^{(2)} \right).$$

Therefore, since the semi-discrete form is $O(h^2)$, this approximation method overall is $O(h^2)$ when $\Delta t = O(h)$.

To consider stability we apply von-Neumann stability analysis [MM94]. Equation (2.5), with zero forcing, becomes

$$\bar{M}_2 g(\xi)^2 = \bar{M} + \bar{M}_1 g(\xi).$$

Solving for the magnitude of $g(\xi)$ yields

$$|g(\xi)| = \left| \frac{1}{2} \bar{M}_2^{-1} \left(\bar{M}_1 \pm \sqrt{(} \bar{M}_1^2 + 4 \bar{M} \bar{M}_2 \right) \right|.$$

With the sample parameters that we use in our simulations, the determinants are: $0.038 - 0.004i$ and $0.038 + 0.004i$ for the plus and minus cases respectively, thus the method is unconditionally stable. Since Crank-Nicolson is also unconditionally stable, our choice of time step should be reasonable. We note that the stability of each of (2.4) and (2.5) does not imply stability of the coupled method. This is a more difficult matter to analyze.

2.2.5 Simple Example (Vacuum)

In order to have a problem that we can test the error we want to be able to find an analytical solution. The most simple case, still incorporating the windowed pulse, is the solution in a vacuum. Note that this implies $\sigma = 0$ thus $P = 0$ everywhere.

Maxwell's equations in a vacuum reduce to

$$E'' = \mu_0 \epsilon_0 \ddot{E} + \mu_0 \dot{J}_s.$$

From PDE's we know that with homogeneous initial conditions that the exact solution, using J_s as defined in (2.1), is [S92]:

$$E(t,z) = \frac{1}{2c}\int\int -\mu_0 c^2 \dot{J}_s$$

which can be shown to be

$$E(t,z) = \frac{\mu_0 c}{2}(H(z-t+t_f) - H(z-t))\sin\left(\frac{2\pi t}{t_f}\right),$$

where H denotes the Heaviside function. This is simply a propagating truncated wave with amplitude $\frac{\mu_0 c}{2}$. Thus, if $t - t_f < z < t$ then the solution is

$$E(t,z) = \frac{\mu_0 c}{2} sin(\omega(z-t+t_f)), \tag{2.6}$$

and it is zero otherwise. Note, since the wave travels at velocity c, to go from $z = 0$ to $z = 1$ meters will take $t = 1/c = 3.3356$ nanoseconds. Thus, this (plus t_f) will be our concluding time for our simulations.

The values of our physical parameters for this simple example (for reference) are:

$$\epsilon_0 = 8.854 \times 10^{-12}$$
$$\mu_0 = 1.2566 \times 10^{-6}$$
$$\epsilon_s = 1$$
$$\epsilon_\infty = 1$$
$$\sigma = 0.$$

Also, we considered a pulse with frequency of 2 GHz, i.e., $\omega = 4\pi \times 10^9$.

2.2.6 Analysis of Results

We simulated the above example using $N = 400$ and $\Delta t = h/10$. Figure 2.6 depicts the computed solution, the exact solution, and the error, respectively (using Method 2). There is a noticeable oscillation at the front of the wave most likely due to the discontinuity in the initial conditions. Figure 2.7 depicts the same plots only at a later time. We see that the global error is increasing with time. Also the absorbing boundary condition is evident.

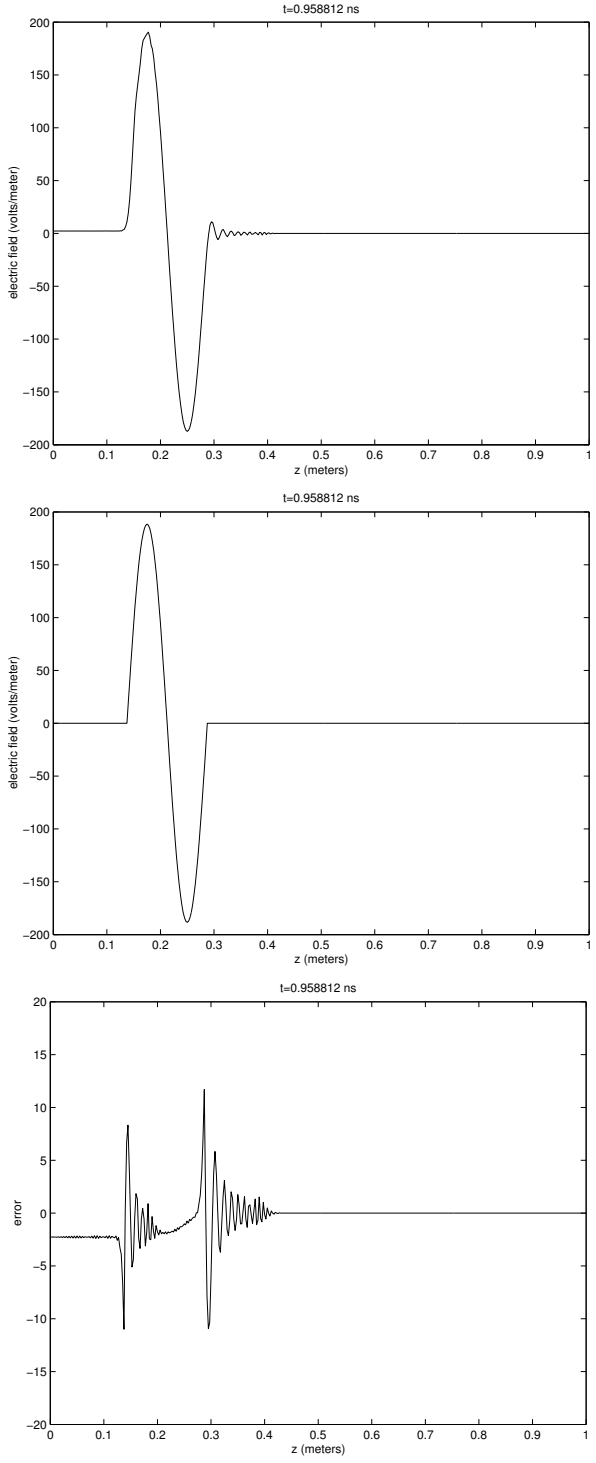

Figure 2.6: The computed solution in a vacuum (above), the exact solution (middle) and the difference between the two (below), using $N = 400$ and $\Delta t = h/10$.

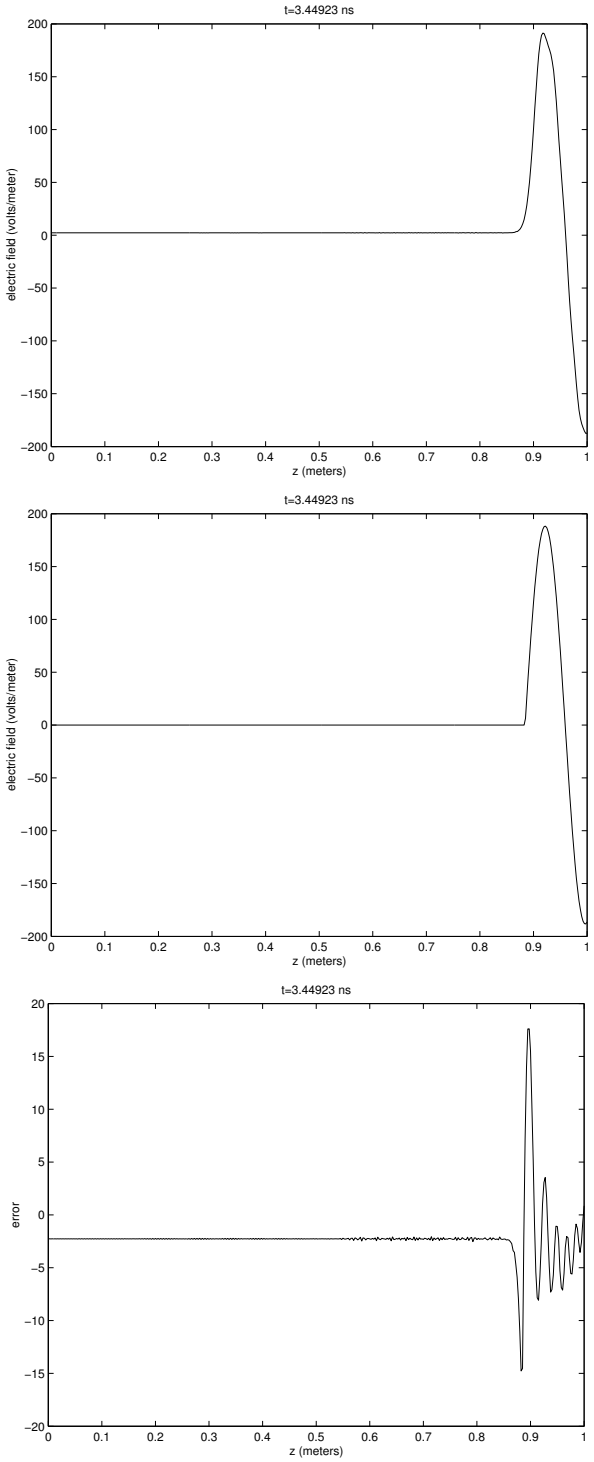

Figure 2.7: The computed solution in a vacuum at a later time (above), the exact solution (middle) and the difference between the two (below), using $N = 400$ and $\Delta t = h/10$. The absorbing boundary condition at $z = 1$ is apparent.

Both methods performed well, yielding similar errors. Figure 2.8 depicts the error using Method 1 and Method 2 for comparison. Although both methods were stable for most values of the parameters, since our exact solution is not smooth enough, we do not expect to obtain the second order accuracy our theory predicts. In fact, both methods converge with less than first order accuracy according to grid refinement analysis ($O(h^{\cdot 7})$). The errors and runtimes are given in Table 2.1.

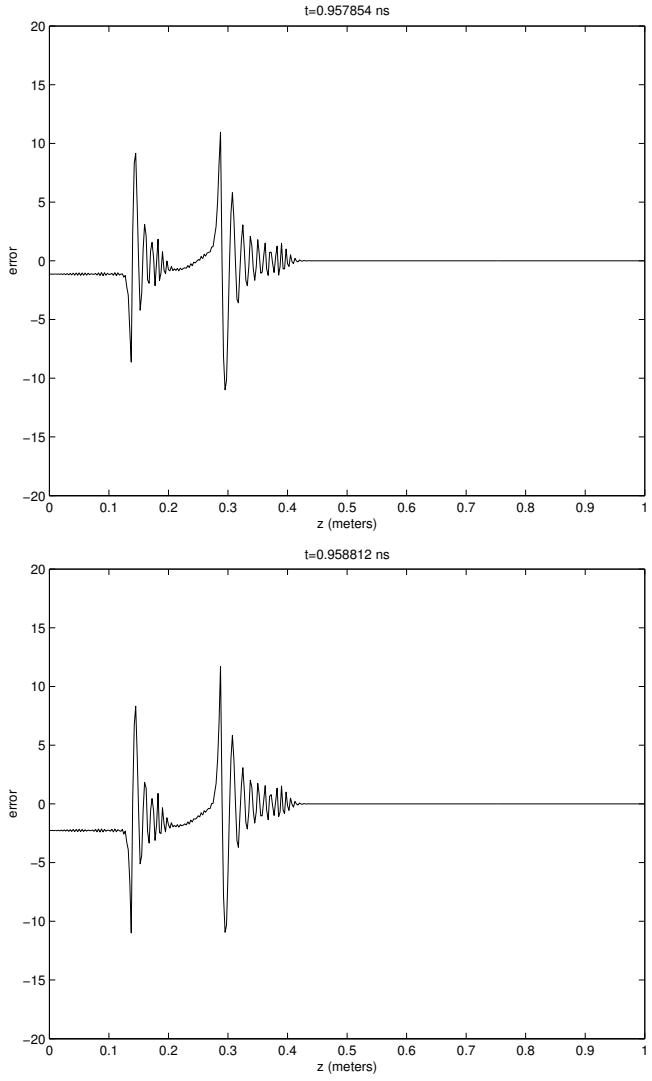

Figure 2.8: The error from Method 1 and Method 2 for comparison. Again, using $N = 400$ and $\Delta t = h/10$.

Table 2.1: The maximum error (over time) and the total execution time for simulations using Method 1 and Method 2 with various mesh sizes.

Method	Max error	Execution time (seconds)
$(N = 200)$		
Method 1	36.6530	3.7008
Method 2	38.1030	2.2227
$(N = 400)$		
Method 1	19.4206	14.3258
Method 2	18.4472	7.7873
$(N = 800)$		
Method 1	11.3081	60.4923
Method 2	10.8401	30.6036
$(N = 1600)$		
Method 1	7.4817	243.1902
Method 2	7.3027	121.1999

The most notable difference in the two methods was that not only did the second method perform slightly better with regards to error, but it was twice as fast in all cases. For example, for $N = 400$ Method 1 took 14.3258 seconds, while Method 2 took 7.7873 seconds (the errors, after 4 ns, were 9.7% and 9.2% respectively).

After the accuracy of the methods was established, we attempted to solve a more realistic problem. This time we took the medium to be a non-vacuous Debye medium with the following parameters:

$$\epsilon_s = 80.1$$
$$\epsilon_r = 5.5$$
$$\sigma = 1 \times 10^{-5}$$
$$\tau = 3.16 \times 10^{-8}.$$

Figure 2.9 depicts the computed solutions at two different times. As both methods produced similar results, we only show one set of simulations. We notice that the amplitude decreases significantly as it propagates. Also, the speed of propagation in the medium is about half that of the speed of the wave in a vacuum. All of these observations are in accord with observed experimental results, thus adding validity to the model and the computational methods.

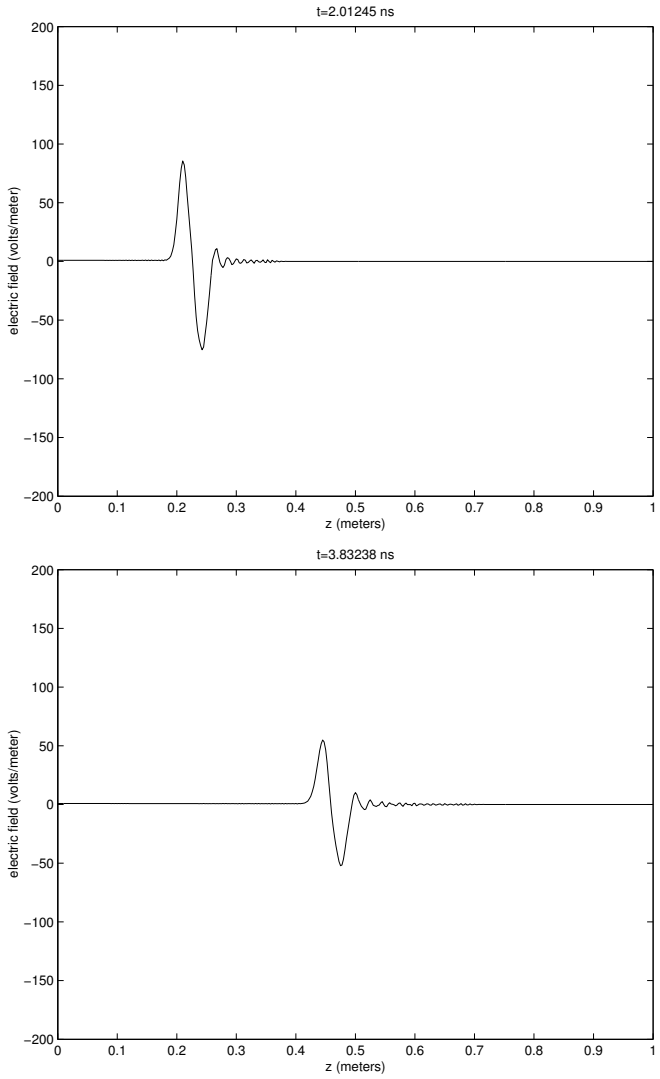

Figure 2.9: Computed solutions of an windowed electromagnetic pulse propagating through a Debye medium at two different times. The decreasing amplitude and slower speed are both apparent.

However, it should be noted that for the non-vacuous problem the second method did exhibit instability for τ values of less than 10^{-12}, but it is most likely due to roundoff or overflow and can probably be fixed with an appropriate scaling. Method 1 was stable for all attempted values of τ.

2.2.7 Choice of Method

We solved the semi-discrete form of Maxwell's Equations in $1D$ by using two numerical methods for comparison. In the first method we converted the coupled second order system of equations into one larger first order and simply applied a theta method. We theoretically determined the method to be of $O(h^2)$ accuracy with $\Delta t = O(h)$ as well as to be unconditionally stable. The simulations demonstrated good stability and reasonable accuracy considering the lack of smoothness of the exact solution.

In the second method we solved first for the polarization using Crank-Nicolson and used it to update a second order central difference scheme for the magnitude of the electromagnetic field. Each scheme was shown to be second order in time and space for appropriately smooth data, and both were shown to be independently unconditionally stable.

We compared the errors and the runtimes of the two methods and determined that for practical use the increased speed obtained by using Method 2 is substantial. Thus the approach we choose, namely Method 2, is to first solve for $\bar{p}$ using a θ-method, and then use that approximation to solve for e at the next time step. The only concern is the loss of stability for very large values of the parameters (roundoff), and possibly for very small time steps. From our simulations we found that if Δt is too large, or even too small, the method exhibits some instability which can result in noisy oscillations before, or after, the actual signal. In our testing we have determined that there is an optimal range of values for Δt given a fixed h.

Remark 2 *An inverse problem formulation requires that the sample time of the given data (which is* $st := 1/sr$*, where* sr *is the sample rate with units of number of observations per second) be larger than the time step of the simulations. Since we have an optimal range of values for our time step, occasionally our preferred time step will be larger than the sample time of the given data. Rather than significantly modifying our time step, we discard the extra data points, effectively multiplying the sample rate by an integer multiple. (We refer to this new sample rate as the effective sample rate* sr_e *which will be used to determine the observations on the simulations in the inverse problem.) Note that since*

$dt = O(h) = O(1/N)$, a larger N may result in more data points being retained, and thus provides an additional advantage in finding an optimal solution over the usual increased accuracy in the discretization schemes.

2.2.8 Method of Mappings

We want the spatial discretization of the domain to incorporate the interfaces between the material and the vacuum so that physical characteristics are not split across more than one finite element. However, we do not want to limit ourselves to simulating gap widths that are in effect multiples of a fixed h. Decreasing h to compensate would increase computational time unnecessarily. Instead we employ the "method of mappings". In essence we map our computational domain to a reference domain with a predetermined discretization, using a linear transformation. In this way we can ensure that all of our boundaries are mapped to node locations. Also, regardless of how small the crack may be, we are guaranteed a fixed number of elements to accurately resolve the behavior of the electric field in that region. Each interval $[\tilde{z}_i, \tilde{z}_{i+1}]$ is mapped to a predeterminined interval $[\hat{z}_i, \hat{z}_{i+1}]$ by

$$\hat{z} = \hat{z}_{i+1}\left(\frac{\tilde{z} - \tilde{z}_i}{\tilde{z}_{i+1} - \tilde{z}_i}\right) + \hat{z}_i\left(\frac{\tilde{z} - \tilde{z}_{i+1}}{\tilde{z}_i - \tilde{z}_{i+1}}\right).$$

In effect we are using a variable mesh size, thus we must take care to check that in mapping our domain we do not "stretch" or "shrink" any interval too much because our error is based on the mesh size in the original domain. Although our reference domain may be equally spaced with small subintervals, in general our effective mesh sizes can be quite large. Therefore, we monitor the magnitude of the scaling factors and rediscretize our reference domain if any mesh size is too large. The method of mappings also allows us to easily normalize our domain length, which justifies our theoretical development of the problem in the domain $z \in [0, 1]$.

The method of maps also alters our inner products used in the weak formulation of the problem. We subsequently use a weighted inner product defined as follows:

$$\langle \phi, \psi \rangle = \int_{z_0}^{z_5} \phi(z)\psi(z)dz = \int_0^1 \phi(f^{-1}(\hat{z}))\psi(f^{-1}(\hat{z}))\frac{d\hat{z}}{(f^{-1})'(\hat{z})}$$

where $f(z) = \hat{z}$ is the piece-wise linear transformation on $[z_0, z_5]$.

2.2.9 Numerical Simulations

The following figures depict the numerical solution of the amplitude of the electric field at various times (Figures 2.10 and 2.11), as well as the signal recorded at receivers located at $z = 0$ (Figure 2.12) and $z = 1$ (Figure 2.13). We considered a Debye medium with the following parameters:

$$\begin{aligned} \epsilon_s &= 78.2, \\ \epsilon_\infty &= 5.5, \\ \sigma &= 1 \times 10^{-5}, \\ \tau &= 3.16 \times 10^{-8}, \\ f &= 2GHz, \end{aligned}$$

and a material gap located at $[z_3, z_4] = [.6, .61]$.

We have used 2 GHz simply so that our computational domain of $z \in [0, 1]$ would not have to be scaled for this demonstration. Also, in practice, one would not compute a domain so much larger than the material, just as in an experiment the sensors should be as close to the material as possible to reduce noise. We did so here merely so that the full wavelength of the signal would be visible. Finally, we have carried the time length well past the first reflections, again just for demonstration purposes. We chose to plot Figures 2.12 and 2.13 with the time unit scaled seconds (ss) which is just seconds multiplied by the speed of light in a vacuum, $ss = c \cdot s$. This, along with the placement of the material $.5m$ from the sensor, validates the timing of the first reflection (see Figure 2.12) in that it has traveled $1m$ in c seconds.

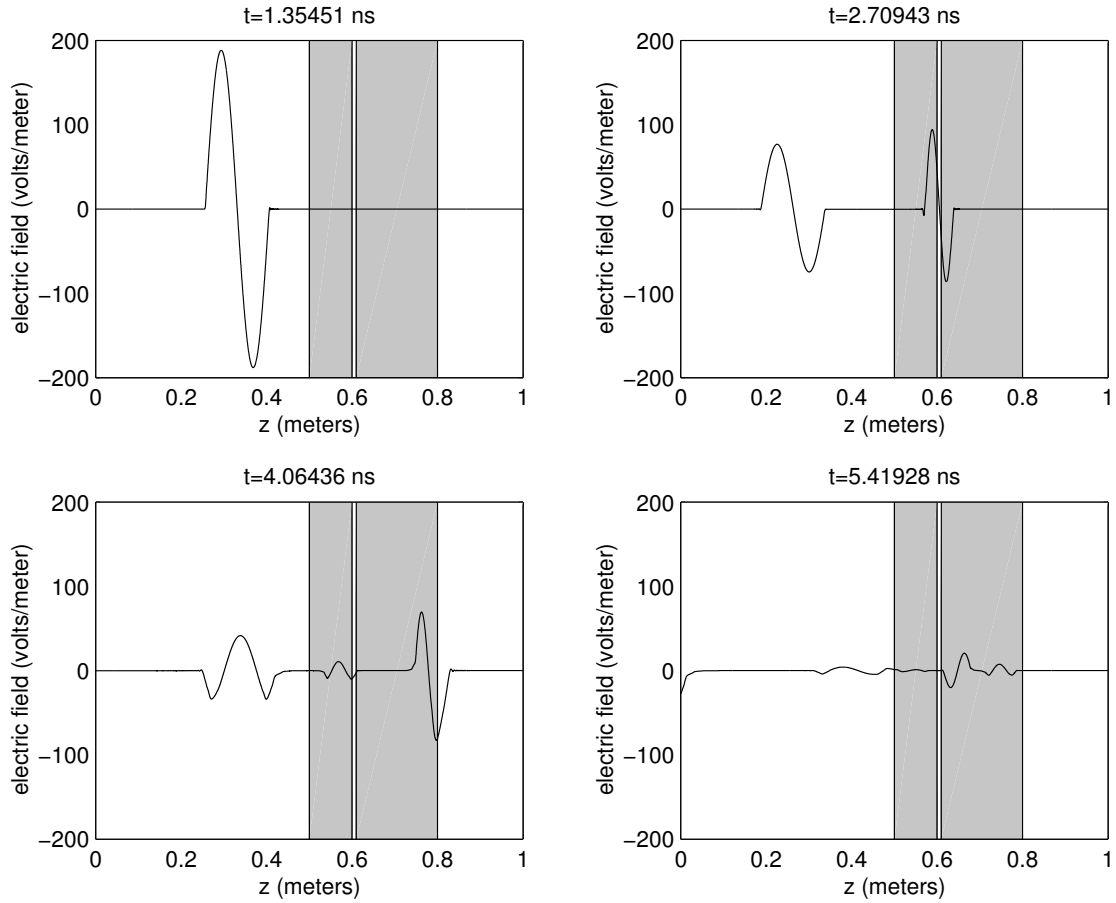

Figure 2.10: Computed solutions at different times of a windowed electromagnetic pulse incident on a Debye medium with a crack.

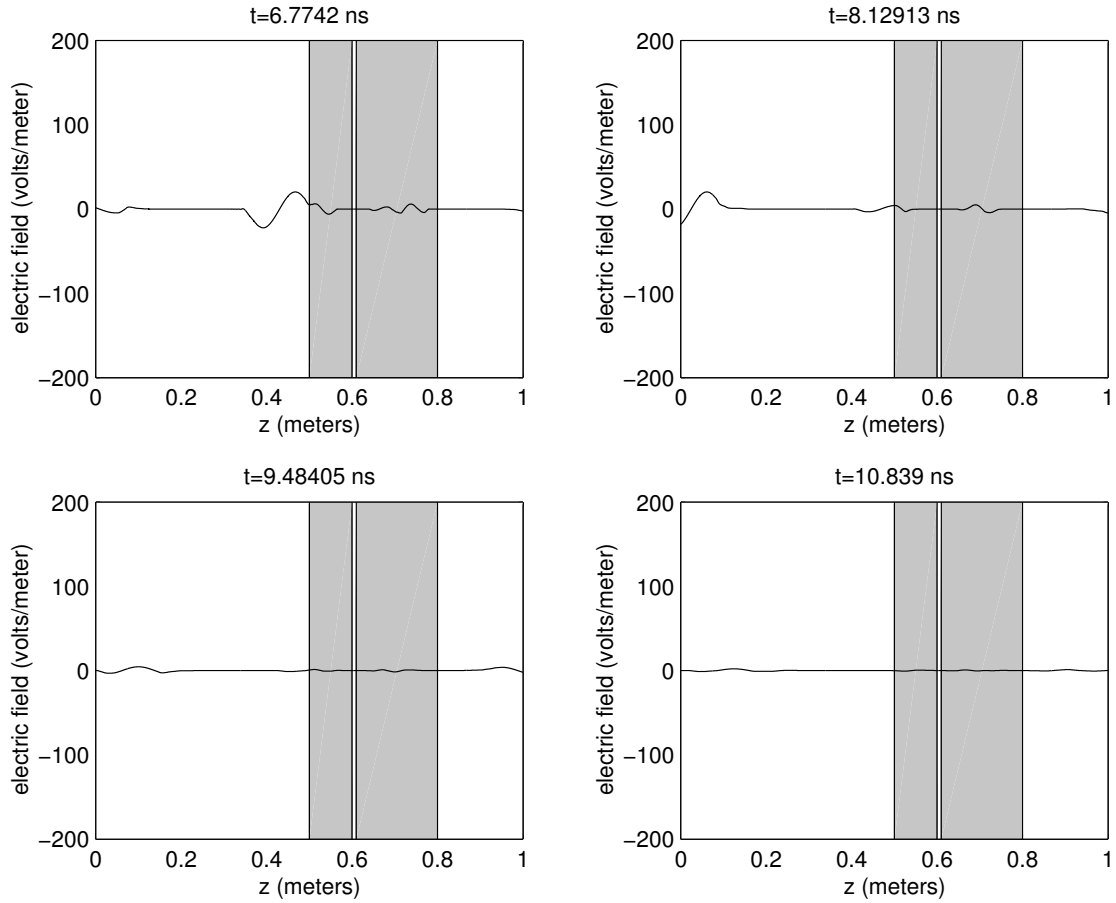

Figure 2.11: (Con't) Computed solutions at different times of a windowed electromagnetic pulse incident on a Debye medium with a crack.

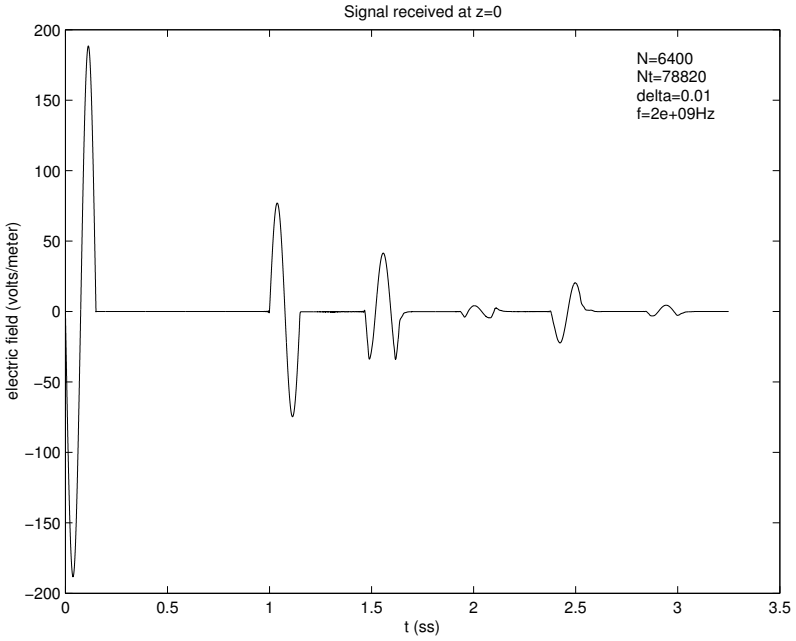

Figure 2.12: Signal received at $z = 0$, plotted versus seconds scaled by c.

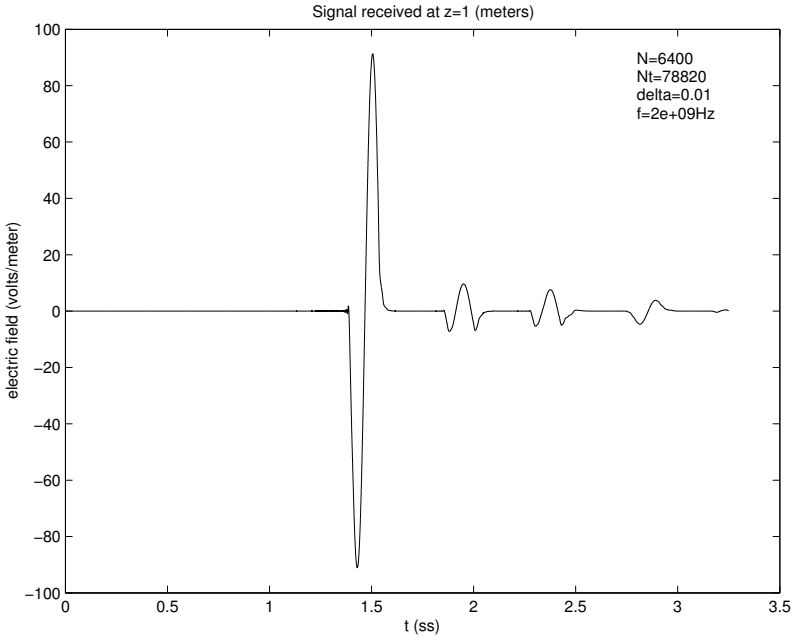

Figure 2.13: Signal received at $z = 1$, plotted versus seconds scaled by c.

2.3 Problem 1

We now apply an optimization routine to the least squares error between a simulated signal and the given data to try to determine the crack characteristics. In particular we will be trying to find the depth, $d := z_2 - z_1$, and the width, $\delta := z_3 - z_2$, which will produce a simulated signal most closely similar (in the least squares sense) to the data.

2.3.1 Inverse Problem

All of the following are solved with respect to a reference problem ($R1$) with these parameter values (see also Figure 2.4):

$z_0 = 0, z_1 = .2, z_2 = .3, z_3 = .5, z_4 = .8, z_5 = 1.0$

$f = 4$ GHz, t_f is one period

$\tau = 8.1 \times 10^{-12}, \sigma = 1 \times 10^{-5}, \epsilon_s = 80.1, \epsilon_\infty = 5.5$ in the material

$N = 1024, N_t = 12926$

The sample rate for the data is one sample per $.05ns$

With this choice of parameters, the forward solve solution at $z = 0$ clearly shows distinct reflections from the z_1, z_2, and z_3. This clear distinction will aid in our approximating the initial guesses, thus making this a relatively easy sample problem.

2.3.2 Initial Guesses

Assuming the physical parameters are given (either known or from a previous estimation), we want to determine the depth of any crack (d), and the width of that crack (δ), using reflection and/or transmission signals. First we will attempt to obtain very close approximations to d and δ using information about the travel times of the data signal, then we will use these values as initial guesses in the optimization routine.

We now describe how to identify the return time of each reflection, which in turn is used to estimate each z_i value, and therefore d and δ. We need to be able to identify the point in time when a reflection begins, i.e., the root immediately in front of a peak (or trough) in the signal. (Note that certain reflections are oriented peak first, while others are oriented trough first.) Three methods of doing this are as follows:

i. $tr_1(i) = \min t$ such that $|\dot{E}(t)| > C_1$ and $t > C_2$, where C_1 is chosen to avoid noise being confused with reflections, and C_2 is large enough that the previous reflection has passed.

ii. $tr_2(i) = \max t$ such that $|E(t)| < C_1$ and $t < C_2$, where C_1 is chosen to avoid noise being confused with reflections, and C_2 is small enough that the peak (or trough) has not yet passed.

iii. $tr_3(i) = \max t_j$ such that $\hat{E}(t_j)\hat{E}(t_{j+1}) < 0$ and $t_j < C_2$, where C_2 is small enough that the peak (or trough) has not yet passed.

In our implementation we chose a combination of these methods in that we take the largest t that satisfies at least one of the above conditions. This seems to work better than any one method individually, especially in the presence of minor noise. Note also that certain reflections are oriented peak first, while others are trough first, thus in some cases C_2 is small enough that the trough has not yet passed.

We then use the difference between the return times of two reflections, multiplied by the speed of light in the medium (or vacuum, appropriately), to determine the additional distance traveled by the latter reflection. Namely, this is twice the distance between the two interfaces. In this manner we estimate d and, when possible, δ.

For small δ the two reflections are overlapping (see, for instance, Figure 2.12). In these cases we approximated the location of the start of the second reflection by the location of the trough. While this is a rough approximation, for this problem it was sufficient. In Problem 2 we will develop more sophisticated methods which could also be applied here.

2.3.3 Optimization of Least Squares Error

With these initial estimates to d and δ established, we now define our inverse problem to be: find $q = \{d, \delta\} \in Q_{ad}$ such that the following least squares error between the simulation and the observed data is minimized:

$$J(q) = \frac{1}{2MS} \sum_{j=1}^{M} \sum_{i=1}^{S} (E(t_i, z_j^O; q) - \hat{E}_{ij})^2. \tag{2.7}$$

Here the $\hat{E}_{ij}$ are measurements of the electric field taken at M specific locations (e.g. $z_1^O = 0$ and/or $z_2^O = 1$) and S distinct times (e.g., every $sr_e = 0.05ns$). The $E(t_i, z_j^O; q)$

are solutions of the simulations evaluated at the same locations and times corresponding to the data, $\hat{E}_{ij}$, and using parameter values q. The set Q_{ad} is the feasible set of q values determined such that d and δ are realistic (e.g., positive).

We apply an inexact Gauss-Newton iterative method to the optimization problem. That is, we re-write the objective function as

$$J(q) = \frac{1}{2MS} R^T R$$

where $R_k = (E(t_i, z_j^O; q) - \hat{E}_{ij})$ for $k = i + (j-1)M$ is the residual. To update our approximation to q we make the Inexact Newton update step $q_+ = q_c + s_c$ where

$$\begin{aligned} s_c &= -\left(R'(q_c)^T R'(q_c)\right)^{-1} \nabla J(q_c) \\ &= -\left(R'(q_c)^T R'(q_c)\right)^{-1} R'(q_c)^T R(q_c) \end{aligned}$$

is the step, q_c is the current approximation, and q_+ is the resulting approximation. This is an inexact method because we have disregarded the S Hessians of $(E(t_i, z_j^O; q) - \hat{E}_i)$, which is generally acceptable for small residual problems [K99].

In this simple case we have a 2×2 matrix inverse, so we can compute it explicitly. Each iteration requires one function evaluation and a forward difference gradient, which is two additional function evaluations (since we have two parameters). Each function evaluation is equivalent to a simulation. Therefore we want as few iterations as possible.

2.3.4 Convergence

Initial testing (with $z = 0$ data only) shows convergence to 8 decimal places of each parameter in 6 iterations of Gauss-Newton with initial guesses having at most 5% relative error in δ and 2% in d. The algorithm does not converge to the correct solution if the initial guess for d has 5% relative error or if the initial guess for δ has 10% relative error.

One reason that the algorithm fails to converge is that this objective function is poorly behaved. In Figures 2.14 and 2.15 we show plots of the objective function with respect to δ. The two very large peaks in J on either side of the exact minimizer are due to the simulated solution going in and out of phase with the exact solution. For this example, the simulated solution is most out of phase with the exact solution at $\delta = .181$ and $\delta = .219$ which correspond to the first and second peak in J respectively. The signal received at

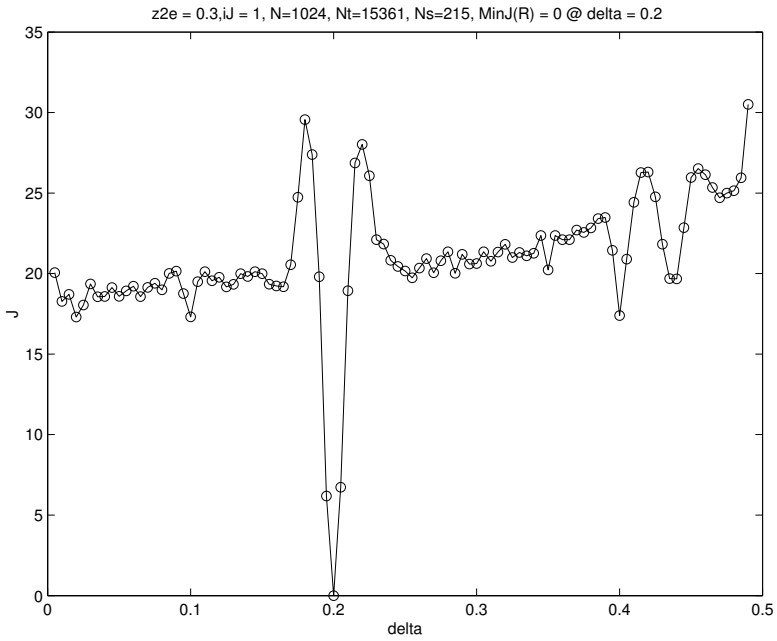

Figure 2.14: Nonlinear Least Squares objective function versus δ for a large range of δ values (data at $z = 0$ only)

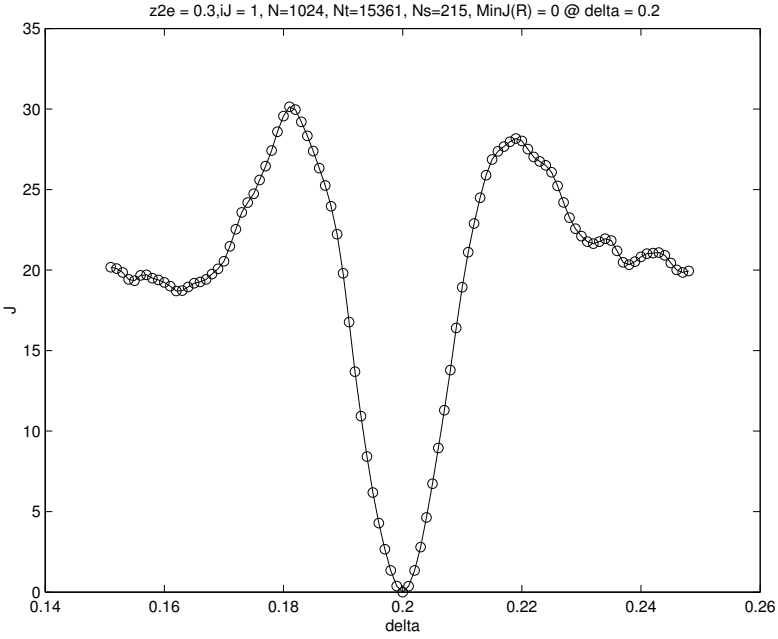

Figure 2.15: Nonlinear Least Squares objective function versus δ for a small range of δ values (data at $z = 0$ only)

$z = 0$ for these two δ values are plotted versus the actual signal with $\delta = .2$ in Figures 2.16 and 2.17. The same phenomenon occurs in the d direction, for the same reasons.

One may consider adding the information at the $z = 1$ signal to the least squares objective function hoping to lessen the effects of the peaks in J. But as demonstrated in Figures 2.18 and 2.19, which depict the objective function using both signals and using just the $z = 1$ signal respectively, the out of phase phenomena is still present.

Very few optimization routines can expect global convergence without having initial estimates between the two peaks in J. The effective convergence region for this objective function applied to this problem (with or without observations at $z = 1$) is within about 8% of the actual value of δ when d is exact and within about 7.5% of the actual value of d when δ is exact.

Note also that the convergence region is very dependent on the frequency of the interrogating signal; for higher frequencies, the region is even smaller. This is because the distance between the two peaks in J is linearly dependent on λ, the wave length of the interrogating signal. This has profound implications for our desire to interrogate with signals in the terahertz range.

Further, this is considering only a one parameter minimization problem with the other parameter held fixed at the exact solution. Convergence is much worse for the actual two parameter problem. The difficulties with the least squares objective function in this problem are clearly visible in the surface plots shown in Figures 2.20 and 2.21. This explains why d has a smaller convergence region, since J is much more sensitive to d. Also we see that there are peaks in J in the d direction as well.

The diagonal "trench" occurs approximately along the line

$$d = -\frac{1}{2}(\delta - \delta^*) + d^* \tag{2.8}$$

(where * denotes the exact solution). This happens because when the depth d is decreased by, say a, the z_1 and z_2 reflections of the simulation no longer correspond with those of the data (think of the two overlapping reflections at $t = 1.5ss$ in Figure 2.12 being shifted slightly to the left in some simulation).

With d decreased by a we must increase δ to try to compensate and get as much of the signal from the simulation to correspond with the data. Since δ only affects the z_2 reflection, it is clear that the z_1 reflections will not correspond. If δ is increased so that the distance traveled by the z_2 reflection is increased by b, then we will need for the time

required for a signal to travel a distance a in the material to be equal to the time required for a signal to travel a distance b in a vacuum. Since the distance traveled by the z_2 reflection is twice that of the increase in δ, we compute the increase in δ to be $\sqrt{\epsilon_\infty}a$. In our case $\epsilon_\infty = 5.5$, so the increase is $2.3452a$. This explains the slope of approximately $-\frac{1}{2}$ in the relationship (2.8).

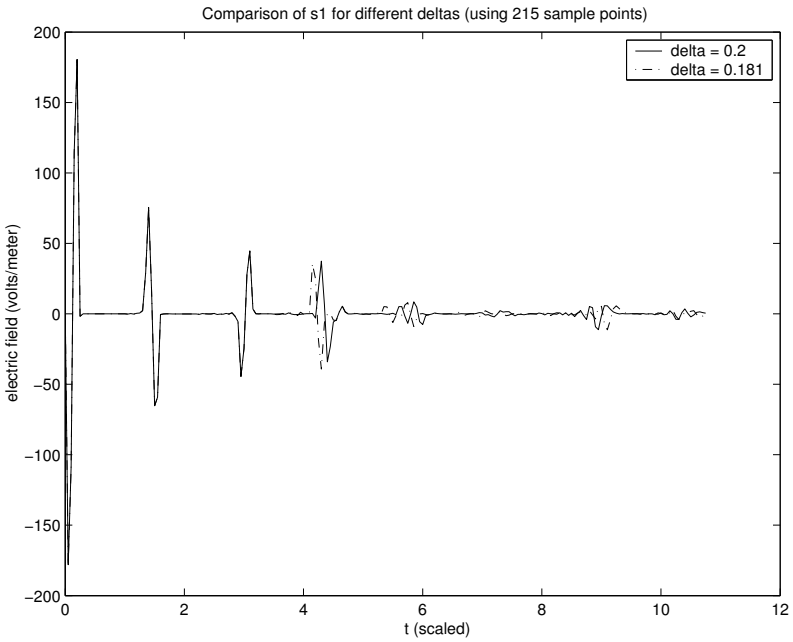

Figure 2.16: Signal received at $z = 0$ for two different values of δ demonstrating the simulation going out of phase on the left with the data signal

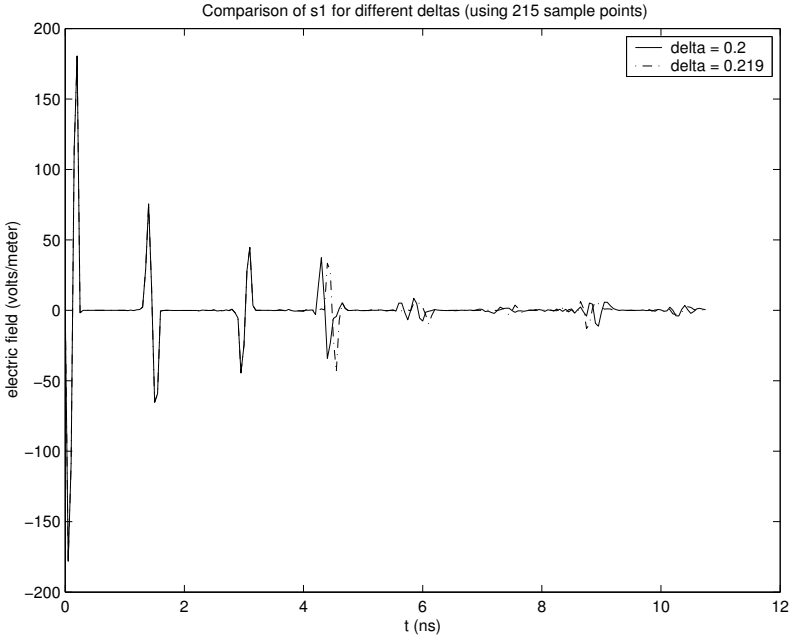

Figure 2.17: Signal received at $z = 0$ for two different values of δ demonstrating the simulation going out of phase on the right with the data signal

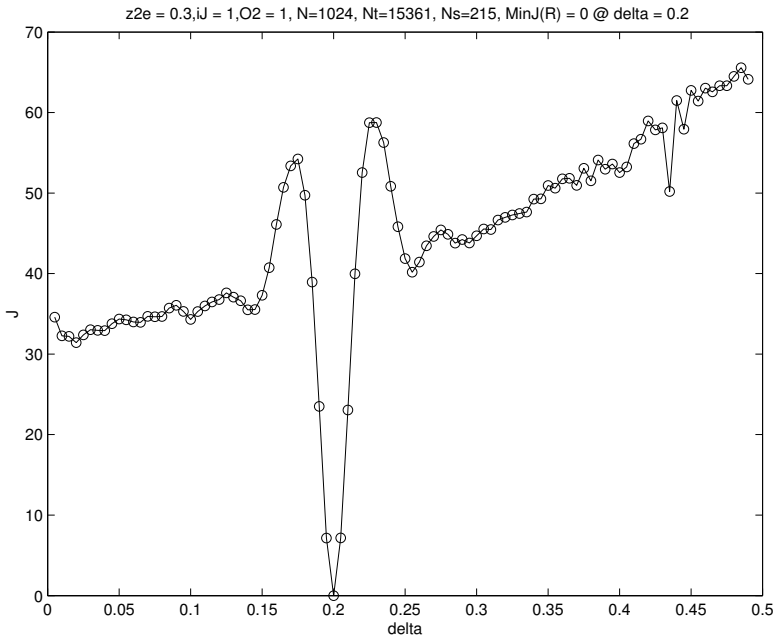

Figure 2.18: Nonlinear Least Squares objective function, using signals received at both $z = 0$ and $z = 1$, versus δ

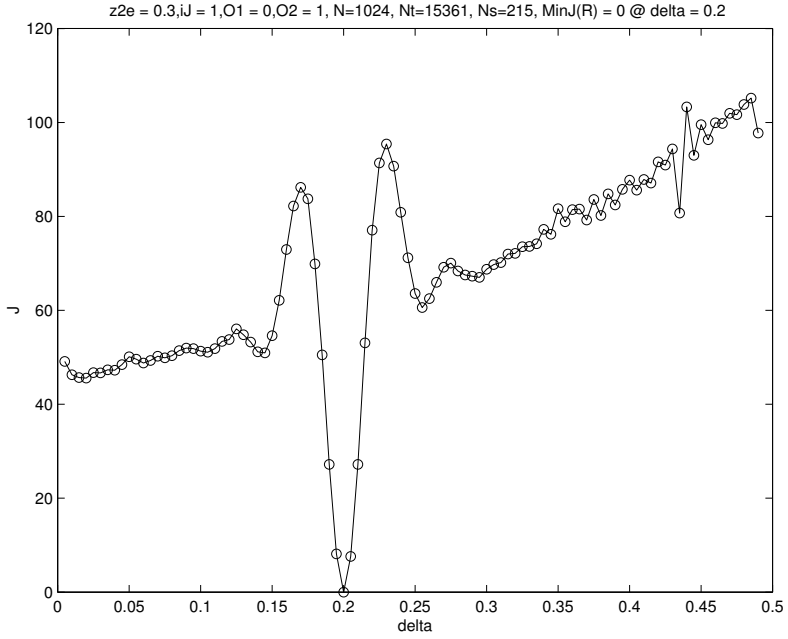

Figure 2.19: Nonlinear Least Squares objective function, using signals received at $z = 1$ only, versus δ

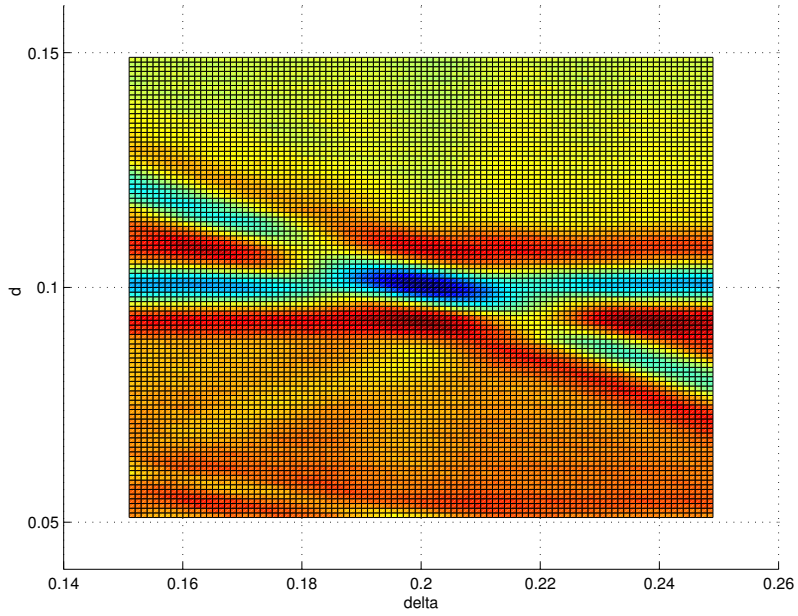

Figure 2.20: Nonlinear Least Squares objective function (J) versus δ and d projected to $2D$ (data at $z = 0$ only)

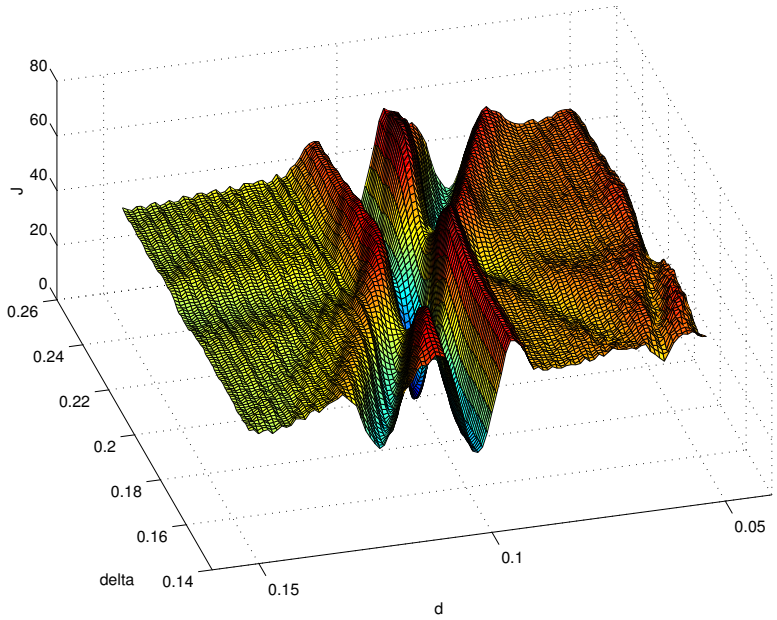

Figure 2.21: Nonlinear Least Squares objective function (J) versus δ and d in $3D$ (data at $z = 0$ only)

2.3.5 An Improved Objective Function

As demonstrated above, the usual Nonlinear Least Squares objective function has two large peaks in J on either side of the exact minimizer. The reason for these peaks in J is that the simulated solution goes in and out of phase with the data as d or δ change. When they are precisely out of phase, there is a very large absolute error, which when squared, causes the objective function to have large peaks. Therefore, one solution is to not consider the absolute error, but instead the error between the absolute values, i.e., the following objective function:

$$J_2(q) = \frac{1}{2S} \sum_{i=1}^{S} \left(|E(t_i, z_i^O; q)| - |\hat{E}_i| \right)^2. \tag{2.9}$$

This will prevent the fact that the signals go in and out of phase with each other from having an impact on the objective function, since positive magnitudes cannot cancel each other out. This gives a more accurate measure of the difference between two signals. Note that $J_2(q)$ is not differentiable on a set of measure zero; this is very unlikely to affect the finite difference computations of the gradients, and did not seem to present problems in our testing. We plot $J_2(q)$ versus δ in Figures 2.22 and 2.23.

Note that while we have effectively eliminated the peaks on either side of the exact solutions, in essence we have merely converted them to local minima! But, since the minima occur for the same reasons the peaks in J had been occurring, they occur at the same values of δ. Note that we can see from plotting the signals that they were exactly out of phase when they were shifted by about $\frac{\lambda}{4}$, where λ is the wavelength of the interrogating signal. Therefore δ is off by $\frac{\lambda}{4}$. Since we determine the frequency of the interrogating signal, this is a known quantity, and we can predict where these local minima will occur a priori!

Most optimization routines will continue until they find a local minimum, and since the two false minima described above are at least close to "predictable" locations, we can easily test on either side of any detected minimum to determine if it is in fact global. If J_2 is less at a fixed distance in the δ direction (e.g., $\frac{\lambda}{4}$) on either side of a detected minimum, i.e., at either *test location* of the local minimum, we restart Gauss-Newton at the new best guess. Thus if either of the two local minima described above is found, we will eventually have global convergence if one of their *test locations* in sufficiently close to the global minimizer.

To graphically demonstrate this approach, we have added dotted and dash-dotted

lines to the graph of $J_2(\delta)$ in Figure 2.23 to represent the test values of the first and second local minima respectively. One can clearly see that if either local minimum is detected, the test value either to its right if it is the first one, or to its left if it is the second, will give a smaller J_2 and should eventually lead to the global minimizer being detected. Using this method we have in principle increased our convergence region to about 25% of δ when d is exact.

Our objective function also has local minima in the d direction, as demonstrated in Figure 2.24. Again they are in predictable locations, being at roughly $d^* \pm \frac{\lambda}{4\sqrt{\epsilon_\infty}}$, where d^* represents the global minimizer. Thus, if we know λ and ϵ_∞ (which we should), then we can determine exactly where to test for the global minima once a local minimum has been found. Using the above method, we have in principle increased the d convergence region from about 7.5% to about 15% when δ is exact.

Other possible modifications to the Least Squares objective function having similar effects include squaring the signal instead of taking the absolute value (thus preserving smoothness everywhere), or just halving the reference signal so that we only have a positive amplitude to begin with. Each of these options will still have the local minima problems described above, as well as their own unique disadvantages.

In addition to the two new minima created above, we still have other local minima to deal with which are present in both formulations of the objective function. Some of these local minima can be reduced by using a smaller mesh size (more finite elements) since they are the result of numerical error (see Figures 2.25 and 2.26).

All of the above discussions and Figures 2.22 through 2.26 involve J_2 with observations only at $z = 0$. We have also done tests using only the $z = 1$ transmitted data in the objective function from (2.9) (see Figure 2.27). Clearly this function does not have the same problem of the third reflections (since $z = 1$ only sees the even numbered reflections). But it does still have a very deep and significantly close local minima of its own. This minimum is caused by the same type of problem that causes the $z = 0$ minimum. However, we have found that by combining both $z = 0$ and $z = 1$ data in the objective function J_2 we can obtain much better results since their deficiencies somewhat average out (see Figure 2.28).

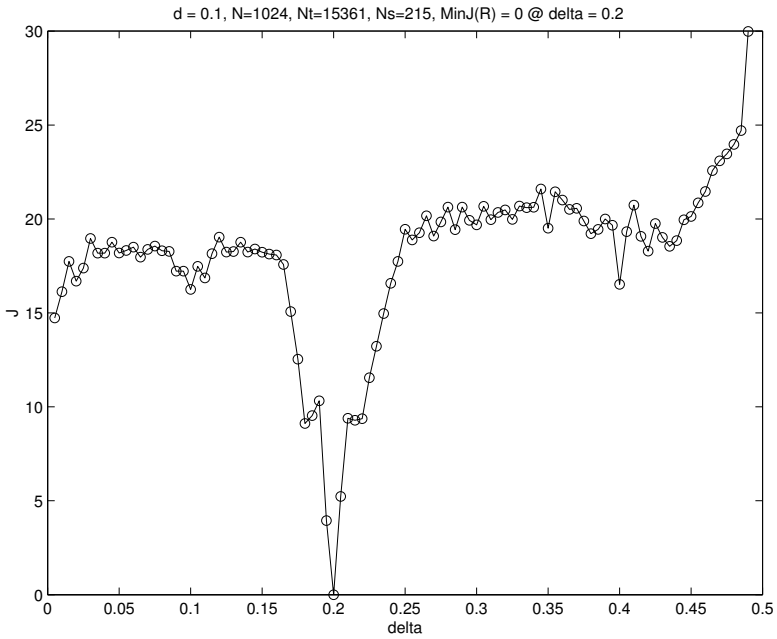

Figure 2.22: Our modified Nonlinear Least Squares objective function (J_2) versus δ for a large range of δ values

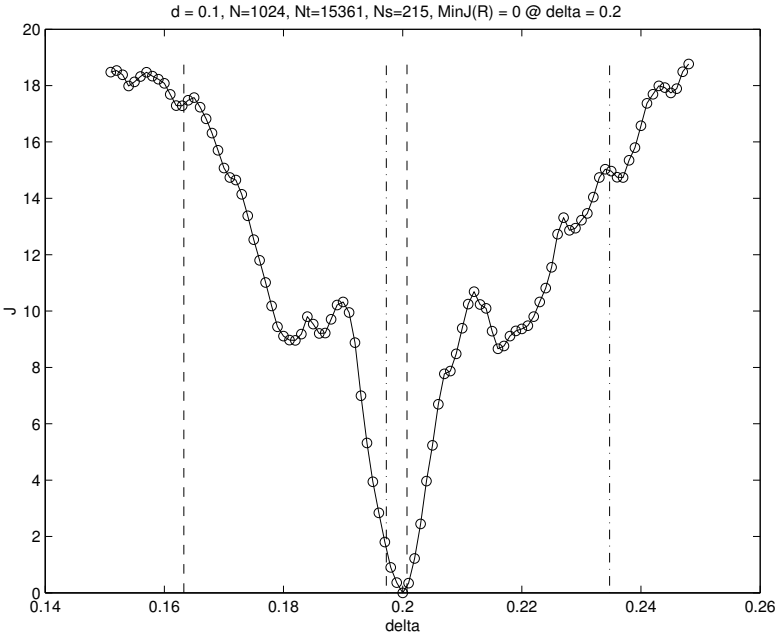

Figure 2.23: Our modified Nonlinear Least Squares objective function (J_2) versus δ for a small range of δ values. The dotted lines represent the delta values that will be tested if a local minimum is found

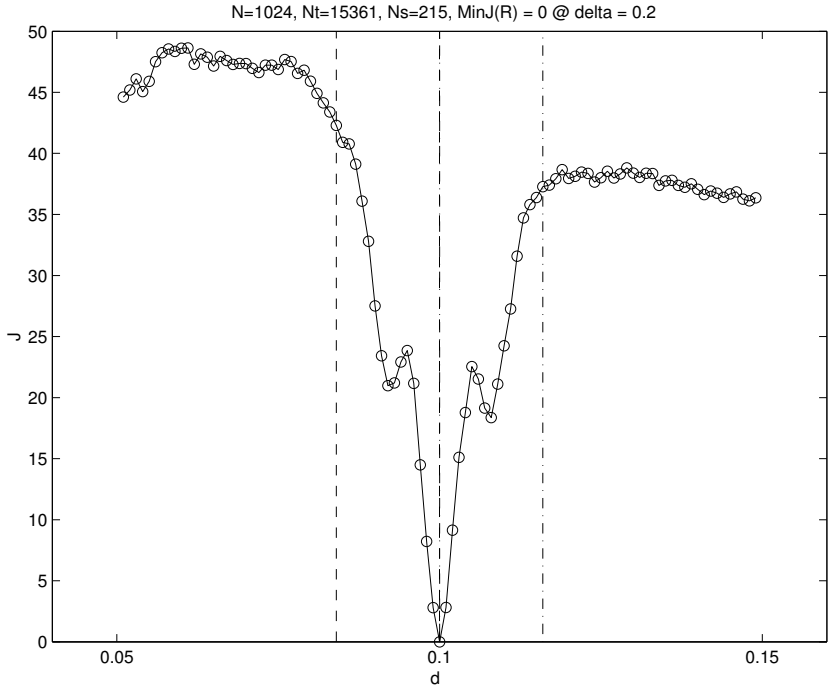

Figure 2.24: Our modified Nonlinear Least Squares objective function (J_2) versus d for a small range of d values. The dotted lines represent the delta values that will be tested if a local minimum is found

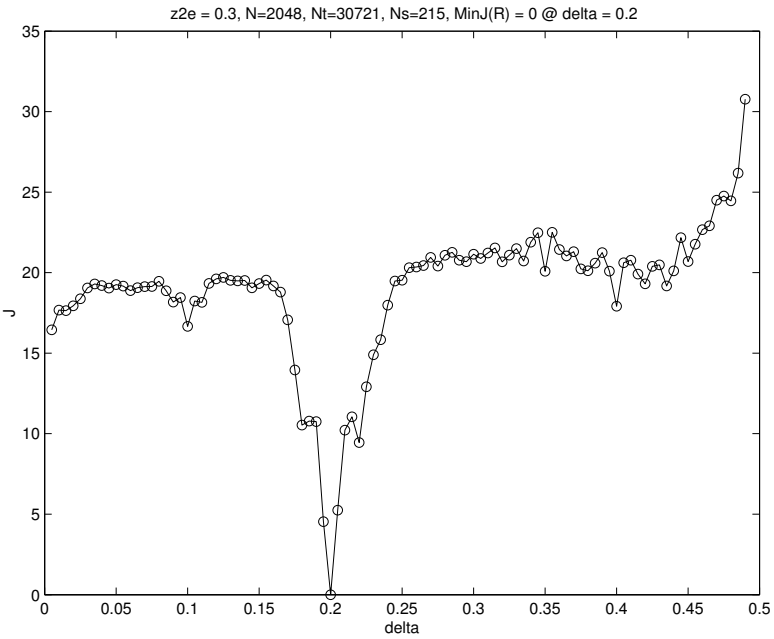

Figure 2.25: Our modified Nonlinear Least Squares objective function (J_2), using a simulation with twice as many meshes, versus δ for a large range of δ values

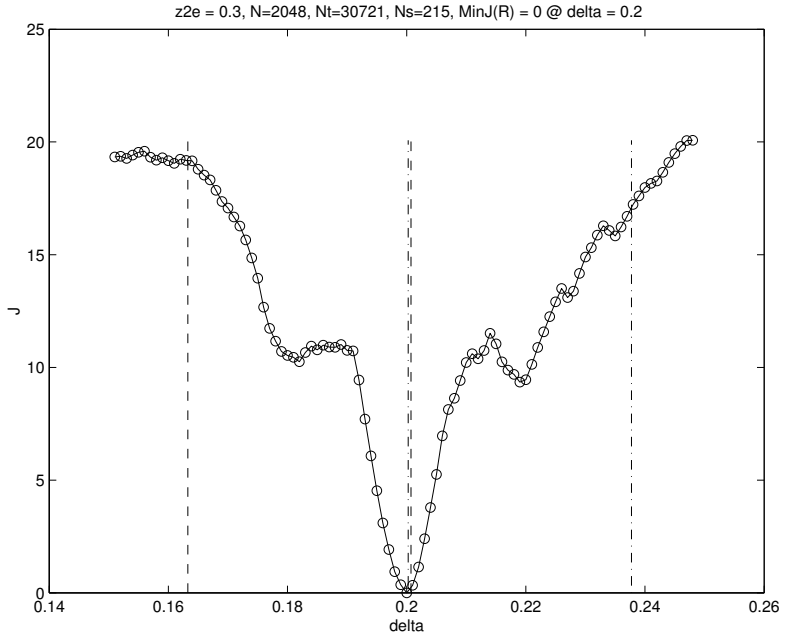

Figure 2.26: Our modified Nonlinear Least Squares objective function (J_2), using a simulation with twice as many meshes, versus δ for a small range of δ values. The dotted lines represent the delta values that will be tested if a local minimum is found

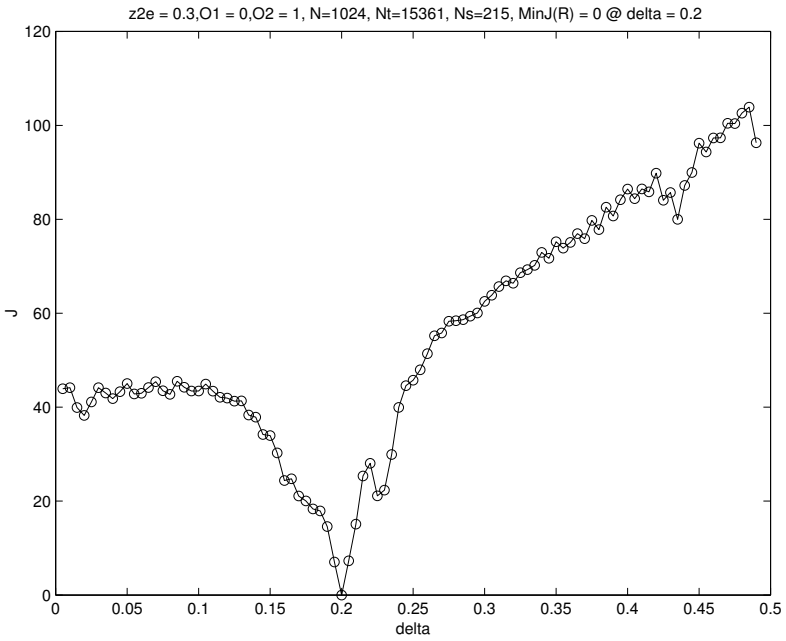

Figure 2.27: Our modified Nonlinear Least Squares objective function (J_2), using the signal received at $z = 1$ only, versus δ for a large range of δ values

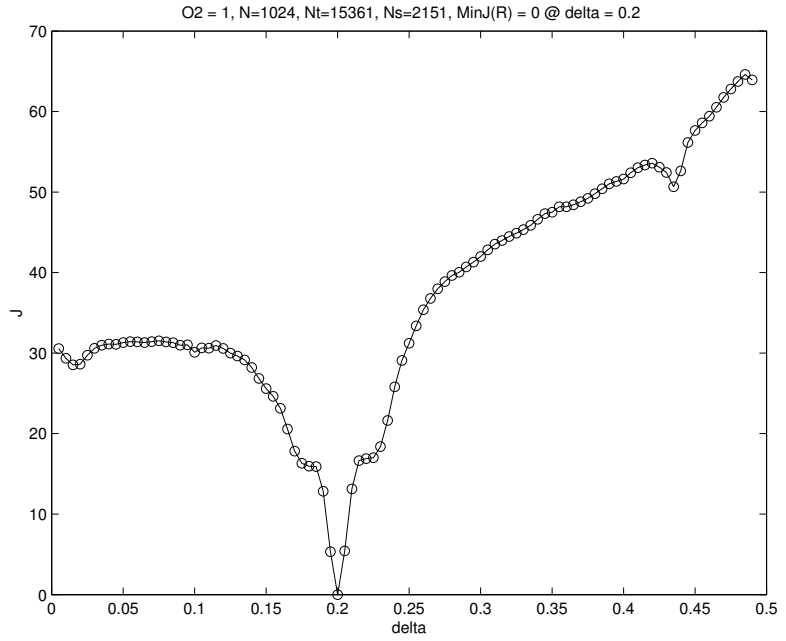

Figure 2.28: Our modified Nonlinear Least Squares objective function (J_2), using the signal received at $z = 0$ and $z = 1$, versus δ for a large range of δ values

2.3.6 Testing J_2

In order to determine the limitations of an optimization routine to minimize our objective function J_2 in a more practical setting we examine J_2 versus q when error is present. In particular we try both adding random noise to the data signal, as well as testing bad initial guesses for δ and d. It should be noted that although we have previously established that there are certain benefits to having data at $z = 1$ in the tests reported on below we assume that it is not available and used only observations at $z = 0$.

2.3.7 Sensitivity to Initial Guesses

For J_2 described in (2.9) we compute a surface plot for various δ and d values, which is shown in Figures 2.29 and 2.30. We notice immediately that the objective function is much more sensitive to d than to δ, therefore it is imperative that our initial guess for d is as good as possible.

To give an idea of what may happen if our d guess were not within the 5% our testing has determined is necessary, we plot the objective function versus δ for three values of d, which are 3%, 15%, and 30% off respectively, in Figures 2.31, 2.32, and 2.33.

It is clear that the 15% case should have no trouble converging with relatively good initial guess for δ, but even if the initial value for δ were exact, the 30% case could quite possibly converge to the minimum at the far left of Figure 2.33. It may be surprising that there should be a minimum for very small δ values at all, even more so that it is in fact the global minimum! This can be explained by first remembering that, for example in the 15% case, the original data was computed with $d = .1$ but the simulations used $d = .085$, so we should expect that regardless of δ there is a part of the simulated signal that will not match the data, namely the first reflection. Thus the first reflection of the data is not matched by the simulation, unless δ is small enough to match it, e.g. $\delta = .035$, and this is exactly what is happening, as displayed in Figure 2.34. Figure 2.35 depicts the other local minimum of the 15% case where the z_3 reflection of the simulation does match the z_3 reflection of the data.

Notice that the distance between the two minimum values of δ (see for example Figure 2.32 or 2.33) is exactly $\delta^* = 0.2$, which is what would be expected. However, we cannot apply the same idea as before where we add or subtract a fixed amount to test for

other local minima, since for one, the "more optimal" of the two is farther from the "true" solution, and also, we would have to know δ in the first place to add or subtract it, but that is what we are trying to estimate!

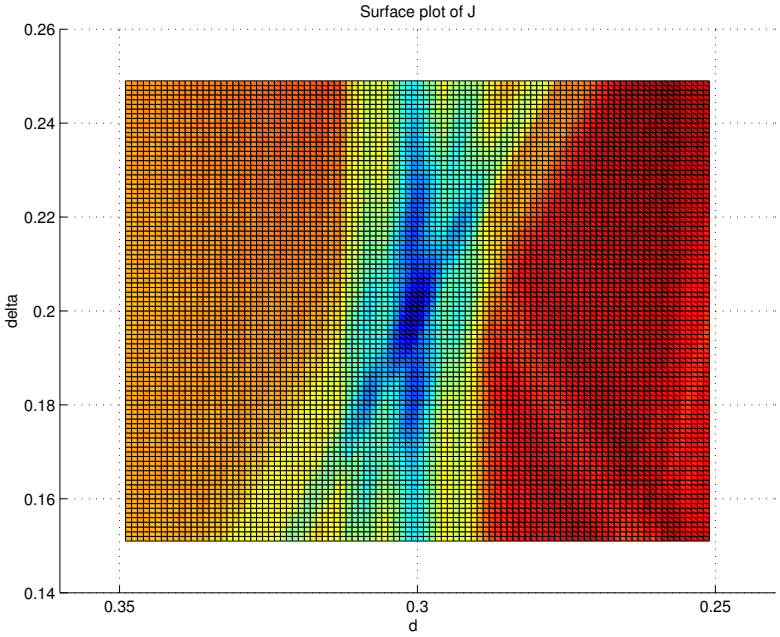

Figure 2.29: Our modified Nonlinear Least Squares objective function (J_2) versus δ and d projected to $2D$

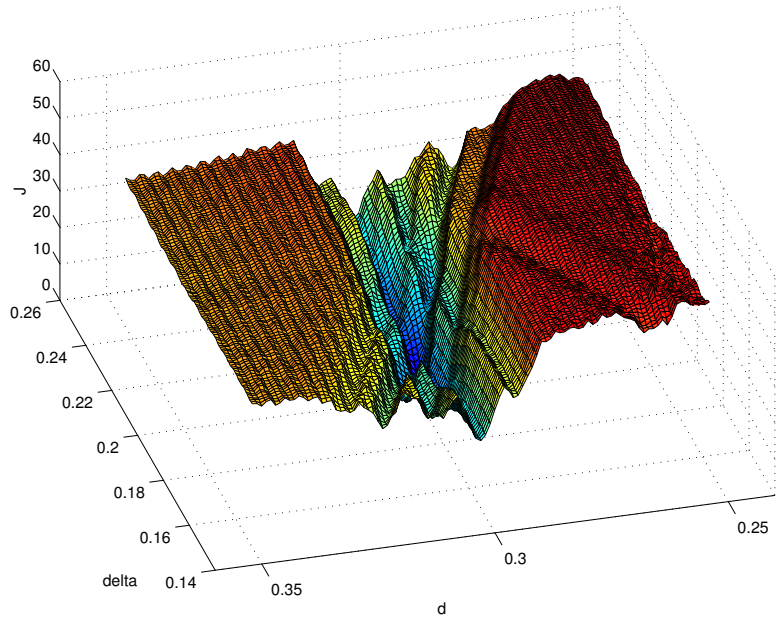

Figure 2.30: Our modified Nonlinear Least Squares objective function (J_2) versus δ and d in $3D$

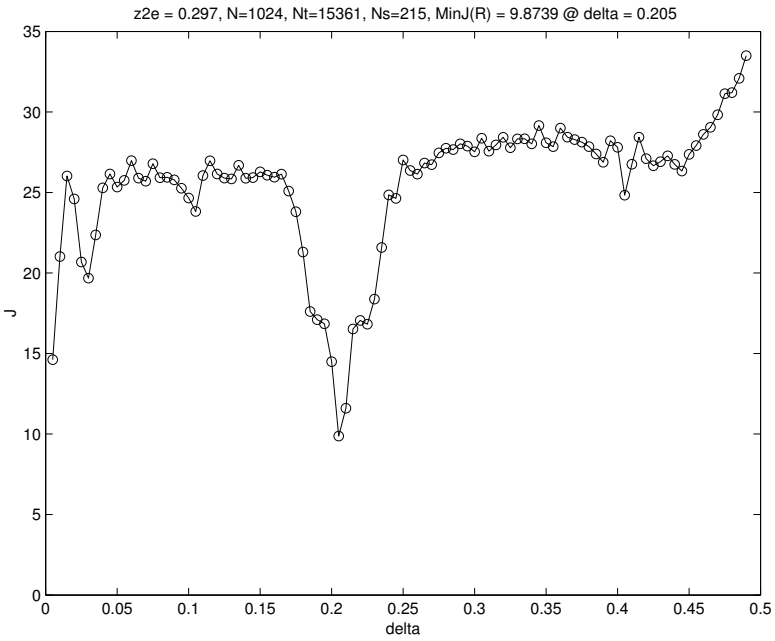

Figure 2.31: Our modified Nonlinear Least Squares objective function (J_2) versus δ with $d = .097$ (representing 3% relative error)

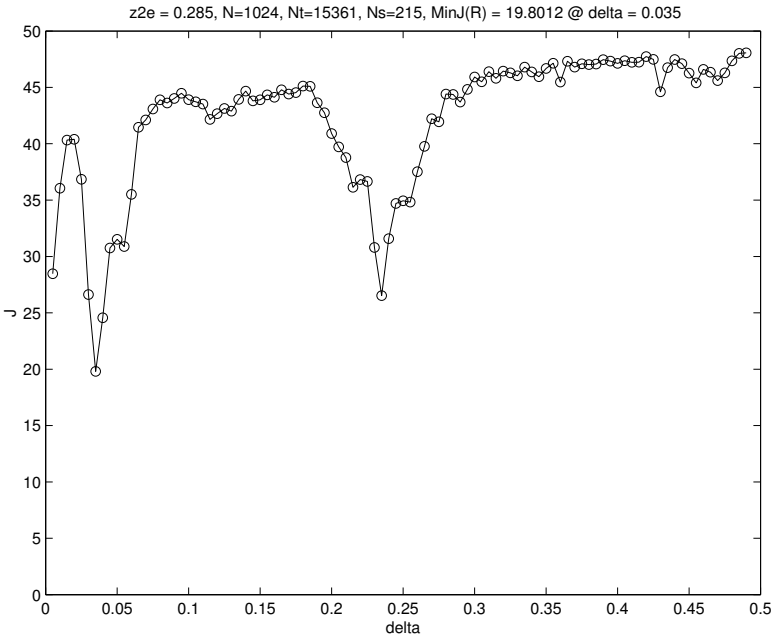

Figure 2.32: Our modified Nonlinear Least Squares objective function (J_2) versus δ with $d = .085$ (representing 15% relative error)

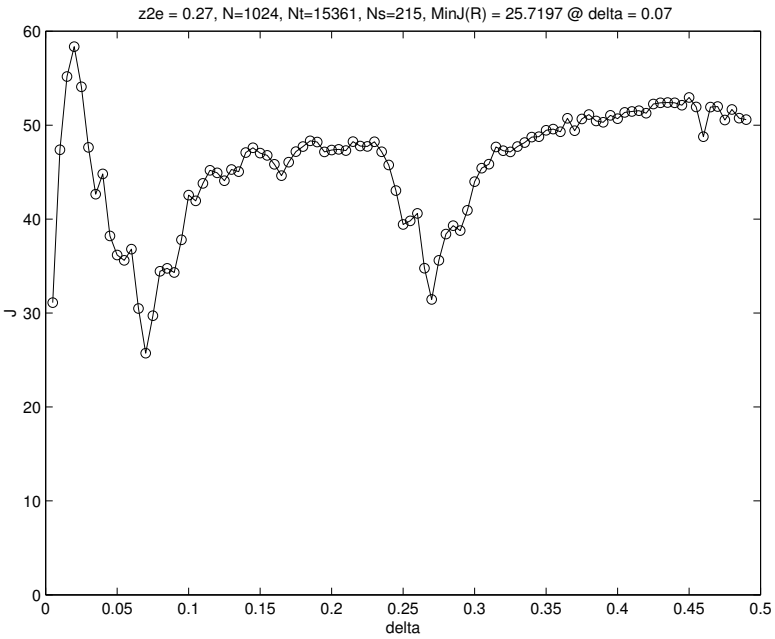

Figure 2.33: Our modified Nonlinear Least Squares objective function (J_2) versus δ with $d = .07$ (representing 30% relative error)

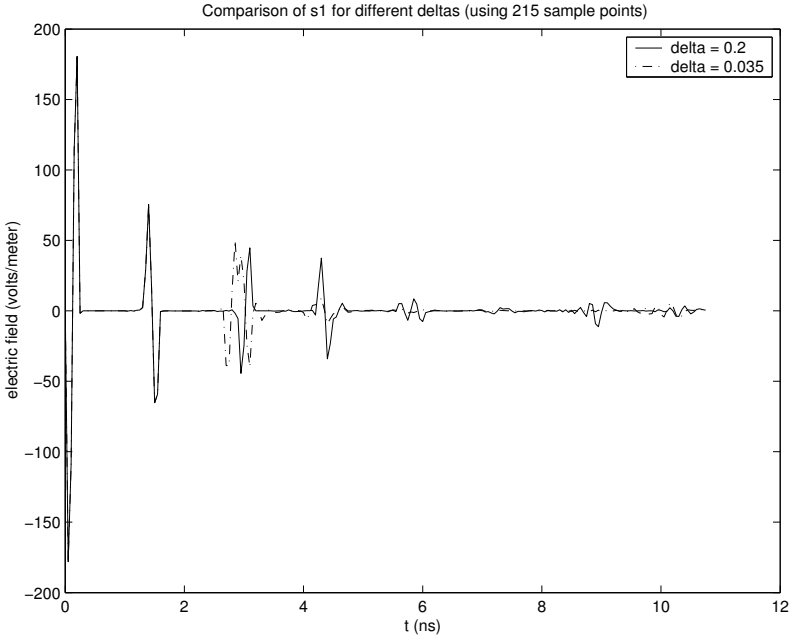

Figure 2.34: Signals received at $z = 0$ (where $(d, \delta) = (.1, .2)$ corresponds to the given data and $(d, \delta) = (.085, .035)$ corresponds to the simulation) demonstrating the z_2 reflection of the simulation corresponding to the z_1 reflection of the data

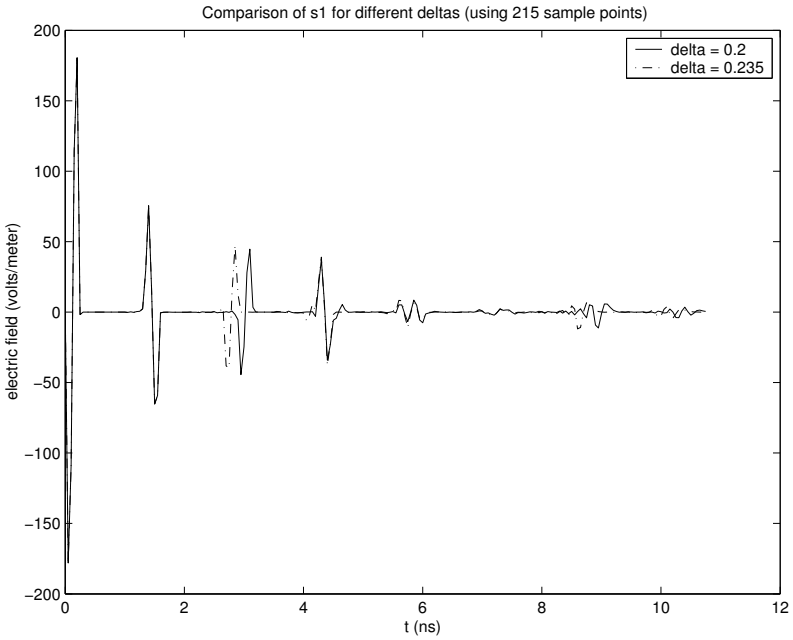

Figure 2.35: Signals received at $z = 0$ (where $(d, \delta) = (.1, .2)$ corresponds to the given data and $(d, \delta) = (.085, .235)$ corresponds to the simulation) demonstrating the z_2 reflection of the simulation matching the z_2 reflection of the data and ignoring the z_1 reflection

2.3.8 Random Observation Noise

In order to test the feasibility of this procedure as an estimation method, we have produced synthetic data for our observations $\hat{E}_i$. In an actual experiment, one must assume that the measurements are not exact. To simulate this we have added random noise to the original signal. The absolute value of the noise is relative to the size of the signal. If E_i is the data sampled, then we define $\hat{E}_i = E_i(1 + \nu\eta_i)$, where η_i are independent normally distributed random variables with mean zero and variance one. The coefficient ν determines the relative magnitude of the noise as a percentage of the magnitude of E_i, in particular, $\nu = 0.05$ corresponds to 10% noise and $\nu = 0.025$ to 5% noise.

Plots of the resulting objective functions for various values of ν ranging from 2% to 40% are shown in Figures 2.36-2.41. We notice that the structure of the curves is not significantly affected, nor is the location of the global minimum. However the magnitude of the objective function is increased, making Inexact Newton methods slightly less reliable due to the larger residual. Still, our results show that the minima were consistently found and within a reasonable amount of time. Select examples are summarized in Table 2.2.

Table 2.2: Number of Iterations and CPU Time for Gauss-Newton given various relative magnitudes of random error.

ν	d	δ	J	Iterations	CPU Time (s)
0	0.1	0.2	1.32319E-10	7	160
0.01	0.099994	0.199969	0.00792792	8	186
0.05	0.099974	0.199835	0.199489	13	291
0.2	0.099928	0.199204	3.04619	20	435

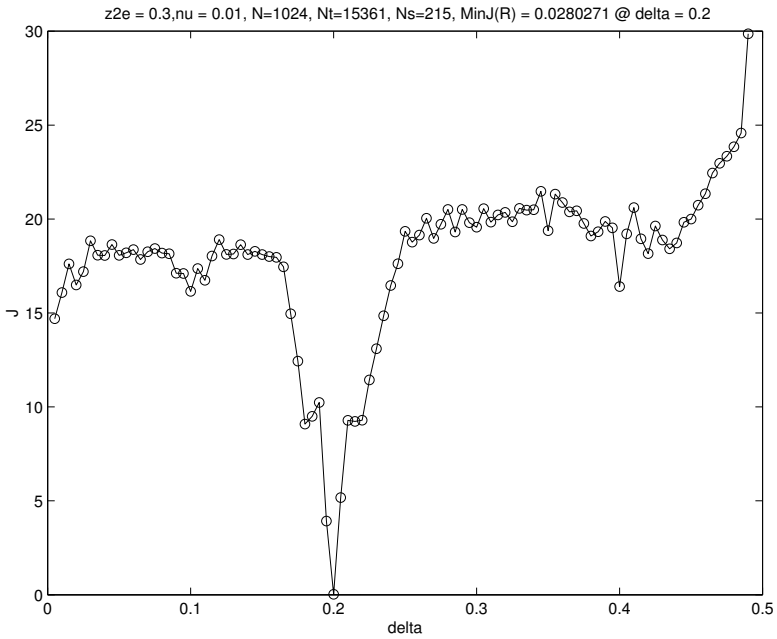

Figure 2.36: Our modified Nonlinear Least Squares objective function (J_2), with 2% random noise, versus δ for a large range of δ values

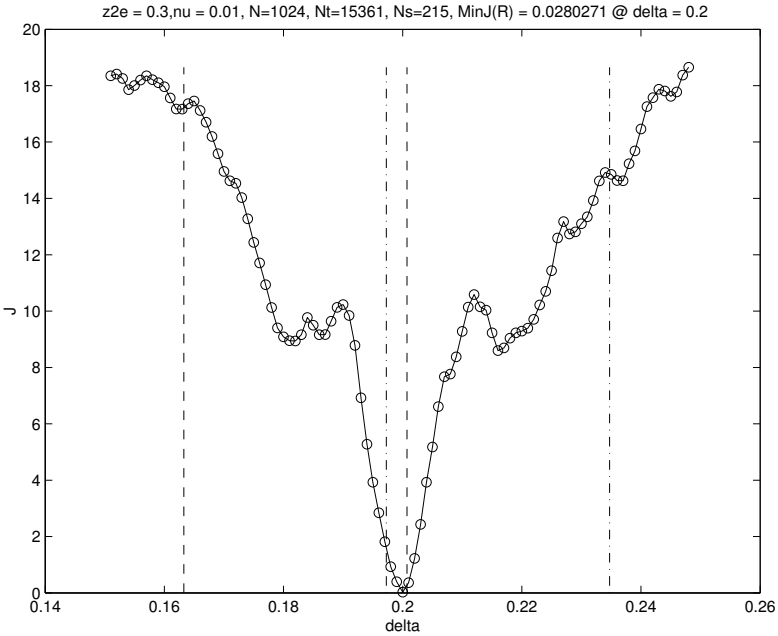

Figure 2.37: Our modified Nonlinear Least Squares objective function (J_2), with 2% random noise, versus δ for a small range of δ values

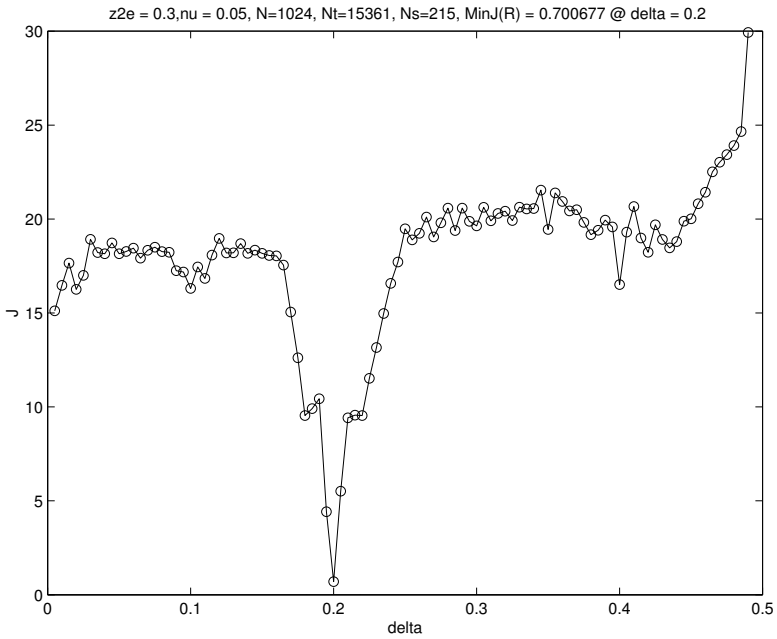

Figure 2.38: Our modified Nonlinear Least Squares objective function (J_2), with 10% random noise, versus δ for a large range of δ values

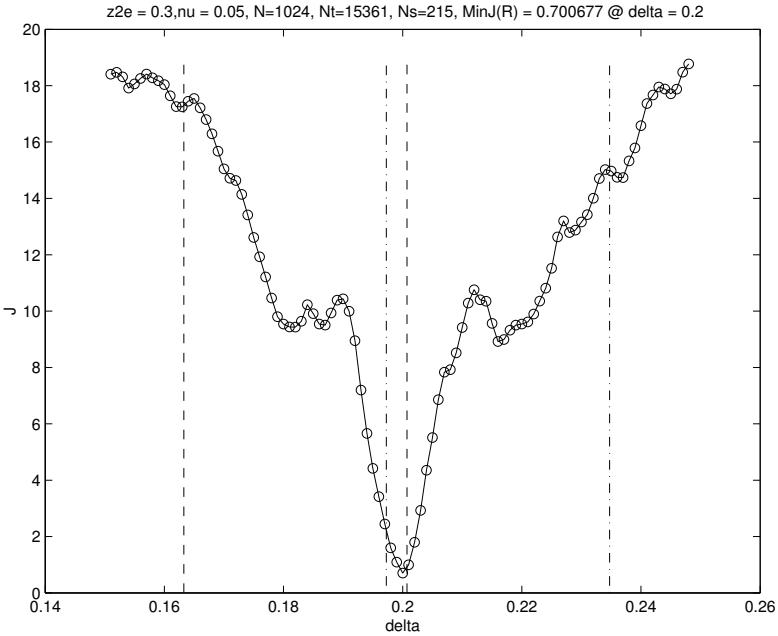

Figure 2.39: Our modified Nonlinear Least Squares objective function (J_2), with 10% random noise, versus δ for a small range of δ values

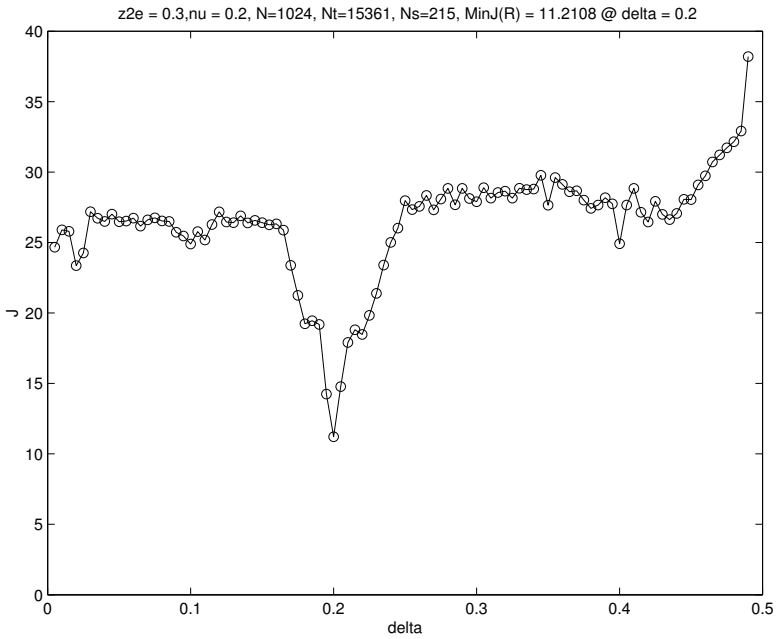

Figure 2.40: Our modified Nonlinear Least Squares objective function (J_2), with 40% random noise, versus δ for a large range of δ values

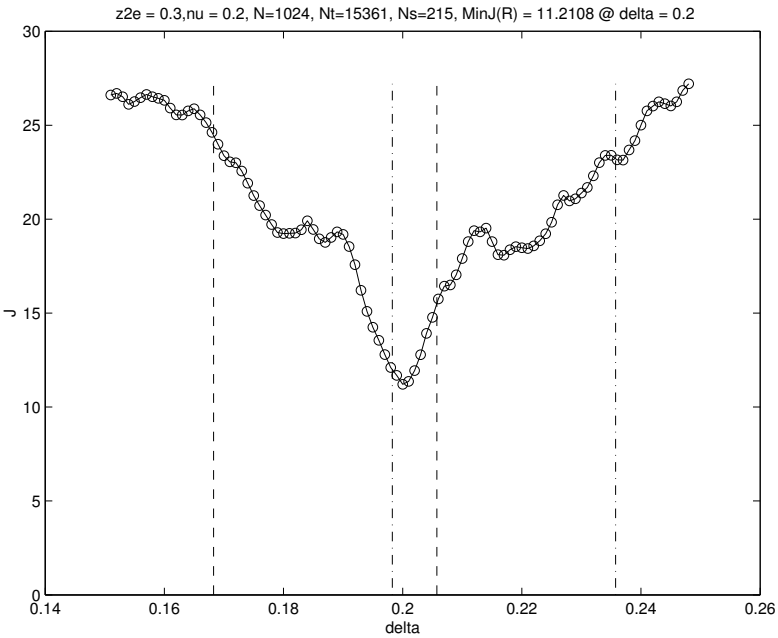

Figure 2.41: Our modified Nonlinear Least Squares objective function (J_2), with 40% random noise, versus δ for a small range of δ values

2.4 Problem 2

We next apply the most useful techniques obtained from the investigations of Problem 1 to a new formulation of the interrogation problem. In Problem 2 we consider a dielectric slab and a metallic backing (conductor) with a possible gap between the two (see Figures 2.42 and 2.43). Applications of this specific formulation include detecting delamination (separation) of insulation from metallic containers, e.g., insulating foam on a space shuttle fuel tank. In order for this numerical approach to be useful in this particular application we must be able to resolve a gap width of $.2mm$ inside of a slab with a thickness of at least $20cm$ and a frequency of $100GHz$.

We will again assume the same physical parameters for our dielectric and consider the gap as a vacuum. The variables d and δ are still the depth and the width of the gap respectively. One major difference is that in this problem we are only able to detect the electromagnetic signal in front of the material. Also, since the metallic backing reflects much of the signal, we have considerably more overlapping of the reflections to worry about. These properties contribute to the fact that this formulation leads to a much more difficult inverse problem. For this reason we will be using a more sophisticated optimization routine including a Levenberg-Marquardt parameter and Implicit Filtering. We will also need to develop different approximation methods for our initial guesses.

The implementation of this problem has several minor differences from the previous one. First, we now only need to represent two interfaces $\tilde{z_1}$ and $\tilde{z_2}$, with $\tilde{z_0}$ and $\tilde{z_3}$ being the front and back computational boundaries, respectively. Thus now we define the depth of the gap as $d := \tilde{z_2} - \tilde{z_1}$ and the width as $\delta := \tilde{z_3} - \tilde{z_2}$. Also, as previously mentioned, the conductive metal backing reflects the signal, and hence we must change our absorbing boundary conditions at $z = 1$ (for a finite computational domain), to a Dirichlet boundary condition ($E = 0$). We must modify our finite element matrices accordingly, as well. Otherwise, the numerical method for simulation is the same as it was for Problem 1, namely standard finite element methods for spatial derivatives, and an alternating implicit/explicit centered difference time stepping scheme. Sample solutions are plotted in Figure 2.44.

We again define our inverse problem to be: find $q := \{d, \delta\} \in Q_{ad}$ such that an objective function representing the error between the simulation and the observed data is minimized:

$$\min_{q \in Q_{ad}} J(q).$$

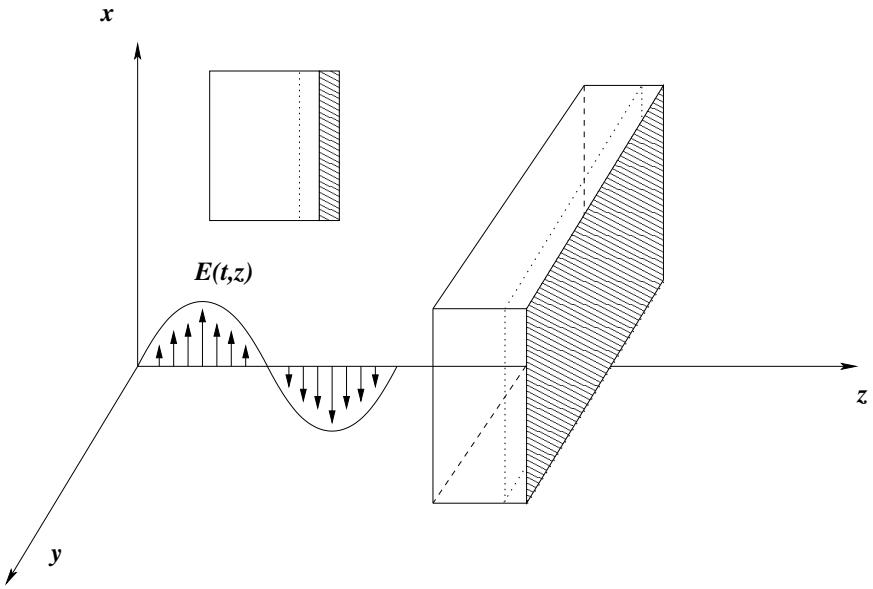

Figure 2.42: Schematic of Problem 2: determining the depth and width of a gap between a dielectric slab and a metallic backing

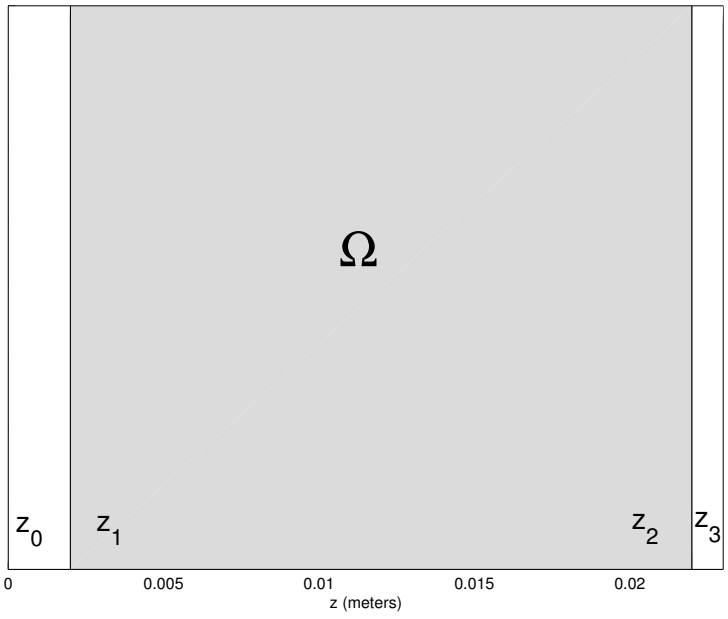

Figure 2.43: The domain of the material slab with a gap between the medium and a metallic conductive backing: $\Omega = \{z | z_1 \leq z \leq z_2\}$.

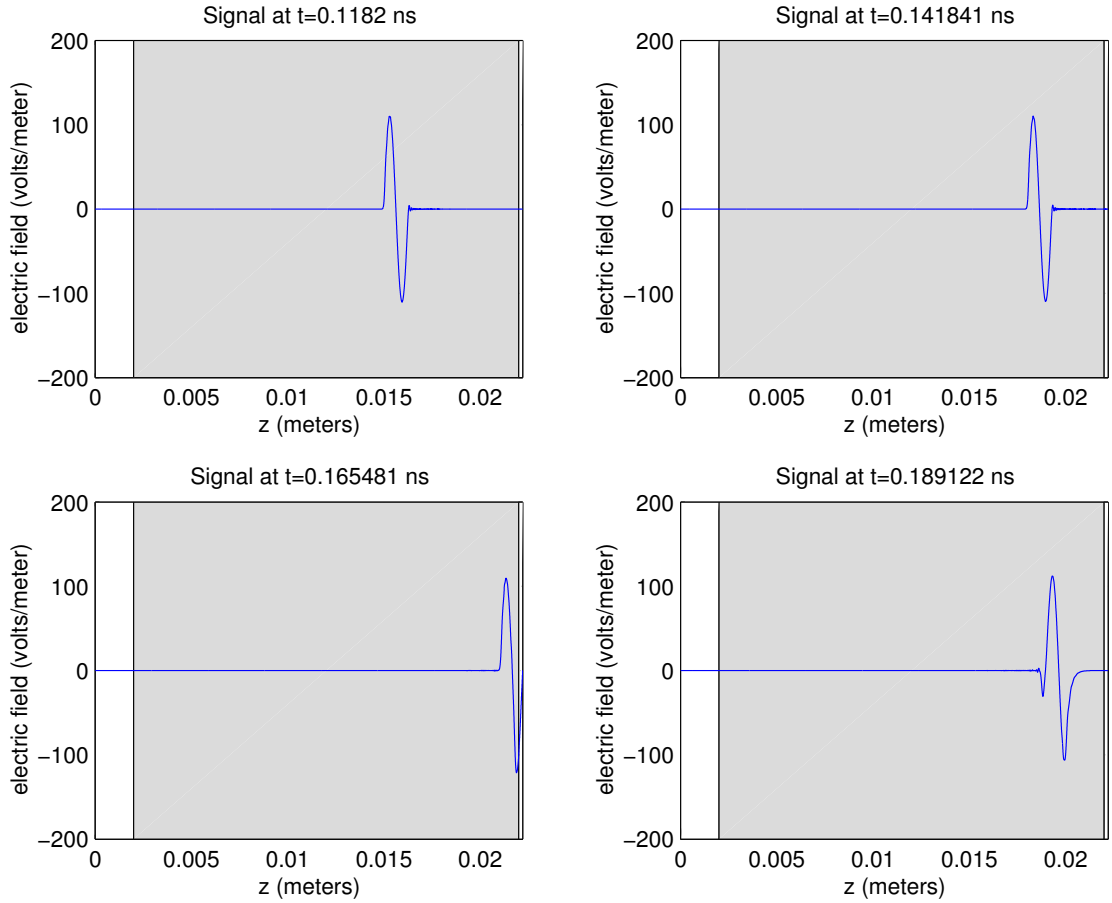

Figure 2.44: Computed solutions at different times of a windowed electromagnetic pulse incident on a Debye medium with a crack between the medium and a metallic conductive backing. The width of the slab is $d = .02m$ and the width of the gap is $\delta = .0002$ (barely visible at the far right of the gray region).

Here the measurements of the electric field, $\hat{E}_i$, are taken only at $z = 0$, but still at S distinct times (e.g., every $0.06ps$). The solutions of the simulations, $E(t_i, 0; q)$, computed using parameter values q, are evaluated at the same location and times corresponding to the given data. In lieu of actual data from experiments, we again create our observed data by using the simulator, however, the only information that is given to the minimizer is the data observed at $z = 0$, which we will denote by $\hat{E}$.

The system that we use to represent the propagation of the electric field, and thus simulate in order to solve our inverse problem, is as follows, and includes the above

mentioned Dirichlet condition at $z = 1$:

$$\begin{aligned}
\mu_0\epsilon_0(1 + (\epsilon_\infty - 1)I_\Omega)\ddot{E} + \mu_0 I_\Omega \ddot{P} + \mu_0\sigma\dot{E} - E'' &= -\mu_0\dot{J}_s && \text{in } \Omega \cup \Omega_0 \\
\tau\dot{P} + P &= \tau\epsilon_0(\epsilon_s - \epsilon_\infty)E && \text{in } \Omega \\
[\dot{E} - cE']_{z=0} &= 0 \\
[E]_{z=1} &= 0 \\
E(0, z) &= 0 \\
\dot{E}(0, z) &= 0
\end{aligned}$$

with

$$J_s(t, z) = \delta(z)sin(\omega t)I_{[0,t_f]}(t).$$

See Section 2.1 for a complete description.

2.4.1 Objective Function

As in the previous problem, we encounter difficulties when attempting to use the standard Least Squares objective function to compute the error between the simulated signal and the observed data. The constructive interference of peaks and troughs produces peaks in J, the objective function, on all sides of the global minimum which make it nearly impossible to find the solution in the middle. The peaks in J in the d direction are clearly apparent in Figure 2.45. In contrast, Figure 2.46 depicts a surface plot of our modified least squares objective function

$$J_2(q) = \frac{1}{2S}\sum_{i=1}^{S}\left||E(t_i, 0; q)| - |\hat{E}_i|\right|^2.$$

Remark 3 *The gradual slope down and to the left in the surface plots is due to the increased attenuation of signals as the depth is increased. Also, the drop off at large depth values is an artifact of having a finite end time for collecting data, i.e., the reflection from the back of the material did not return in time.*

It is clear, as before, that the initial guess is crucial to the success of any optimization routine. To further demonstrate this importance, we expand our surface plot out

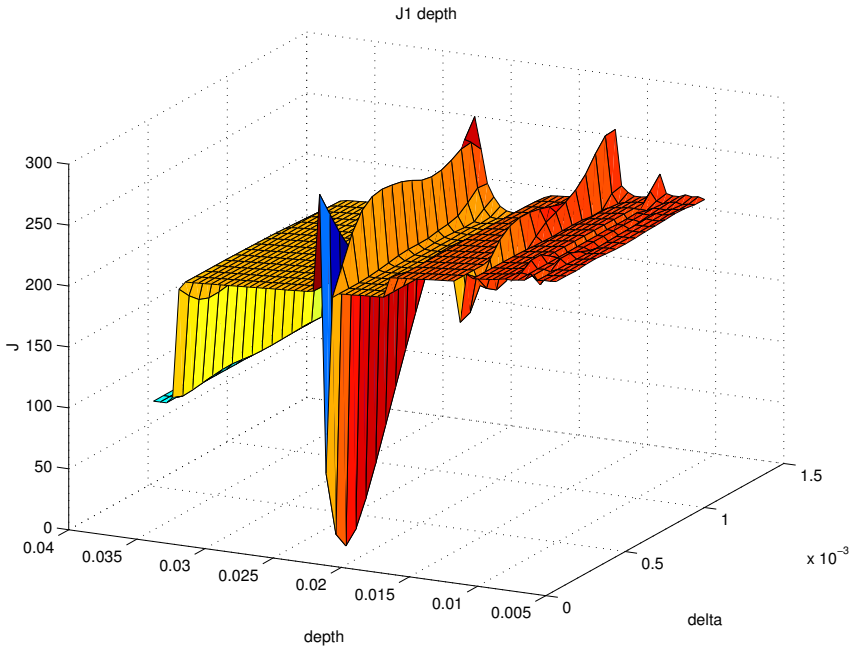

Figure 2.45: Surface plot of Least Squares objective function demonstrating peaks in J.

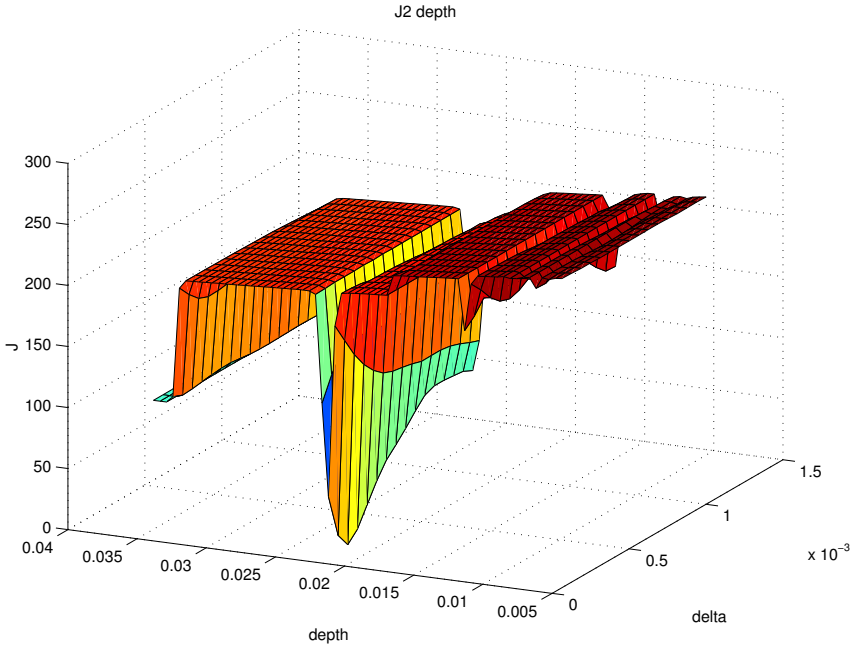

Figure 2.46: Surface plot of modified Least Squares objective function demonstrating lack of peaks in J.

in the δ direction, and zoom in with respect to d. Figures 2.47 and 2.48 depict J_1 and J_2 respectively. Notice that although J_2 does not exhibit the familiar peaks in J of J_1, it does however still have many local minima, which are as difficult, if not more so, to avoid in a minimization routine.

The local minima occur approximately every $\frac{\lambda}{4}$ along the line

$$d = -\frac{1}{\sqrt{\epsilon_\infty}}\delta + b.$$

This happens for the same reason as in Problem 1 (see Section 2.3.4). For an illustration, see Figures 2.49 and 2.50. In each figure we see that the small objective function value is due primarily to the coinciding of the single largest peak and/or the largest trough. (Note that the trailing oscillations are not numerical noise; the reflections appear as they do because $\delta \approx \frac{\lambda}{4} \approx 7.5 \times 10^{-4}$.)

Because we cannot eliminate these local minima, we must appeal to the procedure that worked in the previous problem, namely testing "check points". Since we know where these local minima are occurring with respect to the global minimum, if our minimization routine finds what it suspects to be a local minima, say (d_1, δ_1), we simply check $(d_1 \pm \alpha\frac{\lambda}{4}, \delta_1 \mp \alpha\sqrt{\epsilon_\infty}\frac{\lambda}{4})$, where $\alpha = 1/\sqrt{1+\epsilon_\infty}$. If we find a lower objective function value, we restart our optimization routine at that "check point".

2.4.2 Initial Guesses

In spite of our faith in the "check point" method, we still desire to find the best initial guesses for our optimization routine as possible so that we may hopefully find the global minimum without restarting. As before, we use the travel time of the first trough to approximate the location of the first interface. However, in this formulation we can take advantage of some of the characteristics of the signals. For example, the first reflection off of the gap is always trough-first, and the second (as well as each subsequent reflection) is always peak-first. For this reason, if we want to locate the first trough we can simply find the largest peak (belonging to the second reflection) and back track. It is a very simple matter to find a maximum or minimum of a vector of values. After the location of the largest peak is found, we back track to find the minimum in front of it, namely that belonging to the first reflection off of the gap. Then using the procedure described in Section 2.3.1, we approximate the root immediately in front of this trough. That gives us the travel time for

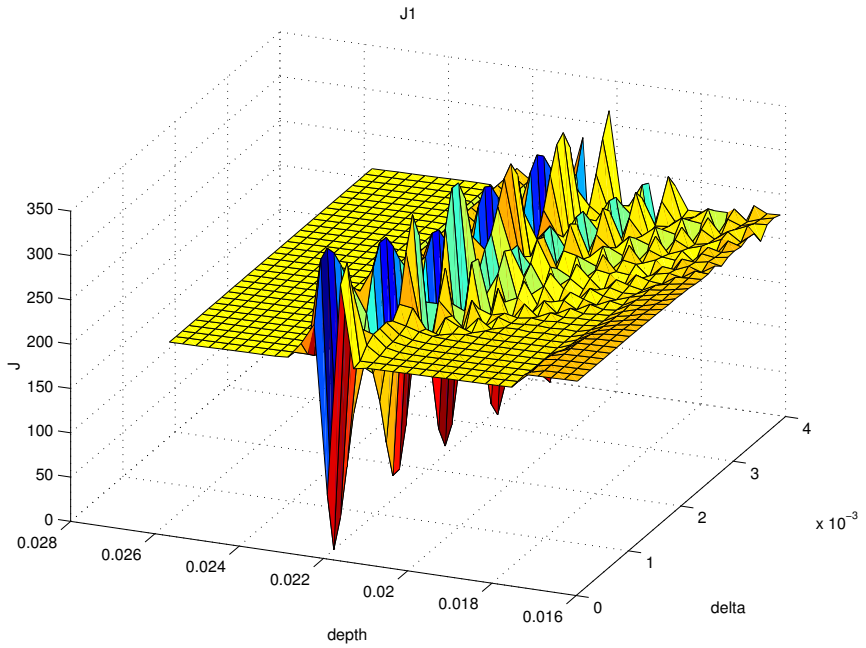

Figure 2.47: Close up surface plot of Least Squares objective function demonstrating peaks in J, and exhibiting many local minima.

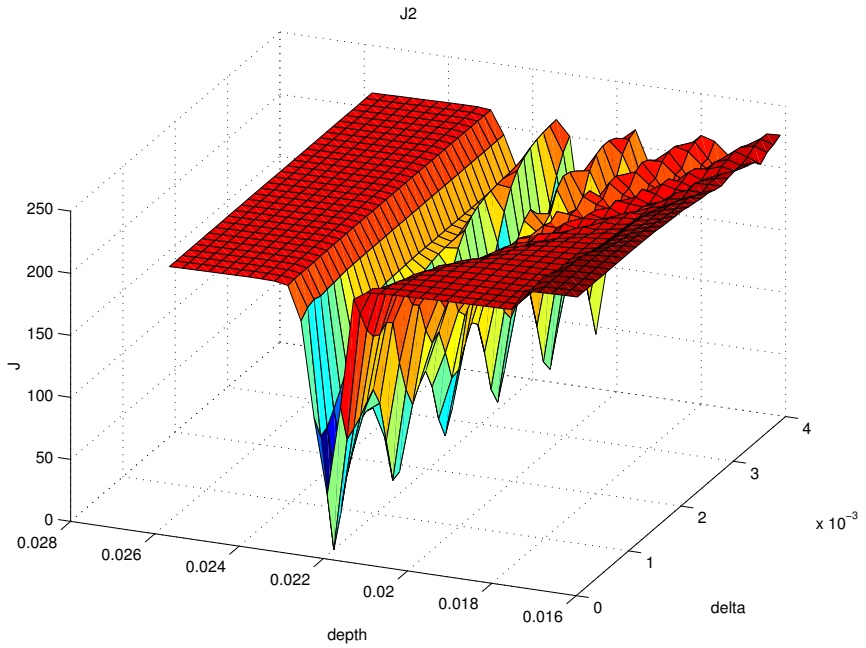

Figure 2.48: Close up surface plot of modified Least Squares objective function demonstrating lack of peaks in J, but exhibiting many local minima.

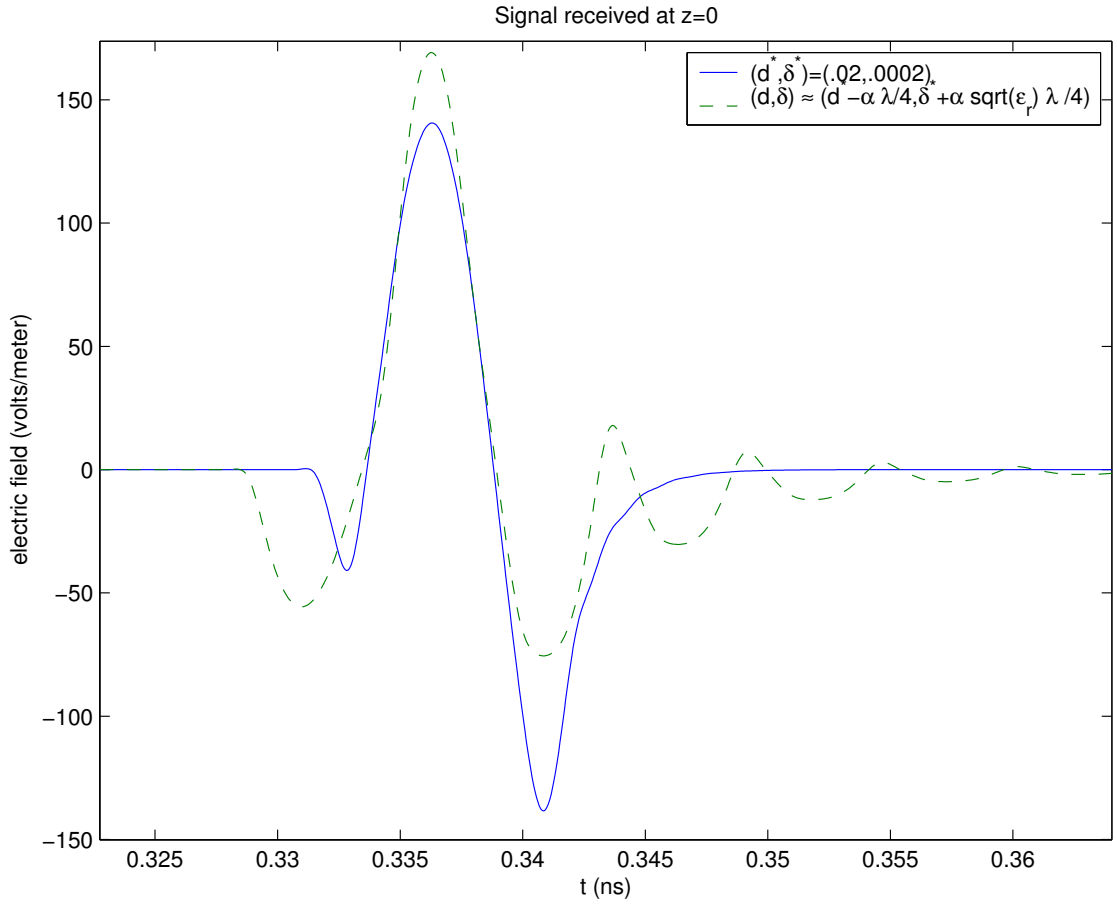

Figure 2.49: Data from (d^*, δ^*) and a simulation from the "check point" $(d^* - \alpha\frac{\lambda}{4}, \delta^* + \alpha\sqrt{\epsilon_r}\frac{\lambda}{4})$. The first trough cannot be matched, but δ is sufficiently large so that the signal's peak matches with that of the data.

the first reflection off of the gap, which in turn gives us the depth d of the gap.

Finding δ is, unfortunately, not nearly as straightforward. There are two main possibilities, and therefore, two differing approaches to approximating δ:

(i) The leading trough of the first reflection and the second reflection are disjoint (i.e., $\delta > \frac{\lambda}{8}$). In this case we can find the locations of the peak and trough and use the travel time between the two to approximate δ. We denote this approximation by δ_1. (Note that the observed peak is not necessarily the same as the original peak unless $\delta > \frac{3\lambda}{8}$, but it is still a good approximation). See Figure 2.51.

(ii) The second reflection partially truncates the trough of the first (i.e., $\delta < \frac{\lambda}{8}$). As a

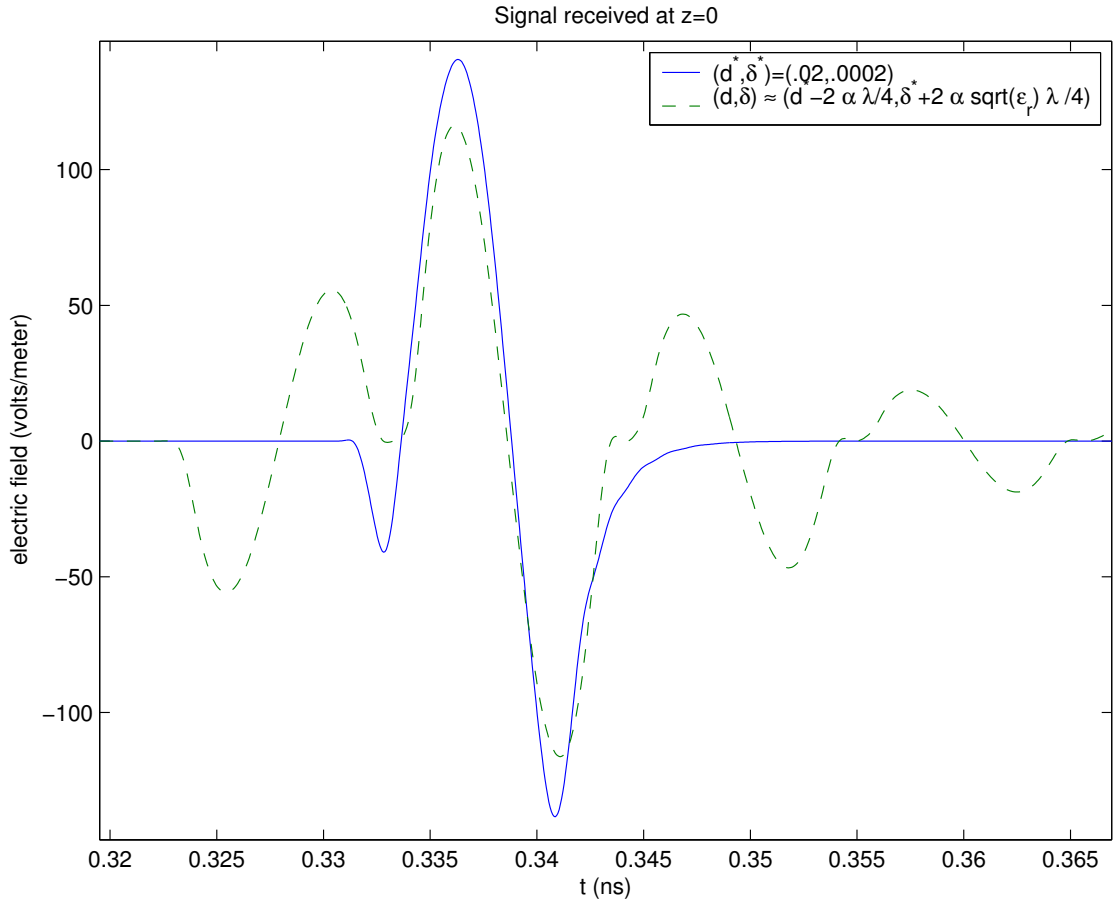

Figure 2.50: Data from (d^*, δ^*) and a simulation from the "check point" $(d^* - 2\alpha\frac{\lambda}{4}, \delta^* + 2\alpha\sqrt{\epsilon_r}\frac{\lambda}{4})$. Again, the first trough cannot be matched, but this time simulated signal has no cancelations so that its largest peak matches with that of the data.

rough approximation, we can assume that the location of the actual minimum (trough) is where the two signals begin to interfere with each other (the observable minimum). See Figure 2.52. We denote this approximation by δ_4.

A more accurate method is to use triangles to approximate the two reflections. By knowing the location of the maximum and minimum (peak and trough, respectively), and also the beginning of the first signal (from Section 2.3.1) and the rough approximation to the beginning of the second signal using δ_4, we can estimate the slopes of the two triangles with finite differences. Also note that since the two signals are added, the observed root between the peak and trough in the combined signal is actu-

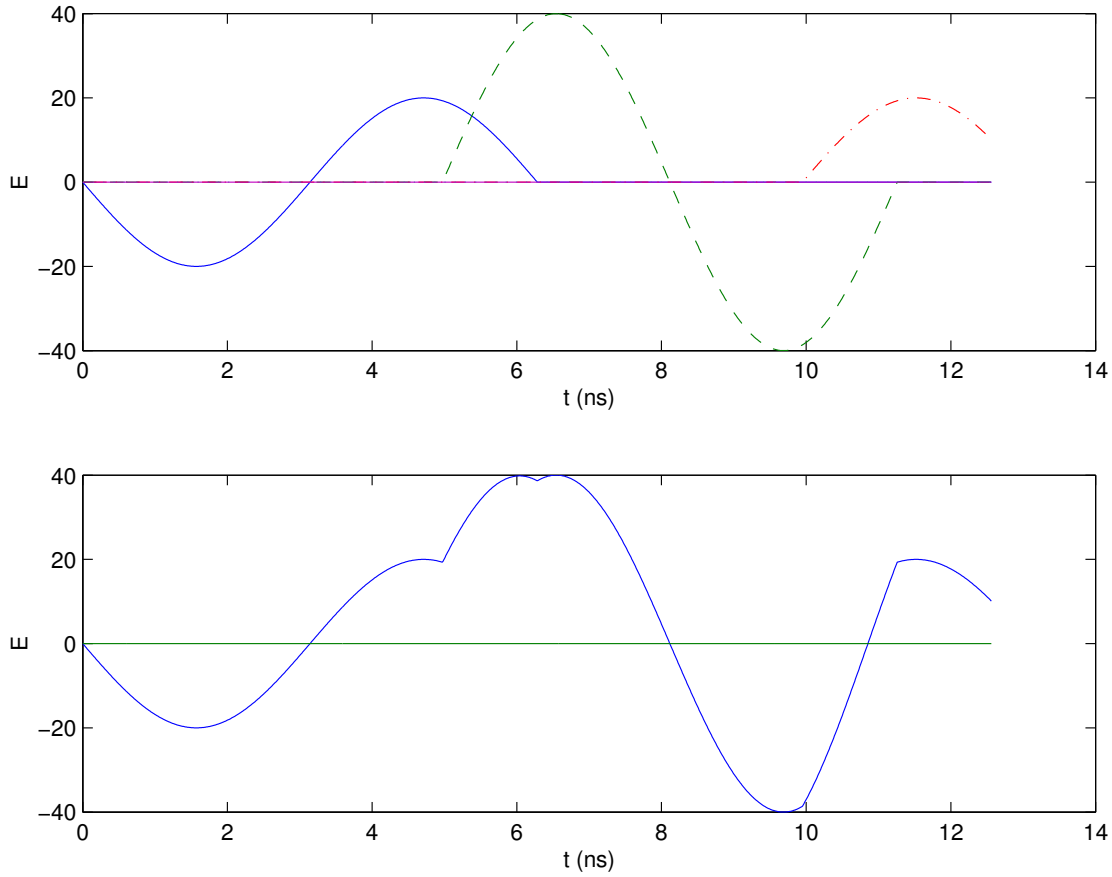

Figure 2.51: The top plot represents several signals which may be observed in a simulation of Problem 2. The bottom plot depicts the sum of the top signals. The peak of the second signal is just beginning to be obscured by the first when δ becomes less than $3\lambda/8$. Thus the observable maximum is still a good approximation of the peak of the second signal, and a trough to peak distance can be used to estimate δ.

ally an equilibrium point between the two signals. By setting equal to each other the two linear approximations for each of the two signals, evaluated at the equilibrium point, we can solve for the distance between the starting point of each signal, and thus for δ_3. See Figure 2.53. Specifically, let (p_1, q_1) be the location of the trough of the combined signal and (p_2, q_2) be the location of the peak. Let r_1 be the location of the root in front of the trough, and r_2 be the root between the trough and peak. Estimate the slope of the first signal, $m_1 < 0$, using (p_1, q_1) and r_1. Now if we let $y = r_2 - r_1$ and say x is the actual distance between r_1 and the beginning of the second signal, then setting the linear approximations equal in magnitude, but opposite in sign, at r_2

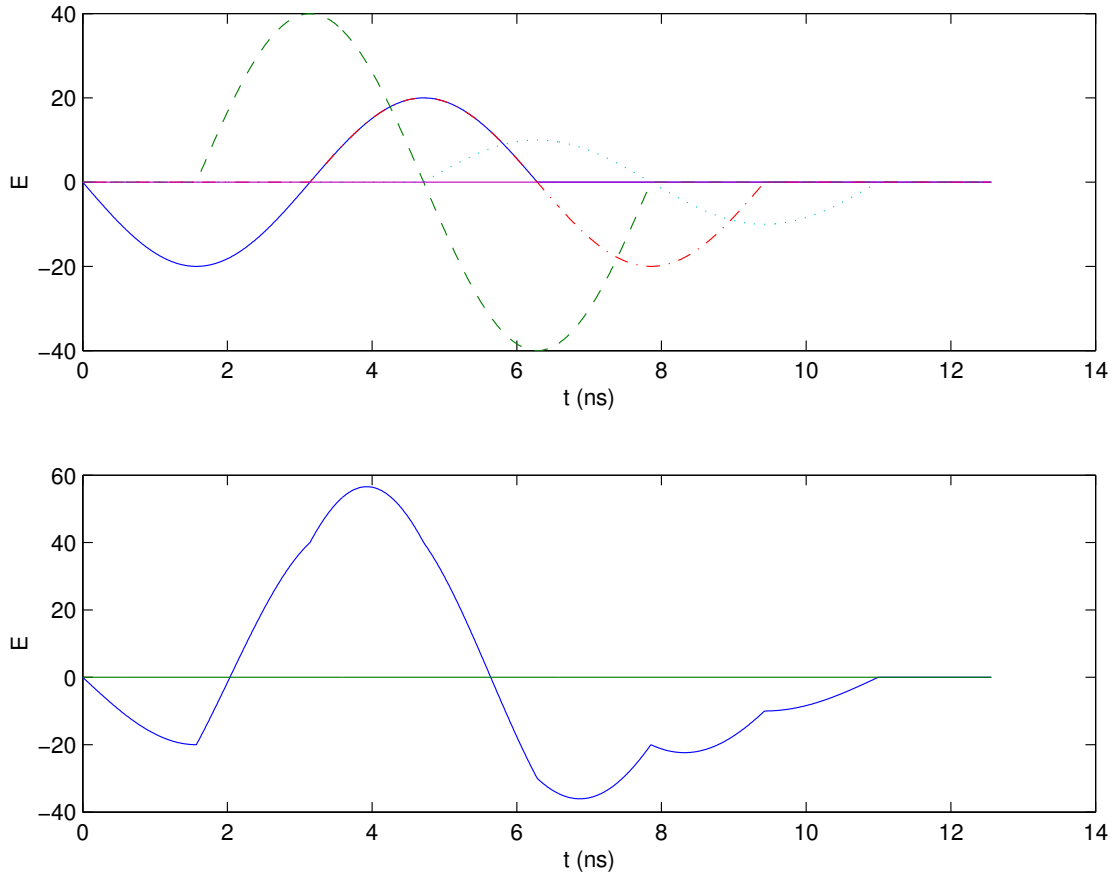

Figure 2.52: The top plot represents several signals which may be observed in a simulation of Problem 2. The bottom plot depicts the sum of the top signals. The trough of the first signal is partially truncated by the second signal. In this case the observed minimum is a still a good approximation to where the second signal begins. For smaller δ, a linear approximation must be used.

yields

$$-m_1 y = m_2(y - x).$$

Now we can estimate the slope of the second signal, $m_2 > 0$, using (p_2, q_2) and $(r_2, -m_1 y)$. Also, we can re-write the above equation as

$$x = \left(\frac{-m_1 + m_2}{m_2}\right) y.$$

To find δ_3 we simply divide x by 2 and the (scaled) speed of light in the material, i.e., $\sqrt{\epsilon_\infty}$.

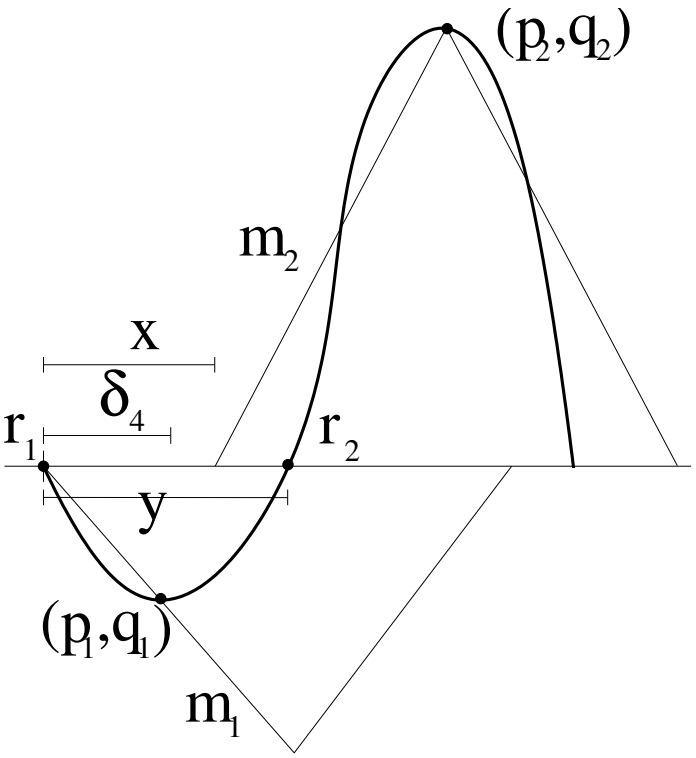

Figure 2.53: This schematic depicts the roots, extrema, distances, and slopes used in the computation of δ_3.

Since each of the two situations above is dependent on the parameter it is approximating, we must also determine which of the above methods is most appropriate to use. Thus we use the most precise of the available methods to determine the situation, i.e., δ_4, instead of δ_3 since in general δ_3 underestimates δ so we do not want to use it as a criterion for determining whether δ is small. (Note that when δ is indeed small, δ_3 is more accurate than δ_4.) The estimate for δ_4 tends to be an overestimate, and is only valid if $\delta < \frac{\lambda}{8}$. Unfortunately, δ_1 also tends to be an overestimate, so we prefer to only trust it entirely if it is larger than $\frac{\lambda}{4}$. If neither δ_1 nor δ_3 is a sufficient approximation we choose to use the average of the two, and call it δ_2.

Therefore our algorithm for approximating δ is as follows:

(a) If $\delta_4 < \frac{\lambda}{8}$ then use δ_3

(b) else if $\delta_1 > \frac{\lambda}{4}$ then use δ_1

(c) else use δ_2 (average between δ_1 and δ_3).

We tested our approximating methods on exact depth (d) values of: .02, .04, .08, .1, and .2 m, and values of width (δ): .0001, .0002, .0004, .0006, and .0008 m. Since $\frac{\lambda}{8}$ is the transition point between the two situations, it is understandable why δ close to this value is the most difficult to accurately resolve. We chose this range of δ's because our choice of frequency gives $\frac{\lambda}{8} = 3.7475 \times 10^{-4} m$. See Tables 2.3 and 2.4 for the initial estimates of d and δ respectively.

The approximations improve slightly as the number of finite elements is increased, and seemed to converge to fixed values. This suggests that numerical error (and instability) can affect the estimates. For each case there is a significant amount of numerical error in the simulations below a certain number of elements, therefore in approximating δ we chose to use the number of elements just above the threshold. The number of finite elements (N) used in the simulations is given for each case. Since approximating d does not depend on δ, we show the progression of estimates as N increases. The values in Table 2.3 which are bold denote the values used to approximate δ in Table 2.4.

Table 2.3: The initial estimates of d. The values in bold denote the values used to approximate δ in Table 2.4.

	N				
d	1024	2048	4096	8192	16384
.02	**0.0200036**	0.019996	0.0199998	0.0199998	
.04	0.0399689	**0.0399766**	0.0399919	0.0399958	
.08	0.0799225	0.0799609	**0.0799839**	0.0799992	
.1				**0.0999799**	
.2					**0.200006**

Table 2.4: The initial estimates of δ.

		δ				
d	N	.0001	.0002	.0004	.0006	.0008
.02	1024	9.41856e-05	0.000127645	0.000611592	0.000683544	0.000791472
.04	2048	0.000113806	0.000210178	0.000611592	0.000647568	0.000791472
.08	4096	2.89938e-05	0.00019437	0.000575616	0.000647568	0.000755496
.1	8192	0.000151182	0.000239409	0.000593604	0.000647568	0.000791472
.2	16384	8.74169e-05	0.000146323	0.000575616	0.000647568	0.000791472

These initial estimates may seem relatively inaccurate, some δ approximations being almost 100% off from the actual value, but in these tests all were sufficiently close

to the global minima to converge, while not resulting in a false, local minima. While our "check point" method is available if needed, it is much more efficient to have an accurate initial estimate than to restart after optimizing from a bad one. Figures 2.54 through 2.58 display surface plots of the modified Least Squares objective function zoomed in around the region that our initial estimates are located. It is evident that relatively small errors in

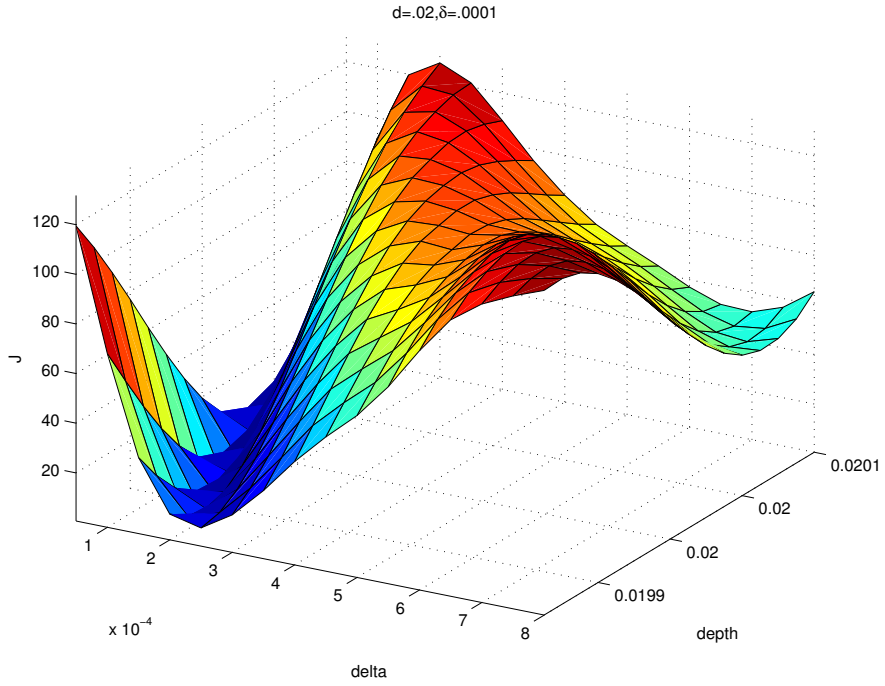

Figure 2.54: Very close surface plot of the modified Least Squares objective function using $d = .02$ and $\delta = .0001$.

the initial estimates could prevent an optimization routine from finding the global minima. For example, in Figure 2.54 if the initial estimate for d were 1×10^{-4} too high and δ too high by 2×10^{-4} then the gradient would cause both δ and d to increase, thus leading to the wrong minima. In cases such as these, the "check point" method provides a last resort.

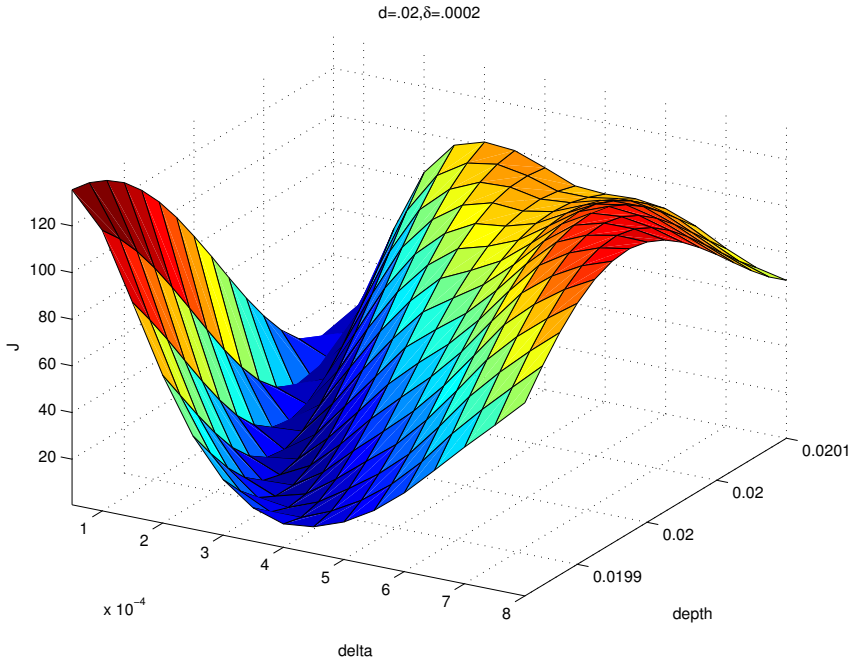

Figure 2.55: Very close surface plot of the modified Least Squares objective function using $d = .02$ and $\delta = .0002$.

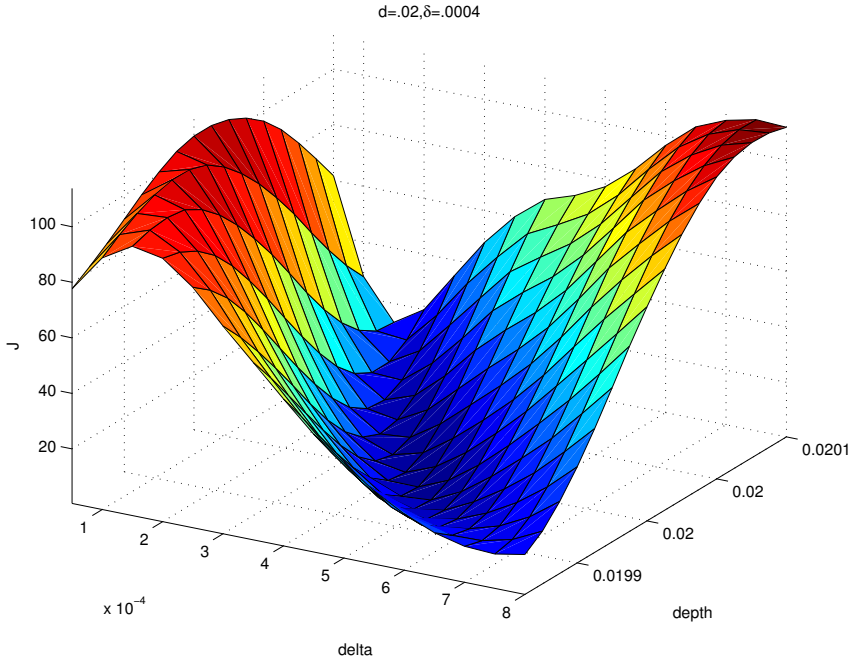

Figure 2.56: Very close surface plot of the modified Least Squares objective function using $d = .02$ and $\delta = .0004$.

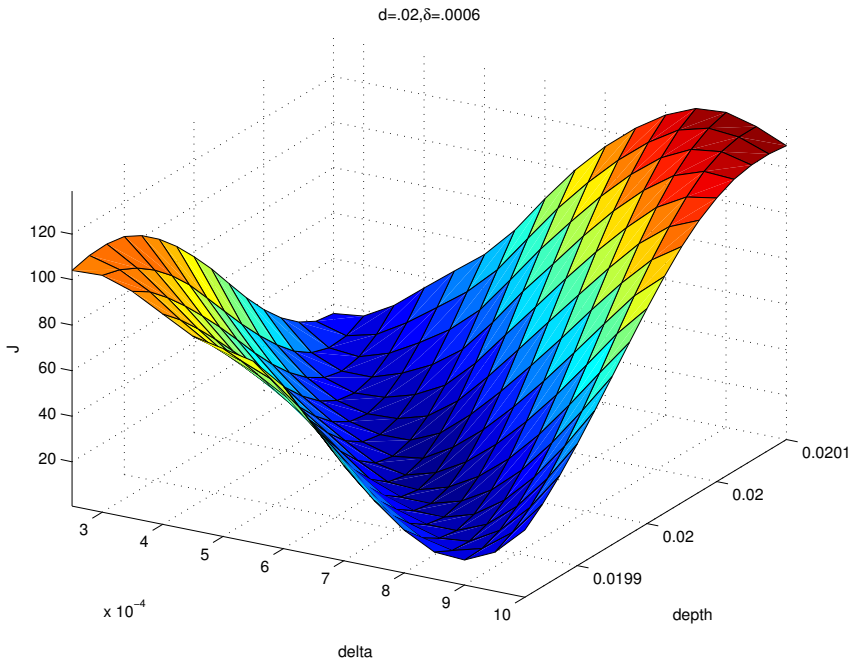

Figure 2.57: Very close surface plot of the modified Least Squares objective function using $d = .02$ and $\delta = .0006$. (Note that the axis is shifted from the previous Figures in order to include the minimum.)

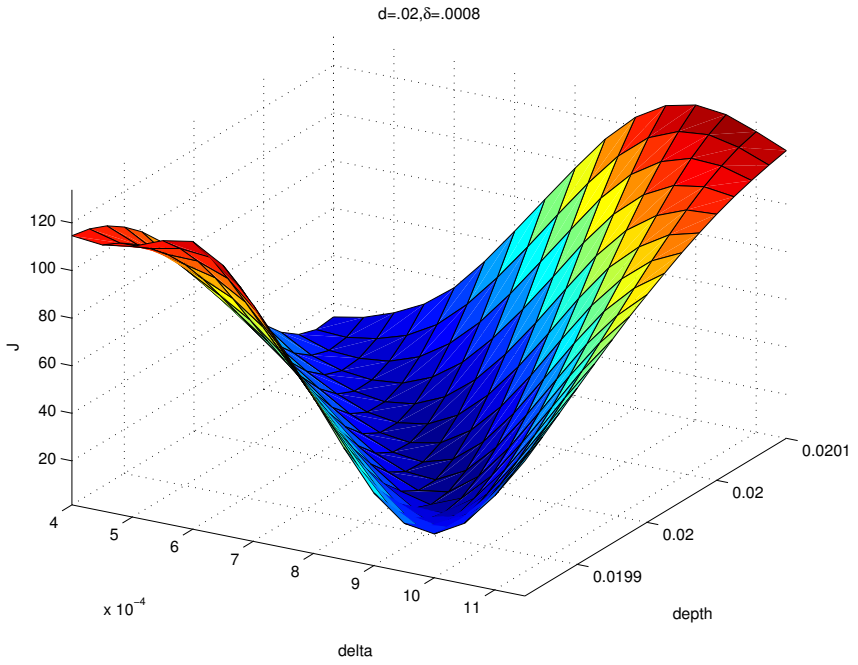

Figure 2.58: Very close surface plot of the modified Least Squares objective function using $d = .02$ and $\delta = .0008$. (Note that the axis is shifted from the previous Figures in order to include the minimum.)

2.4.3 Optimization Method

Now that we have approximated our initial guesses, we need to minimize the objective function in order to solve the inverse problem. In Problem 1, Gauss-Newton was sufficient to find the global minimum for most cases. In this formulation, however, we will apply more sophisticated methods, reverting to Gauss-Newton whenever possible since its convergence rate is best.

The first modification we make to Gauss-Newton is to add a Levenberg-Marquardt parameter, ν_c (see [K99]). The Inexact Newton step becomes

$$s_c = -\left(R'(q_c)^T R'(q_c) + \nu_c I\right)^{-1} R'(q_c)^T R(q_c).$$

This parameter adds regularization by making the model Hessian positive definite. The method uses a quadratic model Hessian, and also has a built-in line search incorporating a sufficient decrease condition. The line search is based on the predicted decrease computed from the quadratic model. If the actual improvement of the objective function, J, is close to the amount predicted by the model Hessian after a step is taken, then the method decreases the Levenberg-Marquardt parameter, ν_c, effectively increasing the relative size of the next step, which hopefully accelerates the convergence. As ν_c is decreased to 0 the method becomes Damped Gauss-Newton (meaning Gauss-Newton with a line search). If, however, the actual improvement of J after a step is not sufficient (or is even negative), ν_c is increased, effectively scaling back the Newton step, and we retest. If there are too many reductions then we declare a "line search failure" meaning that too small a step is required to decrease the objective function.

Usually a method would exit after a line search failure, returning the best approximation so far. But we use this failure to call an adaptive mesh size routine, i.e., an Implicit Filtering technique. The idea is that the failure is likely due to the fact that the direction the finite difference gradient chose is probably not an actual "descent direction" in the global sense. In other words, the finite differencing is most likely differentiating noise. In the same manner that a seemingly smooth surface may look rough under a microscope, using too small of a differencing step amplifies effects from round-off error and other sources of numerical noise. Our technique is to increase the relative differencing step, $\hat{h}$, recompute the gradients, and then try the Levenberg-Marquardt method again. The relative differencing

step, $\hat{h}$, is such that the gradient, $\nabla_{\hat{h}}$, of $J(q) = J([d, \delta])$ is computed with

$$\nabla_{\hat{h}} J([d,\delta]) = \begin{bmatrix} \frac{J\left((1+\hat{h})d,\delta\right) - J(d,\delta)}{\hat{h}d} \\ \\ \frac{J\left(d,(1+\hat{h})\delta\right) - J(d,\delta)}{\hat{h}\delta} \end{bmatrix}$$

We apply a similar approach to modifying the differencing step $\hat{h}$ as we do for changing ν_c in that after a successful step we decrease $\hat{h}$, but if we have another failure we increase $\hat{h}$ even more. Since the convergence rates of gradient based methods are dependent on the size of $\hat{h}$ (for example Gauss-Newton is $O(\hat{h}^2)$), we want $\hat{h}$ to be as small as possible and still be effective, similarly with ν_c. We use a three tiered approach to changing $\hat{h}$. Initially we set $\hat{h} = 10^{-9}$. To increase $\hat{h}$ we raise it to the $\frac{2}{3}$ power, to decrease we raise it to the $\frac{3}{2}$ power. Additionally we define 10^{-4} to be the maximum allowable differencing step value. Thus $\hat{h} \in \{10^{-9}, 10^{-6}, 10^{-4}\}$.

In general an optimization method exits with "success" if the norm of the current gradient is less than *tol* times the norm of the initial gradient. However, in our method we do not immediately trust the finite difference gradients, and instead call Implicit Filtering when the gradients appear small. When we have verified small gradients on all three scales (the various values of the differencing step $\hat{h}$ defined above), then we exit with "success". Likewise, if we experience line search failures on all three scales, we exit with "failure" and return the best minimizer so far.

Remark 4 *In practice, a very good solution is found within a couple of Levenberg-Marquardt steps, and then an equal number of Implicit Filtering iterations verify, and sometimes enhance, this solution. In the interest of efficiency, and since this is a parameter identification problem, we exit early with "success" if our objective function is satisfactorily small (i.e., less than* **tol** *times the initial value), thus saving at least half of the possible iterations.*

Additionally we impose a restriction on the number of "pullbacks" on each linesearch, and on the number of linesearches, effectively limiting the total number of iterations. If a small gradient has not been verified before exhausting the maximum number of iterations, we exit with "failure" and again return the best minimizer so far.

2.4.4 Numerical Issues

For small N the difficult cases are those with large depth. This is because, as we mentioned before, the computational domain is effectively increased when the depth is increased, making the mesh sizes larger and increasing the level of numerical error. The magnitude of δ does not seem to have a significant effect on the convergence of the method.

An obvious disadvantage to having a large N is that each simulation takes much longer. Although on average fewer function calls are required with the larger N cases to obtain the same level of accuracy, in general the total execution time is quadrupled when the number of elements is doubled. This is consistent with the fact that complexity of the most time consuming part of the simulation, the linear solves, is $O(N)$, and the number of time steps N_t is also $O(N)$. So when we double the number of finite elements we are also doubling the number of time steps. Therefore, we obtain an overall complexity of $O(N^2)$. Thus, as mentioned before, in our inverse problem we choose to use the number of elements just above the threshold of when numerical error is apparent.

We should also mention that in order to create data, in lieu of actual experimental data, we perform a simulation at a higher resolution believing it to be more accurate. Specifically, we double the number of finite elements. Since the time step, and therefore the effective sample rate if the time step is too large, are both dependent upon the mesh size (recall $\Delta t = O(h)$ and Remark 2), the sample times of the simulated data do not necessarily correspond with the sample times of the simulations at the lower resolution. (In general we have twice as many samples from the higher resolution.) Thus in order to compute the modified least squares error between the two vectors, we perform a linear interpolation of the simulated data onto the sample times at the lower resolution. See Figure 2.59. Note that in the usual case where we simply have twice as many sample points from the higher resolution simulation, we are in effect discarding sample points rather than doing a true interpolation.

For comparison we compute the low resolution simulation using the values d^* and δ^* (note that this is not the same as taking the high resolution simulation and interpolating it onto the low resolution time steps, which we actually use as our observed data). In every case that we have tested, J, when computed with the d and δ values found from the optimization routine (d_{min} and δ_{min}), is less than or equal to J when computed with the original values (d^* and δ^*). This suggests that an actual global minimum of the objective

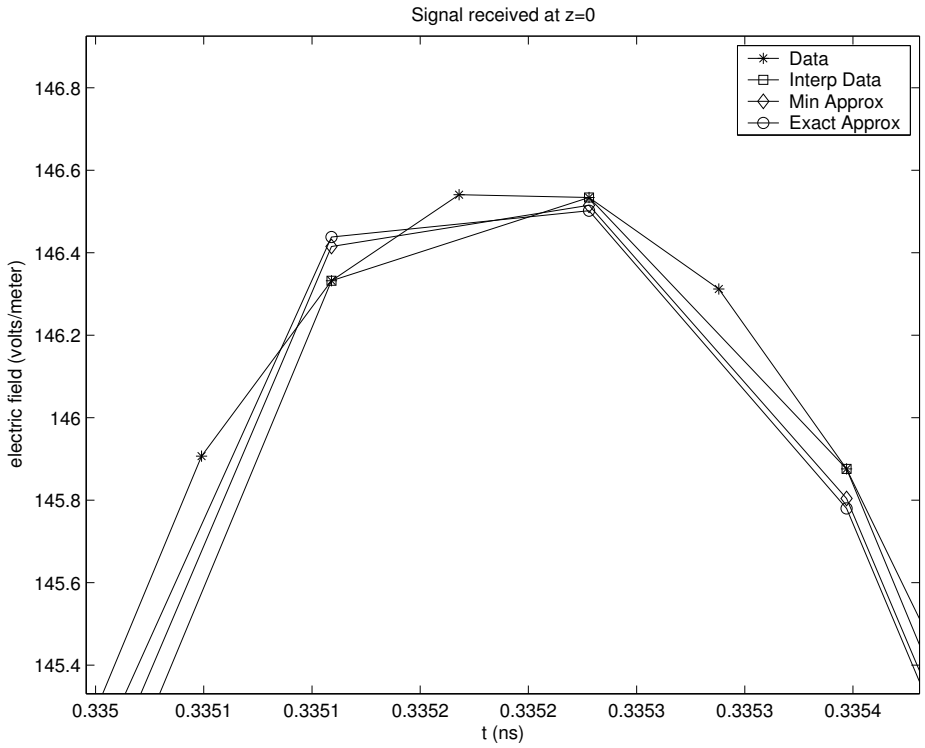

Figure 2.59: Plotted are the actual simulated data ($N = 2048$), the interpolation of the simulated data onto the low resolution sample times ($N = 1024$), the result of the minimization routine ($N = 1024$), and a low resolution ($N = 1024$) simulation using the exact values of d and δ.

function has been found, even though the final estimates of d and δ themselves are not necessarily equal to d^* and δ^*. Note in Figure 2.59 that the simulation using original values, (d^*, δ^*), is in fact closer to the original data, but the simulation using the minimizer values, (d_{min}, δ_{min}), is closer to the interpolated data (see for example the $[.335, .3352]$ interval).

Although we could compute our optimization routine at the same resolution as the simulated data to obtain a better fit in our tests, this would not properly represent the real-life phenomenon of sampling data. Sampled data is inherently not a completely accurate representation of a physical observation. We believe that our interpolation approach gives a more realistic expectation of how our method would perform given actual experimental data. In order to further test the robustness of our inverse problem solution method we introduce random noise to the detected data in Section 2.4.5.

2.4.5 Numerical Results

Tables 2.5 and 2.6 display the final computed approximations for the depth of the slab (d_{min}) and the width of the gap behind it (δ_{min}). The relative differences from the original values used to generate the data (d^* and δ^*), are: for depth, on the order of .0001 and for δ, on the order of .01. However, this does not imply that the optimization routine was unable to find the optimal solution. Recall that since our data is generated with essentially a different simulator than our forward solves, the original values do not necessarily minimize the objective function. The objective function values give a better indicator of how well the optimization routine works since it shows the fit to the generated data. Table 2.7 displays the final objective function values. In each of these cases, the final objective function value (J_{min}) was less than $J^* := J(q^*)$. In fact, the ratios $J_r := J_{min}/J^*$ were on average .3008. We consider any $J_r < 1$ to represent a successful convergence.

Although δ values that are near $\frac{\lambda}{8} = 3.7475 \times 10^{-4}m$ are the most difficult for which to obtain initial approximations, we see that the objective function values in these cases are just as small (and the final estimates are just as close) as for other δ values.

The execution time, in seconds, is given in Table 2.8. While the previous tables verify that we were actually able to resolve the case of $20cm$ depth, we see here what price we had to pay. The average execution times for each of different mesh sizes ($N = 1024, 2048, 4096, 8192,$ and 16384) were $39, 248, 1452, 6229,$ and 35509 seconds, respectively. Each represents and increase in time over the previous mesh size by a factor of $6.4, 5.9, 4.28,$ and 5.7, respectively. This is consistent with the fact that the forward solves are order $O(h^2)$. However, the additional sample points for the larger N cases allowed for smaller objective function values which took increasingly more iterations to satisfy the relative tolerance in our stopping criteria. This explains why we do not see ratios closer to the expected 4 for order $O(h^2)$ methods. The number of calls to the simulator (related to the number of Levenberg-Marquardt iterations) for each case is given in Table 2.9.

2.4.6 Relative Random Noise

We add random noise to the signal, as mentioned above, in order to more closely simulate the experimental process in data collection. As in Section 2.3.8, we start with relative noise where the absolute value of the noise is proportional to the size of the signal. If

Table 2.5: The final estimates of d.

		δ				
d	N	.0001	.0002	.0004	.0006	.0008
.02	1024	0.0200053	0.0200022	0.0200006	0.0200005	0.0200002
.04	2048	0.0399948	0.0399974	0.0400005	0.0400005	0.0399999
.08	4096	0.0799973	0.0799987	0.0800006	0.0800006	0.0800003
.1	8192	0.0999945	0.0999974	0.1	0.1	0.0999999
.2	16384	0.200011	0.200005	0.2	0.2	0.200001

Table 2.6: The final estimates of δ.

		δ				
d	N	.0001	.0002	.0004	.0006	.0008
.02	1024	9.40622e-05	0.000196754	0.000398642	0.000597275	0.00079707
.04	2048	0.000106435	0.000203916	0.000394204	0.000592156	0.000793622
.08	4096	0.000103585	0.000202273	0.000395791	0.000593861	0.000794401
.1	8192	0.000106593	0.000203876	0.000396203	0.000594976	0.000795985
.2	16384	8.7456e-05	0.000191808	0.00040297	0.000602902	0.00080129

Table 2.7: The objective function value of the final estimates.

		δ				
d	N	.0001	.0002	.0004	.0006	.0008
.02	1024	0.00786171	0.00906699	0.0115657	0.0233783	0.0447687
.04	2048	0.021516	0.0343314	0.0514108	0.0700747	0.0927117
.08	4096	0.0116105	0.0145428	0.0201004	0.0272513	0.0344458
.1	8192	0.00304723	0.00547532	0.00779186	0.00931778	0.0118529
.2	16384	0.000609258	0.00133978	0.00146975	0.000962975	0.000766141

E_i is the data sampled, then we define $\hat{E}_i = E_i(1+\nu_r\eta_i)$, where η_i are independent normally distributed random variables with mean zero and variance one. Again, the coefficient ν_r determines the relative magnitude of the noise as a percentage of the magnitude of E_i, in particular, $\nu_r = 0.01$ corresponds to 2% noise. We tested relative magnitude levels of 2%, 10%, and 20% (corresponding to $\nu_r = .01, .05,$ and $.1$ respectively). Table 2.10 displays the initial estimates of d for $\nu_r = .1$ (other ν_r values produced very similar results, so we only give the worst case here). Tables 2.11 through 2.13 display the initial estimates of δ for

Table 2.8: The execution time in seconds to find the final estimates.

		δ				
d	N	.0001	.0002	.0004	.0006	.0008
.02	1024	39	35	48	38	35
.04	2048	198	197	319	196	328
.08	4096	1560	1458	1500	1071	1671
.1	8192	6141	5256	7625	5319	6802
.2	16384	31818	42755	35860	26521	40593

Table 2.9: The total number of calls to the simulator required to find the final estimates.

		δ				
d	N	.0001	.0002	.0004	.0006	.0008
.02	1024	23	23	33	26	23
.04	2048	24	24	43	24	45
.08	4096	38	35	36	24	41
.1	8192	29	24	37	24	33
.2	16384	36	50	41	29	48

several different noise levels. There is not a noticeable significant change in the accuracy of the estimates even for $\nu_r = .1$. In nearly all the cases the estimate was close enough for the optimization method to converge ($J_r < 1$) to the expected minimum. The only exceptions were with $\nu = .1$ and $\delta = .0004$, which are understandably the most difficult cases.

The final approximations d_{min} and δ_{min} in the presence of noise are given in Tables 2.14 through 2.19. Some approximations with high noise may appear to be better approximations than some with little or no noise. For example, with $\delta^* = .0001, d^* = .04$, the $\nu_r = .1$ approximations are an order of magnitude closer to the original values than the $\nu_r = 0$ approximations. This is not to say that the noise helps the approximation method. Rather, it is for the same reason that, for example, as shown in Figure 2.59, the actual parameter values produced a signal farther away (in the Least Squares sense) from the generated data than a signal computed with the approximated parameter values. The resulting objective function values give a better indication of the accuracy of the approximation to the data. A comparison of Tables 2.7 and 2.20 clearly show that the data without noise is more accurately matched by its approximations than those with noise.

Table 2.10: The initial estimates of d with $\nu_r = .1$. The values in bold denote the values used to approximate δ in Table 2.13. (Initial estimates of d using other ν_r values were very similar and therefore are omitted.)

	N		
d	1024	2048	4096
.02	**0.020019**	0.0199883	0.0199998
.04	0.0399689	**0.0399766**	0.0399919
.08	0.0799225	0.0800069	**0.0799992**

Table 2.11: The initial estimates of δ with $\nu_r = .01$.

		δ				
d	N	.0001	.0002	.0004	.0006	.0008
.02	1024	9.43492e-05	0.000127736	0.000611592	0.000647568	0.000791472
.04	2048	0.000115174	0.000209026	0.000611592	0.000647568	0.000755496
.08	4096	3.20852e-05	0.000194313	0.000611592	0.000647568	0.000827448

Table 2.12: The initial estimates of δ with $\nu_r = .05$.

		δ				
d	N	.0001	.0002	.0004	.0006	.0008
.02	1024	4.34312e-05	0.000129248	0.000575616	0.000575616	0.000755496
.04	2048	0.000115175	0.000211701	0.000611592	0.000755496	0.000755496
.08	4096	1.76356e-05	0.000194415	0.000647568	0.000647568	0.000683544

Table 2.13: The initial estimates of δ with $\nu_r = .1$.

		δ				
d	N	.0001	.0002	.0004	.0006	.0008
.02	1024	0.000107928	0.000172127	0.000575616	0.000323784	0.000611592
.04	2048	9.99018e-05	0.000216157	0.000575616	0.000611592	0.000647568
.08	4096	4.76434e-05	0.000194762	0.000611592	0.000647568	0.000755496

Table 2.14: The final estimates of d using $\nu_r = .01$.

		δ				
d	N	.0001	.0002	.0004	.0006	.0008
.02	1024	0.0200057	0.0200021	0.0200006	0.0200008	0.0200001
.04	2048	0.0399944	0.0399971	0.0400005	0.0400005	0.0399998
.08	4096	0.079997	0.0799986	0.0800004	0.0800005	0.0800003

Table 2.15: The final estimates of d using $\nu_r = .05$.

		δ				
d	N	.0001	.0002	.0004	.0006	.0008
.02	1024	0.0200061	0.0200009	0.0200016	0.0200013	0.0200002
.04	2048	0.0399951	0.0399982	0.0399993	0.0400006	0.0399997
.08	4096	0.0799957	0.0799971	0.0799999	0.0800004	0.0800001

Table 2.16: The final estimates of d using $\nu_r = .1$.

		δ				
d	N	.0001	.0002	.0004	.0006	.0008
.02	1024	0.0200059	0.020006	0.0200017	0.0199998	0.0199974
.04	2048	0.0399993	0.0399976	0.0399991	0.0400021	0.0399982
.08	4096	0.0799982	0.079997	0.0800002	0.0799986	0.0800013

Table 2.17: The final estimates of δ using $\nu_r = .01$.

		δ				
d	N	.0001	.0002	.0004	.0006	.0008
.02	1024	9.34307e-05	0.000196985	0.000398454	0.000596308	0.000797028
.04	2048	0.000106823	0.000204701	0.000394249	0.0005922	0.000793984
.08	4096	0.000103996	0.000202579	0.000396222	0.000593539	0.000794799

Table 2.18: The final estimates of δ using $\nu_r = .05$.

		δ				
d	N	.0001	.0002	.0004	.0006	.0008
.02	1024	9.40065e-05	0.000198868	0.000396695	0.000597252	0.000794729
.04	2048	0.000105547	0.000203208	0.000400938	0.000592641	0.000791008
.08	4096	0.000105656	0.000203992	0.000396485	0.000594405	0.000793268

Table 2.19: The final estimates of δ using $\nu_r = .1$.

		δ				
d	N	.0001	.0002	.0004	.0006	.0008
.02	1024	9.34486e-05	0.000188052	0.000392001	0.000594642	0.00079958
.04	2048	0.000100242	0.000204073	0.000401208	0.000586155	0.000798636
.08	4096	0.000101771	0.000205295	0.000400441	0.000604353	0.000798047

Table 2.20: The objective function value of the final estimates using $\nu_r = .1$.

		δ				
d	N	.0001	.0002	.0004	.0006	.0008
.02	1024	3.89043	4.0585	1.64814	3.46279	4.1071
.04	2048	1.29514	1.42229	1.47275	1.5261	1.61906
.08	4096	0.779184	0.717672	0.848017	0.647817	0.674641

2.4.7 Standard Error Analysis

In an actual inverse problem using data collected by experiment, one desires to have confidence intervals on all parameter estimates. We will apply standard error techniques to an Ordinary Least Squares (OLS) formulation of our problem to obtain confidence intervals on our estimates. In order to rewrite our objective function in an OLS formulation, we define $y(t;q) = |E(t,0;q)|$ to be our estimate to $\hat{y} = |\hat{E}|$, which is the data we are trying to fit by determining $q = (d, \delta)$. Now it is clear that our objective function can be written in the standard OLS form

$$J(q) = \frac{1}{N_s} \sum_{i=1}^{N_s} |y(t_i;q) - \hat{y}_i|^2 .$$

For simplicity of terminology, in this section alone, we will refer to $|\hat{E}_i|$ as the data and to $|E(t_i,0;q)|$ as the simulations.

With the relative random noise described above we do not have constant variance, as is demonstrated in Figures 2.60 and 2.61. Here we have plotted the residual $r_i := |E(t_i,0;\hat{q}_{OLS})| - |\hat{E}_i|$ against time, t_i, and also against $|E(t_i,0;\hat{q}_{OLS})|$. As one would expect with noise that is relative in size to the signal value, we have a pattern in Figure 2.60 that follows the pattern of the original signal. Figure 2.61 demonstrates the fan shape associated with noise that is dependent upon the size of the signal, i.e., non constant variance.

Since constant variance is most conveniently assumed in standard error analysis, we further consider estimates obtained from an inverse problem applied to data with constant variance random noise added. In particular, the data we now consider is generated by

$$\hat{E}_j = E(t_j, 0, ; q^*) + \beta \nu_r \eta_j$$

where

$$\eta_j \sim \mathcal{N}(0,1)$$

and the constant β is a scaling factor chosen simply so that the noise level, ν_r, will somewhat correspond to the parameter ν_r used in the previous section on relative noise. Specifically, $\beta = \max_i \hat{E}_i/10$ ensures that J^* in the constant variance cases is on the same order of magnitude as those in the relative noise cases above for all choices of d and δ that we have considered.

The variance of this data is

$$\sigma^2 = \mathcal{E}x[\beta^2 \nu_r^2 \eta_j^2] = \beta^2 \nu_r^2 \mathcal{E}x[\eta_j^2] = \beta^2 \nu_r^2$$

where $\mathcal{E}x$ denotes the expectation. Therefore, we do have constant variance. Note further the resulting lack of patterns in Figures 2.62 and 2.63. The suspicious looking phenomenon of many points on the line $E = 0$ is simply because in the original data E is very close to zero most of the time. (Recall Figures 2.49 and 2.50 for example.) Figure 2.64 demonstrates graphically the difference between relative noise and constant variance noise. The relative noise case is particularly difficult in our inverse problem since most of our initial estimates are based on accurately determining the peak locations, yet this is exactly where most of the relative noise is concentrated.

With constant variance, and further, assuming that each η_j is identically independently (normally) distributed, we have that (see [DG95]) in the limit as $N_s \to \infty$

$$\hat{q}_{OLS} \sim \mathcal{N}_2 \left(q_0, \sigma_0^2 \left[\mathcal{E}^T(q_0)\mathcal{E}(q_0) \right]^{-1} \right).$$

Here $\mathcal{E}(\hat{q}) = \frac{\partial |E|}{\partial q}(\hat{q})$ which is an $N_s \times 2$ matrix since $q = (d, \delta)$ and $|E|$ is evaluated at N_s sample times. Also, the scale parameter σ_0^2 is approximately given by

$$\sigma_0^2 = \frac{1}{N_s - 2} \sum_{i=1}^{N_s} \left(|E(t_i, 0; q_0)| - |\hat{E}_i| \right)^2.$$

In the above equations, q_0 denotes the theoretical "true" value of the parameter that best describes the system from which the data is taken. Note that in this case, this is not necessarily the same as q^* since the method used to generate the data is different from the forward solve simulator. Therefore q_0 is generally unknown even in examples with simulated data.

As demonstrated in the previous sections, our $\hat{q}_{OLS}$ is often a better minimizer than even the original value of q^*, therefore we will approximate q_0 in the above equations by $\hat{q}_{OLS}$. In particular, if we denote the covariance matrix as $C_0 = \sigma_0^2 \left[\mathcal{E}^T(q_0)\mathcal{E}(q_0) \right]^{-1}$, then we will approximate C_0 by $C = \sigma_{OLS}^2 \left[\mathcal{E}^T(\hat{q}_{OLS})\mathcal{E}(\hat{q}_{OLS}) \right]^{-1}$, where

$$\sigma_{OLS}^2 = \frac{1}{N_s - 2} \sum_{i=1}^{N_s} \left(|E(t_i, 0; \hat{q}_{OLS})| - |\hat{E}_i| \right)^2.$$

We compute σ_{OLS}^2 by multiplying our J_{min} by an appropriate conversion factor, since they are defined in a similar manner. However, in order to compute the partial derivatives with respect to d and δ in $\mathcal{E}$ we employ forward differencing, which requires an additional forward simulation for each q_j. For $\hat{q} = \hat{q}_{OLS}$ we have, for example

$$\mathcal{E}_{i1} = \frac{\partial |E|}{\partial q_1}(t_i, 0; \hat{q}) \approx \frac{|E\left(t_i, 0; [\hat{q}_1, \hat{q}_2]\right)| - |E(t_i, 0; [(1 - h_d)\hat{q}_1, \hat{q}_2])|}{h_d \hat{q}_1}$$

and similarly for each $\mathcal{E}_{i2}$. In our computations we used the relative differencing factor of $h_d = 1 \times 10^{-4}$. One could also use a sensitivity equations approach (e.g., see [ABBS03] and the references therein), but since the variational equations are quite difficult to solve for this example, we choose instead to approximate the partial derivatives with respect to q directly with our simulations.

We also need to point out that while taking the absolute value of a function limits differentiability at a small number of points, the derivative does exist almost everywhere. The absolute value function does not change the magnitude of the derivative where it exists, which is what we need to compute the dot product of $\mathcal{E}$ with itself. By using finite differences to estimate derivatives, we are essentially under-estimating at the discontinuities. Under-estimating a few points out of thousands is not going to significantly change our covariance matrix. (Alternatively, one could have defined the objective function by squaring the signals instead of taking absolute values to avoid this problem. In this research we were interested in comparing J_1 and J_2 in previous sections above and changing the scale of E by squaring it would have prevented this.)

With $\mathcal{E}$ calculated, we can now evaluate $C = \sigma_{OLS}^2 \left[\mathcal{E}^T(\hat{q}_{OLS})\mathcal{E}(\hat{q}_{OLS})\right]^{-1}$. Then the standard error for $q_1 = d$ is estimated by $\sqrt{C_{11}}$ while the standard error for $q_2 = \delta$ is estimated by $\sqrt{C_{22}}$. See Tables 2.21 through 2.28 for confidence intervals relating to various d^*, δ^* and ν_r values. For example, in the case of $d^* = .02$, $\delta^* = .0002$ and with $\nu_r = .01$ our covariance matrix is

$$C = \begin{bmatrix} 2.37122 \times 10^{-15} & -4.43815 \times 10^{-15} \\ -4.43815 \times 10^{-15} & 9.1829 \times 10^{-15} \end{bmatrix}$$

which results in the confidence intervals $d \in (2.00004 \pm 4.86952 \times 10^{-6}) \times 10^{-2}$ and $\delta \in (1.9941 \pm 0.000958274) \times 10^{-4}$.

The width of these bounds are $\pm 0.000243471\%$ and $\pm 0.0480555\%$ of the approximation value respectively. For the $d^* = .02$ case, the average size of the confidence intervals for $\nu_r = .01, .05, .1$ respectively were $\pm .0002\%$, $\pm .001\%$, $\pm .002\%$ (averaged over various δ^* values ranging from .0001 to .0008). It is interesting that the widths of the confidence intervals nearly exactly double, on average, when the noise level doubles. For the $d^* = .04$ case the average size of the confidence intervals were $\pm .0001\%, \pm .0006\%, \pm .001\%$. Likewise, when the widths of the confidence intervals for $\delta^* = .0002$ are averaged over several various d^* values $(.02, .04, .08)$ we obtain $\pm .05999\%, \pm .2883\%, \pm .5718\%$ for $\nu_r = .01, .05, .1$ respec-

tively. For $\delta^* = .0004$ the averages are $\pm.03331\%, \pm.1575\%, \pm.3154\%$. In general, larger d^* and δ^* values have smaller (tighter) confidence intervals. This suggests that the approximations found in these cases are better than those estimating small parameters. While this is intuitive, it is not apparent looking at the estimates themselves or even the final objective function values (see, for example, Table 2.7).

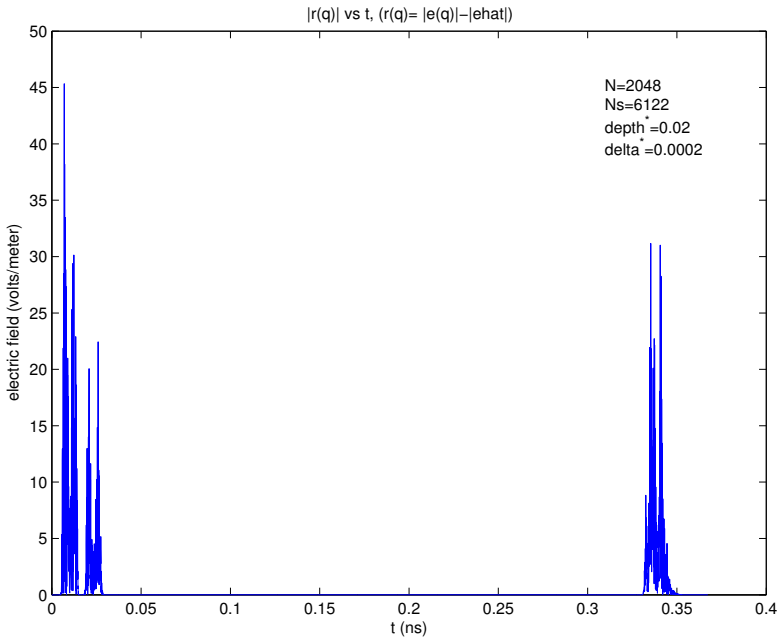

Figure 2.60: Plots of the absolute value of the residual $r_i = |E(t_i, 0; \hat{q}_{OLS})| - |\hat{E}_i|$ versus time t_i when the data contains relative random noise.

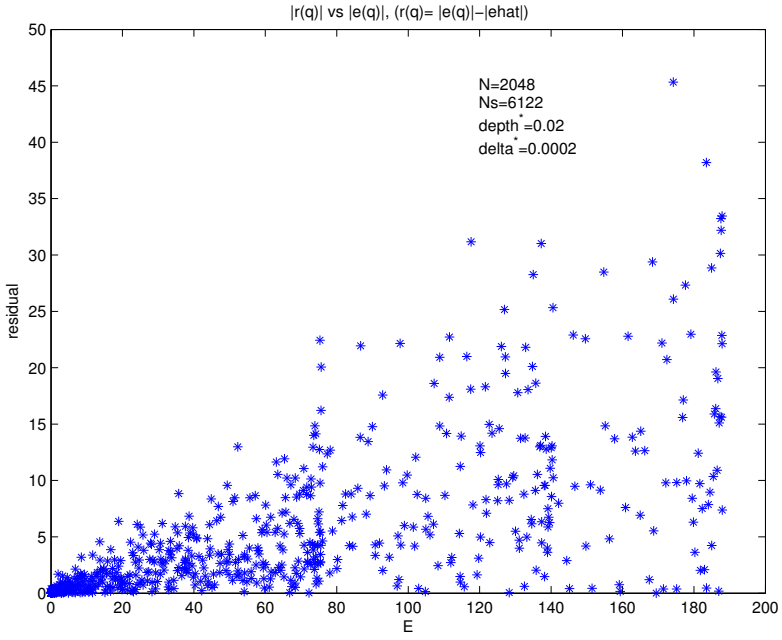

Figure 2.61: Plots of the absolute value of the residual $r_i = |E(t_i, 0; \hat{q}_{OLS})| - |\hat{E}_i|$ versus the absolute value of the electric field $E(t_i, 0; \hat{q}_{OLS})$ when the data contains relative random noise.

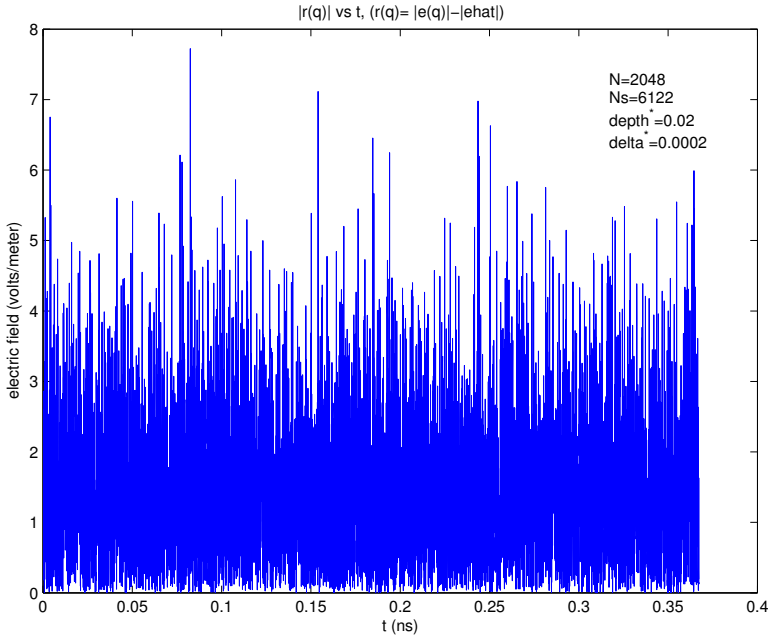

Figure 2.62: Plots of the absolute value of the residual $r_i = |E(t_i, 0; \hat{q}_{OLS})| - |\hat{E}_i|$ versus time t_i when the data contains constant variance random noise.

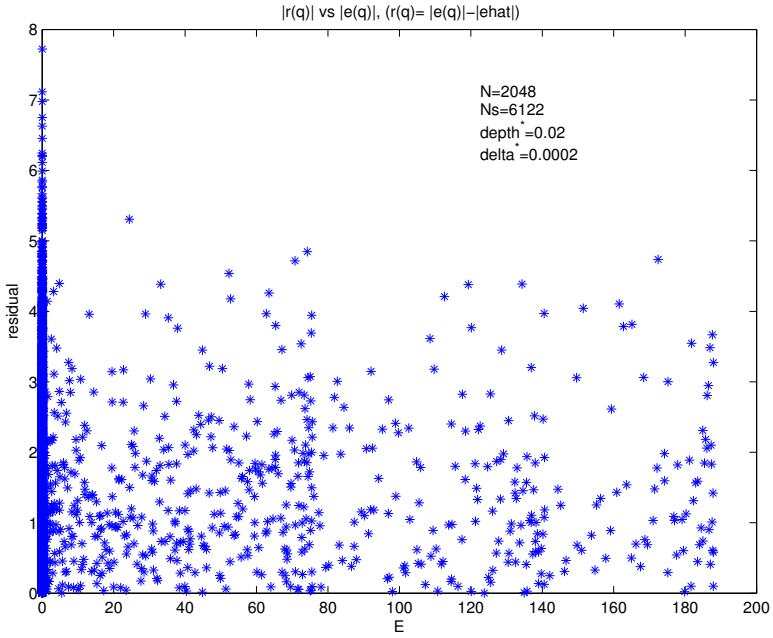

Figure 2.63: Plots of the absolute value of the residual $r_i = |E(t_i, 0; \hat{q}_{OLS})| - |\hat{E}_i|$ versus the absolute value of the electric field $E(t_i, 0; \hat{q}_{OLS})$ when the data contains constant variance random noise.

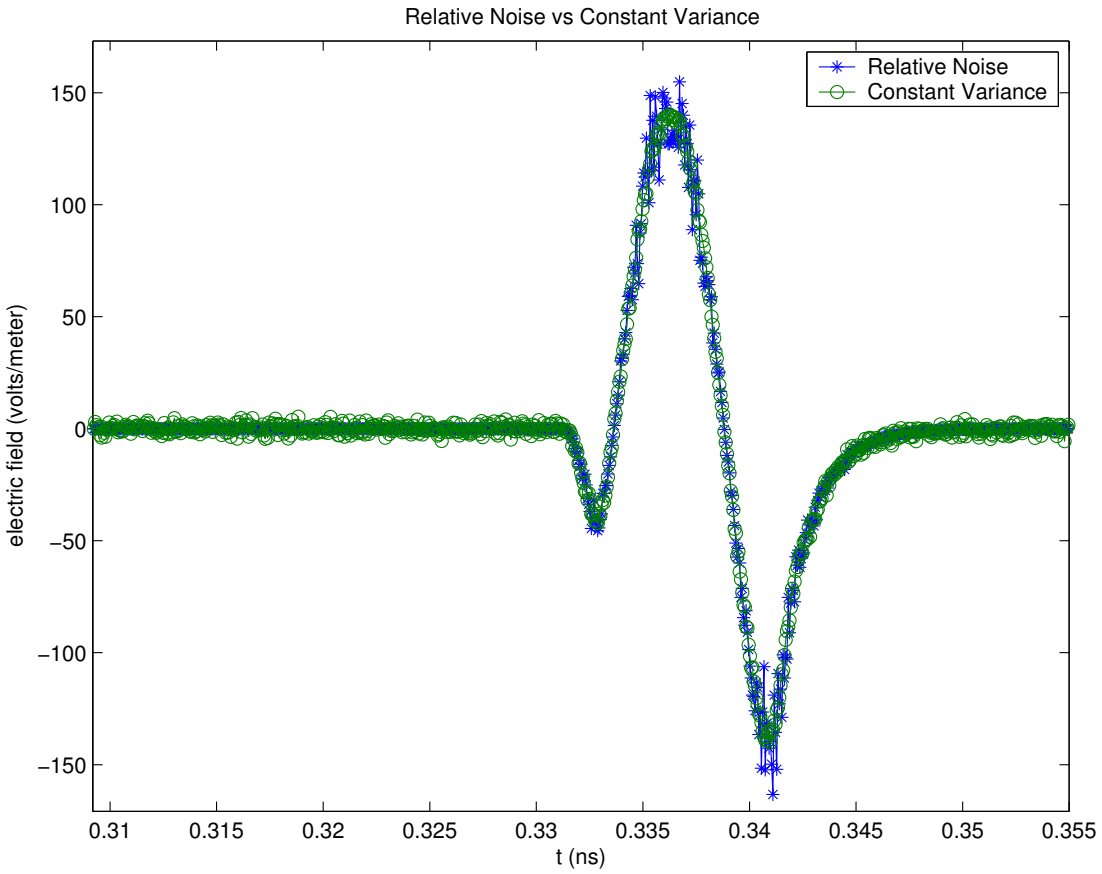

Figure 2.64: The difference between data with relative noise added and data with constant variance noise added is clearly evident when E is close to zero or very large.

Table 2.21: Confidence intervals for the OLS estimate of d when the data is generated with no noise (i.e., $\nu_r = 0.0$).

δ	$d^* = .02$ $(N = 2048)$	$d^* = .04$ $(N = 4096)$
.0002	$(2.00005 \pm 9.30284 \times 10^{-7}) \times 10^{-2}$	$(4.00013 \pm 1.62162 \times 10^{-6}) \times 10^{-2}$
.0004	$(2.00001 \pm 6.50411 \times 10^{-7}) \times 10^{-2}$	$(4.00001 \pm 1.19064 \times 10^{-6}) \times 10^{-2}$
.0008	$(2.00001 \pm 4.91232 \times 10^{-7}) \times 10^{-2}$	$(4.00002 \pm 9.05240 \times 10^{-7}) \times 10^{-2}$

Table 2.22: Confidence intervals for the OLS estimate of d when the data is generated with noise level $\nu_r = .01$.

δ	$d^* = .02$ $(N = 2048)$	$d^* = .04$ $(N = 4096)$
.0002	$(2.00004 \pm 4.86952 \times 10^{-6}) \times 10^{-2}$	$(4.00013 \pm 5.69385 \times 10^{-6}) \times 10^{-2}$
.0004	$(2.00001 \pm 3.50259 \times 10^{-6}) \times 10^{-2}$	$(4.00001 \pm 4.02428 \times 10^{-6}) \times 10^{-2}$
.0008	$(2.00001 \pm 2.87772 \times 10^{-6}) \times 10^{-2}$	$(4.00001 \pm 3.32933 \times 10^{-6}) \times 10^{-2}$

Table 2.23: Confidence intervals for the OLS estimate of d when the data is generated with noise level $\nu_r = .05$.

δ	$d^* = .02$ $(N = 2048)$	$d^* = .04$ $(N = 4096)$
.0002	$(2.00004 \pm 2.41541 \times 10^{-5}) \times 10^{-2}$	$(4.00014 \pm 2.76640 \times 10^{-5}) \times 10^{-2}$
.0004	$(2.00000 \pm 1.68896 \times 10^{-5}) \times 10^{-2}$	$(4.00001 \pm 1.90853 \times 10^{-5}) \times 10^{-2}$
.0008	$(2.00003 \pm 1.40398 \times 10^{-5}) \times 10^{-2}$	$(4.00000 \pm 1.60390 \times 10^{-5}) \times 10^{-2}$

Table 2.24: Confidence intervals for the OLS estimate of d when the data is generated with noise level $\nu_r = .1$.

δ	$d^* = .02$ $(N = 2048)$	$d^* = .04$ $(N = 4096)$
.0002	$(2.00000 \pm 4.72903 \times 10^{-5}) \times 10^{-2}$	$(4.00014 \pm 5.48283 \times 10^{-5}) \times 10^{-2}$
.0004	$(2.00003 \pm 3.39327 \times 10^{-5}) \times 10^{-2}$	$(4.00002 \pm 3.87474 \times 10^{-5}) \times 10^{-2}$
.0008	$(2.00003 \pm 2.79911 \times 10^{-5}) \times 10^{-2}$	$(4.00003 \pm 3.19526 \times 10^{-5}) \times 10^{-2}$

Table 2.25: Confidence intervals for the OLS estimate of δ when the data is generated with no noise (i.e., $\nu_r = 0.0$).

δ	$d^* = .02$ $(N = 2048)$	$d^* = .04$ $(N = 4096)$
.0002	$(1.99272 \pm 0.000182978) \times 10^{-4}$	$(1.98142 \pm 0.000317616) \times 10^{-4}$
.0004	$(4.00035 \pm 0.000201885) \times 10^{-4}$	$(4.00737 \pm 0.000369841) \times 10^{-4}$
.0008	$(7.99833 \pm 0.000136586) \times 10^{-4}$	$(8.00332 \pm 0.000251291) \times 10^{-4}$

Table 2.26: Confidence intervals for the OLS estimate of δ when the data is generated with noise level $\nu_r = .01$.

δ	$d^* = .02$ $(N = 2048)$	$d^* = .04$ $(N = 4096)$
.0002	$(1.99410 \pm 0.000958274) \times 10^{-4}$	$(1.98029 \pm 0.00111475) \times 10^{-4}$
.0004	$(4.00170 \pm 0.00108740) \times 10^{-4}$	$(4.00667 \pm 0.0012499) \times 10^{-4}$
.0008	$(7.99882 \pm 0.000800042) \times 10^{-4}$	$(8.00486 \pm 0.000923838) \times 10^{-4}$

Table 2.27: Confidence intervals for the OLS estimate of δ when the data is generated with noise level $\nu_r = .05$.

δ	$d^* = .02$ $(N = 2048)$	$d^* = .04$ $(N = 4096)$
.0002	$(1.99606 \pm 0.00475672) \times 10^{-4}$	$(1.98106 \pm 0.00541764) \times 10^{-4}$
.0004	$(4.00190 \pm 0.00524360) \times 10^{-4}$	$(4.01214 \pm 0.00593246) \times 10^{-4}$
.0008	$(7.99045 \pm 0.00391181) \times 10^{-4}$	$(8.00947 \pm 0.00444525) \times 10^{-4}$

Table 2.28: Confidence intervals for the OLS estimate of δ when the data is generated with noise level $\nu_r = .1$.

δ	$d^* = .02$ $(N = 2048)$	$d^* = .04$ $(N = 4096)$
.0002	$(2.00017 \pm 0.00932701) \times 10^{-4}$	$(1.97674 \pm 0.0107203) \times 10^{-4}$
.0004	$(4.00070 \pm 0.0105331) \times 10^{-4}$	$(4.01229 \pm 0.0120445) \times 10^{-4}$
.0008	$(7.99698 \pm 0.00778563) \times 10^{-4}$	$(8.00361 \pm 0.00886925) \times 10^{-4}$

2.5 Conclusions

In this section, we have explored a "proof of concept" formulation of an inverse problem to detect and characterize voids or gaps inside of, or behind, a Dielectric medium. We have simplified the problem to one dimension and used Maxwell's equations to model a pulsed, normally incident electromagnetic interrogating signal. We use Finite Element discretization in space, and Finite Differences in time, to simulate the electric field in the time domain. This is coupled with a Levenberg-Marquardt scheme in an optimization step with an innovative cost functional appropriate for reflected waves where phase differences can produce ill-posedness in the inverse problem when one uses the usual ordinary least squares criterion. We have successfully demonstrated that it is possible to resolve gap widths on the order of $.2mm$ between a dielectric slab of $20cm$ and a metal (perfectly conducting) surface using an interrogating signal with a $3mm$ wavelength.

Our modified Least Squares objective function corrects for peaks in J which contribute to the ill-posedness. Further, we are able to test on both sides of any detected minima to ensure global minimization. We refer to this procedure as a "check point" method. Although gap widths close to $\frac{\lambda}{8}$ are the most difficult for us to initially estimate, our optimization routine still converged to the correct minimizer in this regime. Ultimately we were able to detect a $.0002m$ wide crack behind a $20cm$ deep slab, however the inverse problem took approximately $10hrs$ to complete. We note that adding random noise (equivalent to about 20% relative noise) does not significantly hinder our inverse problem solution method, and only slightly broadens the confidence intervals.

Future work on this problem will likely involve more efficient computational methods since currently the inverse problem involving a $20cm$ slab takes too long to be practically useful. Further, more sophisticated models for describing the polarization mechanisms in non-homogenous materials must be developed, which we will discuss in the following sections. Finally, in order to take scattering and non-normally incident electromagnetic signals into account, multi-dimensional models will be necessary.

Chapter 3

Multiple Debye Polarization Mechanisms

The simulations and inverse problem computations in the previous section employed a simple Debye polarization model

$$\tau \dot{P} + P = \epsilon_0(\epsilon_s - \epsilon_\infty)E$$

which could also be written

$$P(t,z) = \int_0^t g(t-s,z;\tau)E(s,z)ds$$

where

$$g(t;\tau) = \epsilon_0(\epsilon_s - \epsilon_\infty)/\tau \;\; e^{-t/\tau}.$$

This presupposes that the material may be sufficiently described by a single relaxation parameter τ. We know the foam in our problem is a composite of (mainly two) different substances.

Therefore, we consider the definition of the electric polarization given by the following convolution operator:

$$P(t,z) = \int_0^t \mathcal{G}(t-s,z)E(s,z)ds$$

where $\mathcal{G}$ is determined by various polarization mechanisms each described by a different parameter τ, and may be written

$$\mathcal{G}(t,z;F) = \int_{\mathcal{T}} g(t,z;\tau)dF(\tau)$$

where $\mathcal{T} \subset [\tau_1, \tau_2]$ and F is a probability measure. In this way we can model systems dependent on distributions of polarization relaxation parameters, instead of a single parameter.

In the next section we demonstrate that systems determined by multiple relaxation parameters (e. g., two), may be fundamentally distinct from simple, single Debye systems. This implies that models must account for all the polarization mechanisms when trying to accurately represent a physical system. In a Chapter 5 we use a least squares inverse problem formulation to attempt to recover the polarization mechanisms (i. e., the two relaxation times used to generate the data) from observations on the electric field. This research shows that in certain cases an effective, single parameter may sufficiently determine the dynamics, but the formula for this parameter is dependent on the relative magnitudes of the frequency and the relaxations times themselves.

Maxwell's equations in one dimension can be simplified to

$$\begin{aligned} \mu_0\epsilon_0\epsilon_r(z)\ddot{E} + \mu_0 I_\Omega \ddot{P} + \mu_0\sigma(z)\dot{E} - E'' &= -\mu_0\dot{J}_s \qquad \text{in } \Omega \cup \Omega_0 \qquad (3.1)\\ [\dot{E} - cE']_{z=0} &= 0 \\ [\dot{E} + cE']_{z=1} &= 0 \\ E(0,z) &= 0 \\ \dot{E}(0,z) &= 0 \end{aligned}$$

with absorbing boundary conditions at $z = 0$ and $z = 1$, and homogenous initial conditions. The region Ω is defined to be the area inside of the material, and Ω_0 is the (vacuous) region in front of and behind Ω. In some cases the polarization P, might be modeled as a Debye medium with the following differential equation:

$$\tau\dot{P} + P = \epsilon_0(\epsilon_s - \epsilon_\infty)E \qquad \text{in } \Omega \qquad (3.2)$$

with $P = 0$ outside of the material.

After scaling P by ϵ_0 and t by c, and applying the boundary conditions, the weak

form of each is as follows:

$$\langle \epsilon_r(z)\ddot{E}, \phi\rangle + \langle I_\Omega \ddot{P}, \phi\rangle + \eta_0\langle \sigma(z)\dot{E}, \phi\rangle + \langle E', \phi'\rangle + \dot{E}(t,1)\phi(1) + \dot{E}(t,0)\phi(0) = -\eta_0\langle \dot{J}_s, \phi\rangle \tag{3.3}$$

$$\langle \dot{P}, \phi\rangle_\Omega + \lambda\langle P, \phi\rangle_\Omega = \lambda\epsilon_d\langle E, \phi\rangle_\Omega, \tag{3.4}$$

where $\lambda = \frac{1}{c\tau}$, $\epsilon_d = \epsilon_s - \epsilon_\infty$, and $\eta_0 = \sqrt{\frac{\mu_0}{\epsilon_0}}$.

To simplify the dependence of E on P, we differentiate (3.4):

$$\begin{aligned}\langle \ddot{P}, \phi\rangle_\Omega &= -\lambda\langle \dot{P}, \phi\rangle_\Omega + \epsilon_d\lambda\langle \dot{E}, \phi\rangle_\Omega \\ &= \lambda^2\langle P, \phi\rangle_\Omega - \lambda^2\epsilon_d\langle E, \phi\rangle_\Omega + \lambda\epsilon_d\langle \dot{E}, \phi\rangle_\Omega\end{aligned} \tag{3.5}$$

which we substitute into (3.3) to obtain

$$\begin{aligned}&\langle \epsilon_r(z)\ddot{E}, \phi\rangle + \lambda^2\langle I_\Omega P, \phi\rangle - \lambda^2\epsilon_d\langle I_\Omega E, \phi\rangle \\ &\quad + \lambda\epsilon_d\langle I_\Omega\dot{E}, \phi\rangle + \eta_0\langle \sigma(z)\dot{E}, \phi\rangle + \langle E', \phi'\rangle + \dot{E}(t,1)\phi(1) + \dot{E}(t,0)\phi(0) = -\eta_0\langle \dot{J}_s, \phi\rangle.\end{aligned}$$

If we assume that Ω_0 is a vacuum, then $\epsilon_r(z) = 1$ in Ω_0 and $\epsilon_r(z) = \epsilon_\infty$ otherwise. Further, $\sigma(z) = 0$ in Ω_0 and a constant, say σ, otherwise. We apply these assumptions, and combine like terms to obtain

$$\begin{aligned}&\langle [1 + I_\Omega(\epsilon_\infty - 1)]\,\ddot{E}, \phi\rangle + \lambda^2\langle I_\Omega P, \phi\rangle - \lambda^2\epsilon_d\langle I_\Omega E, \phi\rangle \\ &\quad + (\lambda\epsilon_d + \eta_0\sigma)\langle I_\Omega\dot{E}, \phi\rangle + \langle E', \phi'\rangle + \dot{E}(t,1)\phi(1) + \dot{E}(t,0)\phi(0) = -\eta_0\langle \dot{J}_s, \phi\rangle.\end{aligned} \tag{3.6}$$

Now suppose that the medium in question is heterogeneous containing two materials having different Debye polarization mechanisms, say with corresponding relaxation times τ_1 and τ_2. If our medium is composed of a weighted average of the materials, then we may expect our total polarization likewise to be a weighted average

$$P = \alpha_1 P_1 + \alpha_2 P_2 \tag{3.7}$$

where $\alpha_1 + \alpha_2 = 1$, and each P_i satisfies (3.2) with the corresponding relaxation parameter τ_i for $i = 1, 2$. Differentiating these equations, and substituting them into the second derivative of (3.7) we obtain

$$\begin{aligned}\ddot{P} &= \alpha_1(\lambda_1^2 P_1 - \lambda_1^2\epsilon_d E + \lambda_1\epsilon_d\dot{E}) + \alpha_2(\lambda_2^2 P_2 - \lambda_2^2\epsilon_d E + \lambda_2\epsilon_d\dot{E}) \\ &= \alpha_1\lambda_1^2 P_1 + \alpha_2\lambda_2^2 P_2 - (\alpha_1\lambda_1^2 + \alpha_2\lambda_2^2)\epsilon_d E + (\alpha_1\lambda_1 + \alpha_2\lambda_2)\epsilon_d\dot{E}.\end{aligned} \tag{3.8}$$

When the weak form of (3.8) is substituted into (3.3), we have

$$\begin{aligned}\langle [1 + I_\Omega(\epsilon_\infty - 1)]\,\ddot{E}, \phi\rangle + \alpha_1\lambda_1^2\langle I_\Omega P_1, \phi\rangle + \alpha_2\lambda_2^2\langle I_\Omega P_2, \phi\rangle \\ - \alpha_1\lambda_1^2\epsilon_d\langle I_\Omega E, \phi\rangle - \alpha_2\lambda_2^2\epsilon_d\langle I_\Omega E, \phi\rangle + (\alpha_1\lambda_1\epsilon_d + \alpha_2\lambda_2\epsilon_d + \eta_0\sigma)\langle I_\Omega \dot{E}, \phi\rangle \\ + \langle E', \phi'\rangle + \dot{E}(t,1)\phi(1) + \dot{E}(t,0)\phi(0) = -\eta_0\langle \dot{J}_s, \phi\rangle. \quad (3.9)\end{aligned}$$

Now suppose we define $\tilde{\lambda} := \alpha_1\lambda_1 + \alpha_2\lambda_2$, $\tilde{\tilde{\lambda}} := \alpha_1\lambda_1^2 + \alpha_2\lambda_2^2$, and $\tilde{P} := (\alpha_1\lambda_1^2 P_1 + \alpha_2\lambda_2^2 P_2)/\tilde{\tilde{\lambda}}$. Then (3.9) becomes

$$\begin{aligned}\langle [1 + I_\Omega(\epsilon_\infty - 1)]\,\ddot{E}, \phi\rangle + \tilde{\tilde{\lambda}}\langle I_\Omega \tilde{P}, \phi\rangle - \tilde{\tilde{\lambda}}\epsilon_d\langle I_\Omega E, \phi\rangle \\ + (\tilde{\lambda}\epsilon_d + \eta_0\sigma)\langle I_\Omega \dot{E}, \phi\rangle + \langle E', \phi'\rangle + \dot{E}(t,1)\phi(1) + \dot{E}(t,0)\phi(0) = -\eta_0\langle \dot{J}_s, \phi\rangle, \quad (3.10)\end{aligned}$$

where is it clear that $\tilde{\lambda}$ corresponds to the previous λ, (e.g. in (3.6)), $\tilde{\tilde{\lambda}}$ corresponds to the previous λ^2, and the electric field depends on the weighted average of each $\lambda_i^2 P_i$ given by $\tilde{\tilde{\lambda}}\tilde{P}$. We can check that if $\lambda_1 = \lambda_2$ then $\tilde{\lambda} = \lambda$, etc. However, for $\lambda_1 \neq \lambda_2$ there is no single λ value such that the dynamics of (3.6) is the same as that of (3.10). In particular, one would need for this single value of λ to satisfy both $\lambda = \alpha_1\lambda_1 + \alpha_2\lambda_2$ and $\lambda^2 = \alpha_1\lambda_1^2 + \alpha_2\lambda_2^2$.

Still, it may be possible that one or the other of these terms dominates the behavior of E. Therefore we test simulations from various values of a single parameter $\tau = \frac{1}{c\lambda}$ against the electric field simulated using two Debye polarization equations, with relaxation times τ_1 and τ_2, respectively. In Figure 3.1 we plot snap shots of the simulation using $\tau_1 = 10^{-13}$ and $\tau_2 = 10^{-12}$ (with $\alpha_1 = \alpha_2 = .5$). We can compare this result to the single Debye simulations using $\tau = 10^{-13}$ in Figure 3.2, or using $\tau = 10^{-12}$ in Figure 3.3. The electric field plotted in Figure 3.1 does appear to be, in some sense, an average between the two single Debye cases. If we take $\lambda = \tilde{\lambda}$ then $\tilde{\tau} = \frac{2\tau_1\tau_2}{\tau_1+\tau_2} = 1.8182 \times 10^{-13}$. The simulation resulting from this relaxation time is given in Figure 3.4. We see that it is "closer" than the previous two single Debye simulations, but still not completely similar. Using $\lambda^2 = \tilde{\tilde{\lambda}}$ gives $\tilde{\tilde{\tau}} = \frac{\sqrt{2}\tau_1\tau_2}{\sqrt{\tau_1^2+\tau_2^2}} = 1.41 \times 10^{-13}$, and its simulation is displayed in Figure 3.5.

A more drastic example is given by $\tau_1 = 10^{-13}$ and $\tau_2 = 3.16 \times 10^{-8}$. In Figure 3.6 we plot snap shots of the simulation using $\tau_1 = 10^{-13}$ and $\tau_2 = 3.16 \times 10^{-8}$ (with $\alpha_1 = \alpha_2 = .5$). Again, we can compare this result to the single Debye simulations using $\tau = 10^{-13}$ in Figure 3.2 and using $\tau = 3.16 \times 10^{-8}$ in Figure 3.7. (Note that the times in Figure 3.7 are different from the rest of the Figures since the signal with this relaxation time travels four times as fast through the material.) If we take $\lambda = \tilde{\lambda}$ then $\tilde{\tau} = \frac{2\tau_1\tau_2}{\tau_1+\tau_2} = 2\times 10^{-13}$.

The simulation resulting from this relaxation time is given in Figure 3.8. Using $\lambda^2 = \tilde{\tilde{\lambda}}$ again gives $\tilde{\tilde{\tau}} = \frac{\sqrt{2}\tau_1\tau_2}{\sqrt{\tau_1^2+\tau_2^2}} = 1.41 \times 10^{-13}$, which was previously displayed in Figure 3.5. Of these possible single Debye simulations, it appears that $\tau = 10^{-13}$ does the best job of structurally matching the signal from the double Debye simulation. But when we pay attention to the speed of the signal in these snapshots, we see that the $\tau = 10^{-13}$ signal is at least half of a wavelength behind the double Debye signal after $.36732ns$. Also, the $\tau = 3.16 \times 10^{-8}$ signal is much too fast. To match the speed of this double Debye signal (as measured by the leading negative peak), we need τ to be on the order of 10^{-11}. A single Debye simulation using this value is plotted in Figure 3.9, but this clearly does not match the structure of the double Debye simulation. Therefore we conclude that the multiple Debye formulation is fundamentally distinct from the single Debye formulation.

It should be noted that the relaxation parameter of a material is generally related to its relative permittivity. Therefore, a more rigorous argument would take this into account by solving the two parameter inverse problem of matching simulations using $\epsilon_d = \epsilon_s - \epsilon_\infty$ and τ in the single Debye model with data generated by a multiple Debye simulation. One difficulty in solving this inverse problem is that simply applying an ordinary least squares formulation would not properly recognize the "closeness" of a signal that is merely phase-shifted due to a decreased effective speed such as in the examples above. It may be useful to derive an estimate of the speed of the signal in terms of ϵ_d and τ, and then solve a one parameter inverse problem along the line of constant speed.

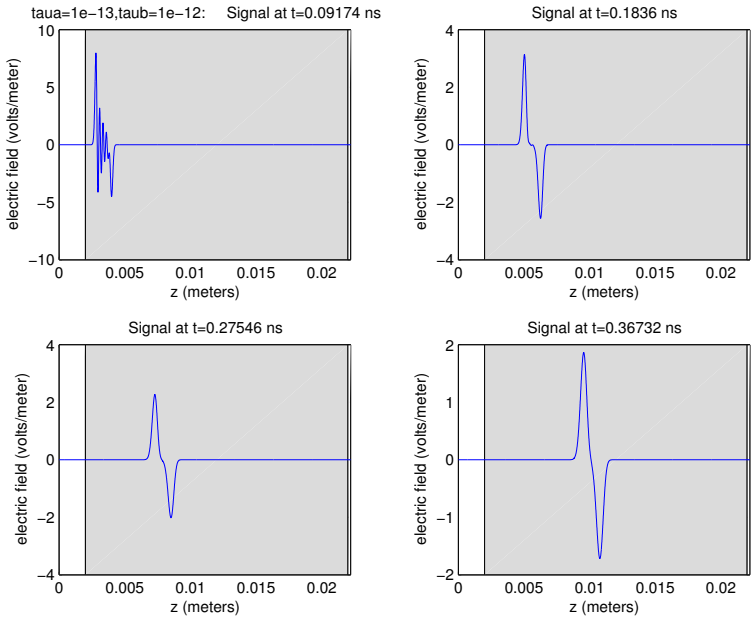

Figure 3.1: Computed solutions at various different times of a windowed electromagnetic pulse traveling through a multiple Debye medium with relaxation parameters $\tau_1 = 10^{-13}$ and $\tau_2 = 10^{-12}$.

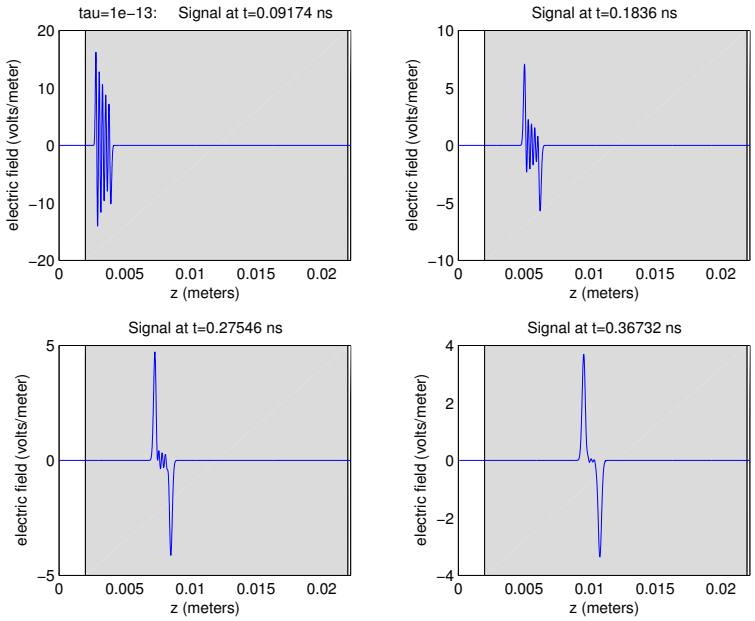

Figure 3.2: Computed solutions at various different times of a windowed electromagnetic pulse traveling through a Debye medium using the single relaxation parameter $\tau = 10^{-13}$.

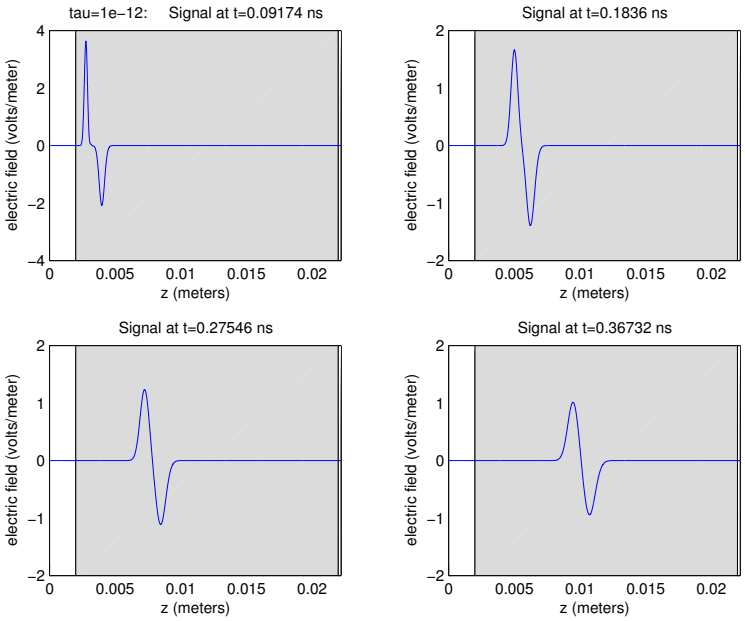

Figure 3.3: Computed solutions at various different times of a windowed electromagnetic pulse traveling through a Debye medium using the single relaxation parameter $\tau = 10^{-12}$.

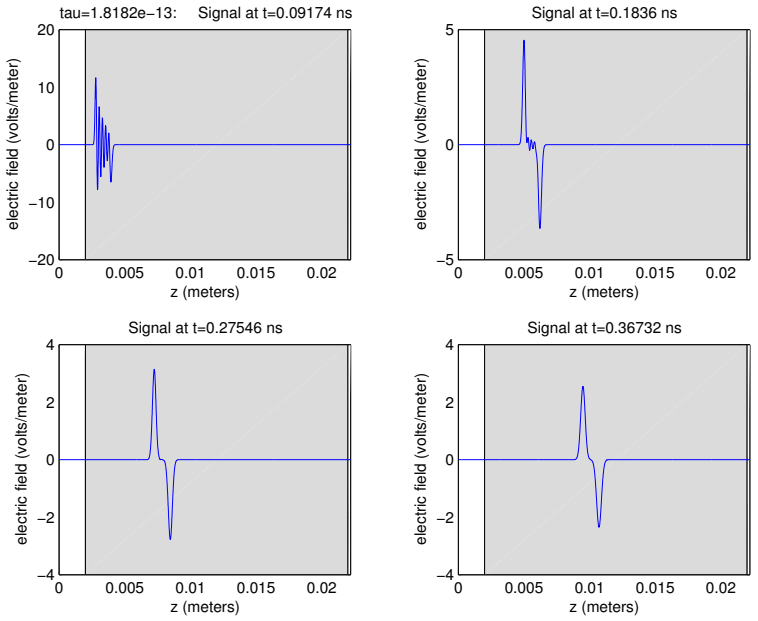

Figure 3.4: Computed solutions at various different times of a windowed electromagnetic pulse traveling through a Debye medium using the single relaxation parameter $\tilde{\tau} = 1.8182 \times 10^{-13}$.

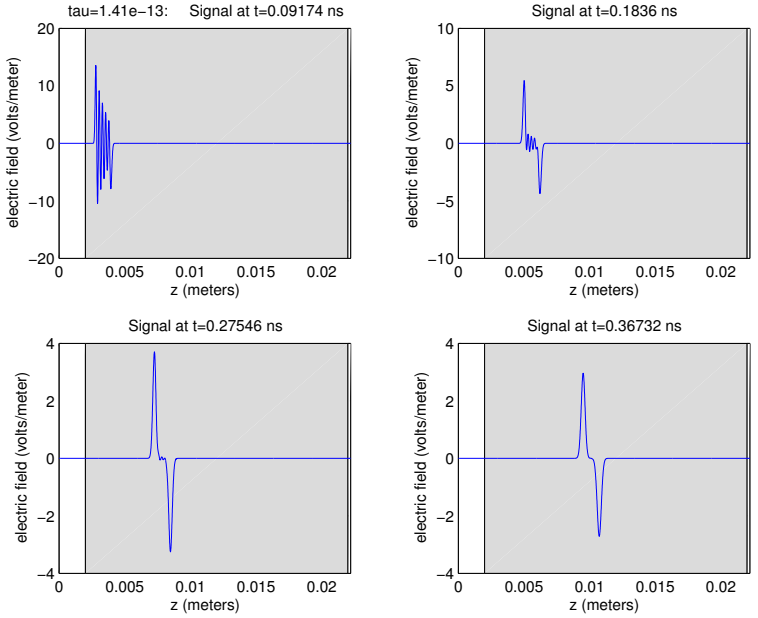

Figure 3.5: Computed solutions at various different times of a windowed electromagnetic pulse traveling through a Debye medium using the single relaxation parameter $\tilde{\tilde{\tau}} = 1.41 \times 10^{-13}$.

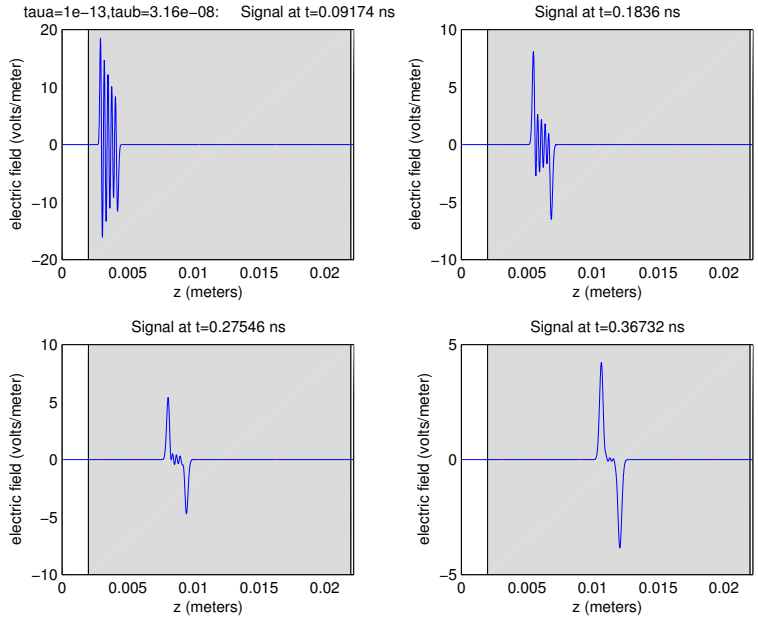

Figure 3.6: Computed solutions at various different times of a windowed electromagnetic pulse traveling through a multiple Debye medium with relaxation parameters $\tau_1 = 10^{-13}$ and $\tau_2 = 3.16 \times 10^{-8}$.

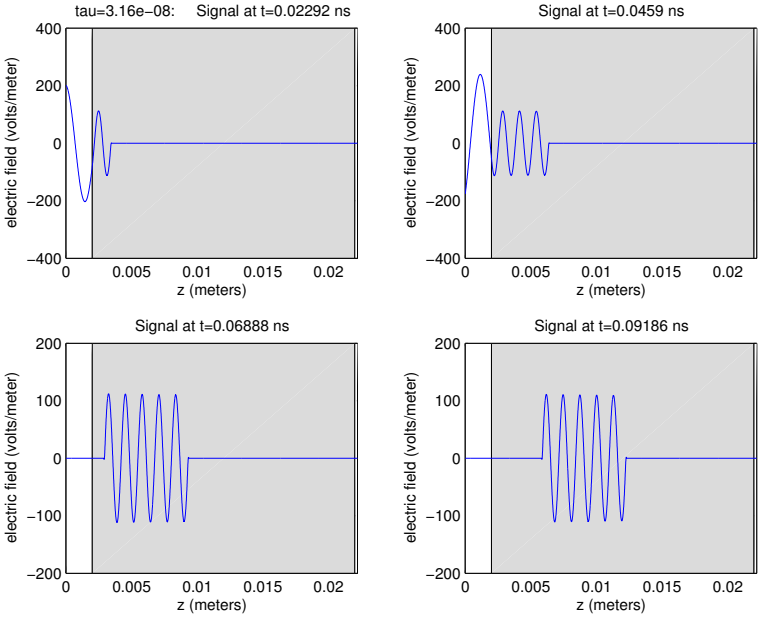

Figure 3.7: Computed solutions at various different times of a windowed electromagnetic pulse traveling through a Debye medium using the single relaxation parameter $\tau = 3.16 \times 10^{-8}$. Note that the times are different from the other Figures since the signal with this relaxation time travels four times as fast through the material.

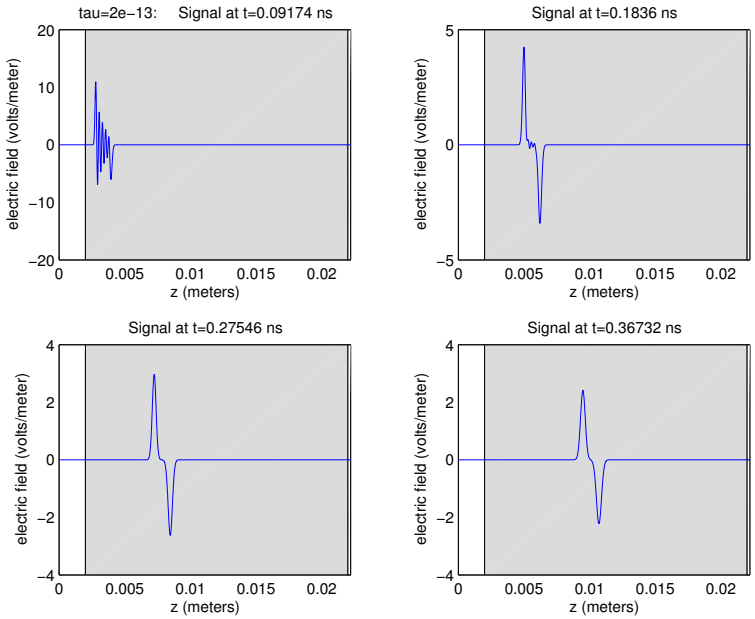

Figure 3.8: Computed solutions at various different times of a windowed electromagnetic pulse traveling through a Debye medium using the single relaxation parameter $\tilde{\tau} = 2\times10^{-13}$.

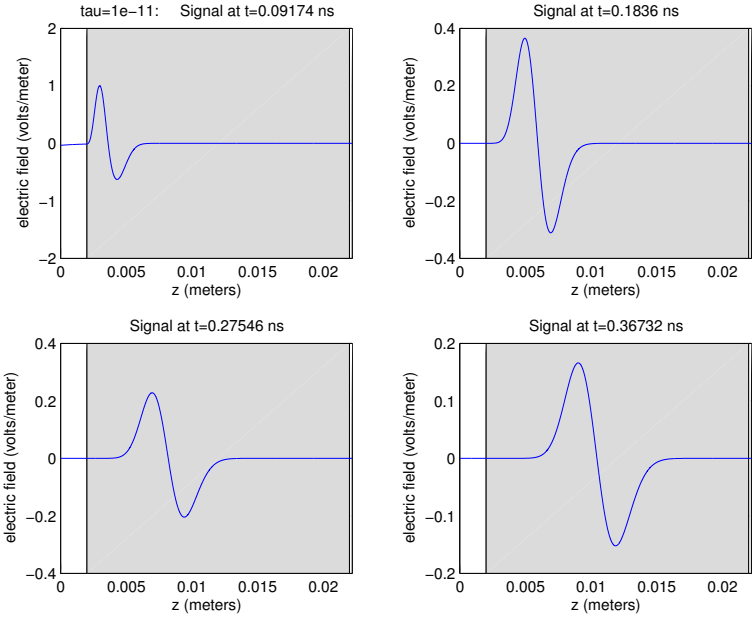

Figure 3.9: Computed solutions at various different times of a windowed electromagnetic pulse traveling through a Debye medium using the single relaxation parameter $\tau = 10^{-11}$.

Chapter 4

Well-Posedness in Maxwell Systems with Distributions of Polarization Relaxation Parameters

In the previous section we have shown that determination of polarization mechanisms is important to accurate representation of the behavior of the electric field and the electric polarization in a material. Therefore, it will be of significant importance to have an inverse problem methodology that can determine the unknown dielectric parameters which govern the physical system. In this section we consider well-posedness questions for the variational solutions of one dimensional Maxwell's equations with an absorbing left boundary condition, a supraconducting right boundary condition and a general macroscopic polarization term which includes uncertainty in the dielectric parameters (see [BG04]). For these solutions, we establish existence, uniqueness and continuous dependence on the uncertainty measures in a Prohorov metric (see [B68], [BB01] for definitions and details) sense. As

explained below, these results can be readily used in an inverse problem methodology to determine the unknown distribution of the dielectric parameters which govern the behavior of the electric field and the electric polarization in a general heterogeneous material with multiple mechanisms (Debye, Lorentz, etc.) and relaxation parameters.

4.1 Problem Formulation

We consider the one dimensional problem formulation of the interrogation problem as above. Assuming $D = \epsilon E + P$, we may obtain Maxwell's equations in second order form given by:

$$\mu_0 \epsilon \ddot{E} + \mu_0 \ddot{P} + \mu_0 \sigma \dot{E} - E'' = -\mu_0 \dot{J}_s \text{ in } \Omega \cup \Omega_0, \tag{4.1}$$

where E is the transverse component of the electric field, P is the material macroscopic electric polarization, $\epsilon = \epsilon(z)$ is the dielectric permittivity and $\sigma = \sigma(z)$ is the conductivity of the material. The boundary conditions that we are assuming are absorbing at $z = 0$ and supraconducting at $z = 1$:

$$\left[\dot{E} - cE'\right]_{z=0} = 0, \quad E(t,1) = 0. \tag{4.2}$$

Our initial conditions are

$$E(0,z) = \Phi(z), \quad \dot{E}(0,z) = \Psi(z). \tag{4.3}$$

To describe the behavior of the electric polarization P, we may employ a general integral equation model in which the polarization explicitly depends on the past history of the electric field

$$P(t,z) = \int_0^t g(t-s,z;\tau) E(s,z) ds. \tag{4.4}$$

where g is a polarization kernel (note that $P(0,z)$ is assumed to be 0). This formulation is sufficiently general to include such special cases as the orientational or Debye polarization model, the electronic or Lorentz polarization model, and even linear combinations thereof, as well as other higher order models. In the Debye case the kernel is given by

$$g(t;\tau) = \epsilon_0(\epsilon_s - \epsilon_\infty)/\tau \ \ e^{-t/\tau},$$

while in the Lorentz model, it takes the form

$$g(t;\tau) = \epsilon_0 \omega_p^2/\nu_0 \ e^{-t/2\tau} \sin(\nu_0 t),$$

where $\omega_p = \omega_0\sqrt{\epsilon_s - \epsilon_\infty}$ is referred to as the plasma frequency.

We note that while we have seemingly neglected any instantaneous polarization in our integral equation model, in actual fact we have separated the instantaneous component by assuming it to be related to the electric field by a dielectric constant $P_{in} = \epsilon_0\chi E$ and denoting the remainder of the polarization effects by P. Thus

$$\begin{aligned} D &= \epsilon_0 E + \epsilon_0\chi E + P \\ &= \epsilon_0\epsilon_r E + P, \end{aligned}$$

where $\epsilon_r = 1 + \chi$ is a relative permittivity, so that the permittivity in (4.1) is understood to be $\epsilon(z) = \epsilon_0\epsilon_r(z)$.

The use of these kernels, however, presupposes that the material may be sufficiently defined by a single relaxation parameter τ, which is generally not the case. In order to account for multiple relaxation parameters in the polarization mechanisms, we allow for a distribution of relaxation parameters which may be conveniently described in terms of a probability measure F. Thus, we define our polarization model in terms of a convolution operator

$$P(t,z) = \int_0^t \mathcal{G}(t-s,z)E(s,z)ds$$

where $\mathcal{G}$ is determined by various polarization mechanisms each described by a different parameter τ, and therefore is given by

$$\mathcal{G}(t,z;F) = \int_{\mathcal{T}} g(t,z;\tau)dF(\tau)$$

where $\mathcal{T} = [\tau_1,\tau_2] \subset (0,\infty)$. In particular, if the distribution were discrete, consisting of a single relaxation parameter, then we would again have (4.4).

Note that,

$$\ddot{P}(t,z) = \int_0^t \ddot{\mathcal{G}}(t-s,z)E(s,z)ds + \mathcal{G}(0,z)\dot{E}(t,z) + \dot{\mathcal{G}}(0,z)E(t,z) \tag{4.5}$$

where

$$\ddot{\mathcal{G}}(t,z;F) = \int_{\mathcal{T}} \ddot{g}(t,z;\tau)dF(\tau).$$

Substituting (4.5) into (4.1) we obtain

$$\begin{aligned} \mu_0\epsilon\ddot{E}(t,z) + \mu_0 I_\Omega\left[\sigma + \mathcal{G}(0,z)\right]\dot{E}(t,z) + \mu_0 I_\Omega\dot{\mathcal{G}}(0,z)E(t,z) \\ + \int_0^t \mu_0 I_\Omega\ddot{\mathcal{G}}(t-s,z)E(s,z)ds - E''(t,z) = -\mu_0\dot{J}_s(t,z), \end{aligned}$$

where indicator functions I_Ω have been inserted to explicitly enforce the restriction of polarization and conductivity to the interior of the dielectric material. Due to various physical considerations including dielectric discontinuities across the material interfaces and a truncated interrogating signal, one should not expect classical solutions to exist for these equations in strong form. Therefore it is necessary to convert to weak form, resulting in (after also multiplying both sides by c^2),

$$\langle \tilde{\epsilon_r}\ddot{E}(t,\cdot),\phi\rangle + \langle \frac{1}{\epsilon_0} I_\Omega \left[\sigma + \mathcal{G}(0,\cdot)\right] \dot{E}(t,\cdot),\phi\rangle + \langle \frac{1}{\epsilon_0} I_\Omega \dot{\mathcal{G}}(0,\cdot)E(t,\cdot),\phi\rangle$$
$$+ \langle \frac{1}{\epsilon_0}\int_0^t I_\Omega \ddot{\mathcal{G}}(t-s,\cdot)E(s,\cdot)ds,\phi\rangle - \langle c^2 E''(t,\cdot),\phi\rangle = -\langle \frac{1}{\epsilon_0}\dot{J}_s(t,\cdot),\phi\rangle,$$

where $\tilde{\epsilon_r} = \frac{\epsilon}{\epsilon_0}$ and $\phi \in V = H_R^1(0,1) = \{\phi \in H^1(0,1) : \phi(1) = 0\}$. (Without loss of generality, we will hereafter assume $\tilde{\epsilon_r} = 1$.) Finally, we may integrate by parts, and apply the boundary conditions (4.2) to obtain

$$\langle \ddot{E}(t,\cdot),\phi\rangle + \langle \frac{1}{\epsilon_0} I_\Omega \left[\sigma + \mathcal{G}(0,z)\right] \dot{E}(t,\cdot),\phi\rangle + \langle \frac{1}{\epsilon_0} I_\Omega \dot{\mathcal{G}}(0,\cdot)E(t,\cdot),\phi\rangle$$
$$+ \langle \frac{1}{\epsilon_0}\int_0^t I_\Omega \ddot{\mathcal{G}}(t-s,\cdot)E(s,\cdot)ds,\phi\rangle + \langle c^2 E'(t,\cdot),\phi'\rangle + c\dot{E}(t,0)\phi(0) = -\langle \frac{1}{\epsilon_0}\dot{J}_s(t,\cdot),\phi\rangle,$$

which we can rewrite more compactly as

$$\langle \ddot{E},\phi\rangle + \langle \gamma\dot{E},\phi\rangle + \langle \beta E,\phi\rangle + \langle \int_0^t \alpha(t-s,\cdot)E(s,\cdot)ds,\phi\rangle$$
$$+ \langle c^2 E',\phi'\rangle + c\dot{E}(t,0)\phi(0) = \langle \mathcal{J},\phi\rangle, \quad \phi \in V, \quad (4.6)$$

where

$$\gamma(z) = \frac{1}{\epsilon_0} I_\Omega \left[\sigma(z) + \mathcal{G}(0,z)\right] = \frac{1}{\epsilon_0} I_\Omega \left[\sigma(z) + \int_{\mathcal{T}} g(0,z;\tau)dF(\tau)\right]$$
$$\beta(z) = \frac{1}{\epsilon_0} I_\Omega \dot{\mathcal{G}}(0,z) = \frac{1}{\epsilon_0} I_\Omega \int_{\mathcal{T}} \dot{g}(0,z;\tau)dF(\tau)$$
$$\alpha(t,z) = \frac{1}{\epsilon_0} I_\Omega \ddot{\mathcal{G}}(t,z) = \frac{1}{\epsilon_0} I_\Omega \int_{\mathcal{T}} \ddot{g}(t,z;\tau)dF(\tau)$$
$$\mathcal{J}(t,z) = -\frac{1}{\epsilon_0}\dot{J}_s(t,z).$$

4.2 Estimation Methodology

Our goal is to estimate the probability distribution function (PDF) of relaxation parameters $F \in \mathcal{P}(\mathcal{T})$ in a given model of the polarization, where $\mathcal{P}(\mathcal{T})$ is the set of all

PDFs on the Borel subsets of the admissible region $\mathcal{T} = [\tau_1, \tau_2] \subset (0, \infty)$. To this end we attempt to minimize the difference between model simulations and observations of time-domain data as in the previous sections. In our formulation, the observations, $\hat{E}_j$, are of the electric field E at discrete times t_j taken at $z = 0$. Each simulation is a solution of Maxwell's equation given in (4.6) with (4.3) using candidate values for the distribution of relaxation parameters. We assume a standard least-squares criterion (which is equivalent to a maximum likelihood estimation in many situations–see [DG95]) for the optimization procedure given by

$$J(F) = \sum_j |E(t_j, 0; F) - \hat{E}_j|^2 \tag{4.7}$$

where $E(\cdot, \cdot; F)$ is the solution of (4.6) with (4.3) corresponding to the distribution F. Thus the inverse problem is to solve

$$\min_{F \in \mathcal{P}(\mathcal{T})} J(F). \tag{4.8}$$

In practice, one may choose to approximate a continuous distribution F by a discrete one with, for example, N elements. This approach would result in a straightforward N-dimensional minimization problem. Other parameterizations of the unknown distribution are also possible to reduce the problem to a finite dimensional one.

4.3 Well-Posedness

In this section we address the questions of well-posedness of the form of Maxwell's equation given in (4.6) with respect to the unknown distribution of dielectric parameters. In particular we wish to establish the continuous dependence of solutions on the distributions F in the sense of the Prohorov metric. This leads in turn to well-posedness for the inverse problem (4.8).

We will make use of the following result proved in [BBL00]:

Theorem 1 *Suppose that $\mathcal{J} \in H^1(0, T; V^*)$, γ, $\beta \in L^\infty(0, 1)$, $\alpha \in L^\infty(0, T; L^\infty(0, 1))$ with α, β, γ vanishing outside Ω. Then for $\Phi \in V = H^1_R(0, 1) = \{\phi \in H^1(0, 1) : \phi(1) = 0\}$, $\Psi \in H = L^2(0, 1)$, we have that solutions to* (4.6) *and* (4.3) *exist and are unique. These solutions satisfy $E \in L^2(0, T; V) \cap C(0, T; H)$, $\dot{E} \in L^2(0, T; H)$, and $\ddot{E} \in L^2(0, T; V^*)$.*

Moreover, $t \to E(t,0)$ is absolutely continuous with $\dot{E}(\cdot, 0 \in L^2(0,T)$. The solutions depend continuously on $(\Phi, \Psi, \mathcal{J})$ as maps from $V \times H \times H^1(0,T;V^*)$ to $L^2(0,T;V) \times L^2(0,T;H)$.

Given that we assume g, $\dot{g}$, and $\ddot{g}$ are uniformly continuous in τ and bounded on $([0,T] \times [0,1] \times [\tau_1, \tau_2])$ where $0 < \tau_1 < \tau_2 < \infty$, then $\mathcal{G}$, $\dot{\mathcal{G}}$, and $\ddot{\mathcal{G}}$ are L^∞ since, for example,

$$|\mathcal{G}|_\infty \leq \int_{\mathcal{T}} |g(\cdot, \cdot; \tau)|_\infty dF(\tau) \leq M_\infty$$

when $\mathcal{T} \subset (0, \infty)$. Therefore, α, β, and γ are all also L^∞ by definition. Thus, for each fixed $F \in \mathcal{P}(\mathcal{T})$, α, β, and γ satisfy the hypothesis of Theorem 1, so that given $\Phi \in V = H^1_R(0,1) = \{\phi \in H^1(0,1) : \phi(1) = 0\}$, $\Psi \in H = L^2(0,1)$, a unique solution to (4.6) with (4.3) exists, and $E \in L^2(0,T;V)$, $\dot{E} \in L^2(0,T;H)$.

It remains yet to show the continuous dependence of solutions on F. To this end we introduce a topology on the probability distribution functions $P \in \mathcal{P}(\mathcal{T})$, namely, the Prohorov metric [BB01, BBPP03, BP04, B68]. For the sake of completeness we will give some of the basic definitions and major results here.

Suppose that (Q,d) is a complete metric space, then for any closed subset $G \subset Q$ and $\varepsilon > 0$ we define the set

$$G^\varepsilon = \{q \in Q : d(\tilde{q}, q) < \varepsilon, \quad \forall \tilde{q} \in G\}.$$

Definition 1 *The Prohorov metric $\rho : \mathcal{P}(Q) \times \mathcal{P}(Q) \to \mathbb{R}^+$ is defined by*

$$\rho(F_1, F_2) \equiv \inf\{\varepsilon > 0 : F_1[G] \leq F_2[G^\varepsilon] + \varepsilon, G \text{ closed }, G \subset Q\}.$$

Some useful results on the Prohorov metric are given in the following Lemma (see [B68] for details and proofs):

Lemma 1 *If (Q,d) is a complete metric space, $\mathcal{P}(\mathcal{T})$ is the set of all PDFs on the Borel subsets of the admissible region $\mathcal{T} = [\tau_1, \tau_2] \subset (0, \infty)$, and ρ is defined as above, then $(\mathcal{P}(Q), \rho)$ is a complete metric space. Further, if Q is compact, then $(\mathcal{P}(Q), \rho)$ is a compact metric space.*

The properties of the Prohorov metric which are most relevant to the task of showing our continuous dependence are given in the following theorem ([B68])

Theorem 2 *Given $F_n, F \in \mathcal{P}(Q)$, the following convergence statements are equivalent*

(a) $\rho(F_n, F) \to 0$,

(b) $\int_Q f dF_n(q) \to \int_Q f dF(q)$ *for all bounded, uniformly continuous functions* $f : Q \to \mathbb{R}$,

(c) $F_n[A] \to F[A]$ *for all Borel sets* $A \subset Q$ *with* $F[\partial A] = 0$.

Now we may proceed to show that weak solutions to (4.6) with (4.3) depend continuously on the probability distribution function F in the Prohorov metric.

Theorem 3 *Given that the hypotheses of Theorem 1 are all satisfied, then if* $F_n \to F$ *in the Prohorov metric we have that* $E_n \to E$ *in* $L^2(0,T;V)$ *and* $\dot{E}_n \to \dot{E}$ *in* $L^2(0,T;H)$ *where* E_n *are the weak solutions of* (4.6) *and* (4.3) *corresponding with the probability density functions* F_n*, and* E *is the weak solution of* (4.6) *and* (4.3) *corresponding with the probability function* F.

Proof First we note that $F_n \to F$ in the Prohorov sense is equivalent to

$$\int_{\mathcal{T}} f(\tau) dF_n(\tau) \to \int_{\mathcal{T}} f(\tau) dF(\tau)$$

for all bounded, uniformly continuous functions $f : \mathcal{T} \to \mathbb{R}$. Since $\ddot{g}$ is uniformly continuous in τ, we have then that $\alpha(t,z;F_n) \to \alpha(t,z;F)$ a.e. when $F_n \to F$. We will define $\alpha_n := \alpha(t,z;F_n)$ and $\alpha := \alpha(t,z;F)$. Because $|\alpha_n|_{L^\infty} \leq M$ for all n, the Dominated Convergence Theorem implies that $\alpha_n \to \alpha$ in $L^2([0,T] \times [0,1])$. Similarly, we can show that $\beta_n \to \beta$ and $\gamma_n \to \gamma$ in L^2.

We consider arguments for fixed β and γ. We need to show that $(E^n, \dot{E}^n) \to (E, \dot{E})$ in $L^2([0,T],V) \times L^2([0,T],H)$ when $\alpha_n \to \alpha$, where E^n denotes the solution to (4.6) corresponding to α_n.

We begin by subtracting equation (4.6) corresponding to α from (4.6) corresponding to α_n to obtain

$$\langle \ddot{E}^n - \ddot{E}, \phi \rangle + \langle \gamma(\dot{E}^n - \dot{E}), \phi \rangle + \langle \beta(E^n - E), \phi \rangle + \langle c^2((E^n)' - E'), \phi' \rangle$$
$$+ c\left[\dot{E}^n(t,0) - \dot{E}(t,0)\right]\phi(0) = -\langle \int_0^t \left[\alpha_n(t-s,z)E^n(s,z) - \alpha(t-s,z)E(s,z)\right] ds, \phi \rangle.$$

By adding and subtracting a mixed term to the right side, we have

$$\langle \ddot{E}^n - \ddot{E}, \phi\rangle + \langle \gamma(\dot{E}^n - \dot{E}), \phi\rangle + \langle \beta(E^n - E), \phi\rangle + \langle c^2((E^n)' - E'), \phi'\rangle$$
$$+ c\left[\dot{E}^n(t,0) - \dot{E}(t,0)\right]\phi(0) = -\langle \int_0^t \alpha_n(E^n - E)ds, \phi\rangle - \langle \int_0^t (\alpha_n - \alpha)Eds, \phi\rangle. \quad (4.9)$$

Following the general procedure in [BBL00] (see also [L71], [W92] for related fundamental ideas and theory), we approximate E^n and E in V_m=span$\{w_1, ..., w_m\}$ by

$$E_m^n(t,z) = \sum_{i=1}^m e_i^n(t)w_i(z)$$
$$E_m(t,z) = \sum_{i=1}^m e_i(t)w_i(z).$$

Then (4.9) becomes

$$\langle \ddot{E}_m^n - \ddot{E}_m, \phi\rangle + \langle \gamma(\dot{E}_m^n - \dot{E}_m), \phi\rangle + \langle \beta(E_m^n - E_m), \phi\rangle + \langle c^2(E_m^{n'} - E_m'), \phi'\rangle$$
$$+ c\left[\dot{E}_m^n(t,0) - \dot{E}_m(t,0)\right]\phi(0) = -\langle \int_0^t \alpha_n(E_m^n - E_m)ds, \phi\rangle - \langle \int_0^t (\alpha_n - \alpha)E_m ds, \phi\rangle,$$

which must hold for all $\phi \in V_m$. Since $\dot{E}_m^n$ and $\dot{E}_m$ are both in V_m, we may take $\phi = \dot{E}_m^n - \dot{E}_m$. Then we have

$$\frac{1}{2}\frac{d}{dt}\left[|\dot{E}_m^n - \dot{E}_m|_H^2 + \sigma_1(E_m^n - E_m, E_m^n - E_m)\right] + |\sqrt{\gamma}(\dot{E}_m^n - \dot{E}_m)|_H^2 + c|\dot{E}_m^n(t,0) - \dot{E}_m(t,0)|^2$$
$$= \langle k(E_m^n - E_m), \dot{E}_m^n - \dot{E}_m\rangle - \langle \int_0^t \alpha_n(E_m^n - E_m)ds, \dot{E}_m^n - \dot{E}_m\rangle - \langle \int_0^t (\alpha_n - \alpha)E_m ds, \dot{E}_m^n - \dot{E}_m\rangle,$$

where we have used the sesquilinear form $\sigma_1 : V \times V \to \mathbb{C}$ defined by

$$\sigma_1(\phi, \psi) = \langle c^2\phi', \psi'\rangle_H + \langle \hat{\beta}\phi, \psi\rangle_H$$

for ϕ,$\psi \in V$ and where $\hat{\beta} = \beta + k > 0$ for some sufficiently large $k > 0$.

Integration, along with the V-ellipticity of σ_1 yields

$$|\dot{E}_m^n(t) - \dot{E}_m(t)|_H^2 + c_1|E_m^n(t) - E_m(t)|_V^2 + 2\int_0^t |\sqrt{\gamma}(\dot{E}_m^n(s) - \dot{E}_m(s))|_H^2 ds$$
$$+ 2c|\dot{E}_m^n(t,0) - \dot{E}_m(t,0)|_{L^2(0,t)}^2 \le 2\left|\int_0^t F_m^n(\xi)d\xi\right|, \quad (4.10)$$

where

$$F_m^n(\xi) = \langle k[E_m^n(\xi) - E_m(\xi)], \dot{E}_m^n(\xi) - \dot{E}_m(\xi)\rangle - \langle \int_0^\xi \alpha_n[E_m^n(s) - E_m(s)]ds, \dot{E}_m^n(\xi) - \dot{E}_m(\xi)\rangle$$
$$- \langle \int_0^\xi [\alpha_n - \alpha]E_m(s)ds, \dot{E}_m^n(\xi) - \dot{E}_m(\xi)\rangle$$
$$= T_2(\xi) + T_3(\xi) + T_4(\xi).$$

Following precisely the arguments in [BBL00] we have that

$$\int_0^t |T_2(\xi)|d\xi \le \int_0^t \left[\frac{1}{2}k^2|E_m^n(\xi) - E_m(\xi)|_H^2 + \frac{1}{2}|\dot{E}_m^n(\xi) - \dot{E}_m(\xi)|_H^2\right] d\xi$$

and

$$\int_0^t |T_3(\xi)|d\xi \le K_1 \int_0^t |E_m^n(\xi) - E_m(\xi)|_H^2 d\xi + K_2 \int_0^t |\dot{E}_m^n(\xi) - \dot{E}_m(\xi)|_H^2 d\xi.$$

Lastly, we bound the final term by

$$|T_4(\xi)| = \langle \int_0^\xi [\alpha_n(\xi - s) - \alpha(\xi - s)]\, E_m(s)ds, \dot{E}_m^n(\xi) - \dot{E}_m(\xi)\rangle$$
$$\le \frac{1}{2}\left|\int_0^\xi [\alpha_n(\xi - s) - \alpha(\xi - s)]\, E_m(s)ds\right|_H^2 + \frac{1}{2}|\dot{E}_m^n(\xi) - \dot{E}_m(\xi)|_H^2.$$

Since E_m is bounded in $C([0,T],V)$,

$$|T_4(\xi)| \le \frac{1}{2}\left(\int_0^\xi K_E|\alpha_n(\xi - s) - \alpha(\xi - s)|_H ds\right)^2 + \frac{1}{2}|\dot{E}_m^n(\xi) - \dot{E}_m(\xi)|_H^2$$
$$\le \frac{1}{2}K_E^2 t\int_0^\xi |\alpha_n(\xi - s) - \alpha(\xi - s)|_H^2 ds + \frac{1}{2}|\dot{E}_m^n(\xi) - \dot{E}_m(\xi)|_H^2.$$

Thus

$$\int_0^t |T_4(\xi)|d\xi \le \hat{K_3}\int_0^t \int_0^\xi |\alpha_n(\xi - s) - \alpha(\xi - s)|_H^2 dsd\xi + K_4 \int_0^t |\dot{E}_m^n(\xi) - \dot{E}_m(\xi)|_H^2 d\xi.$$

We observe that

$$\int_0^t \int_0^\xi f(\xi - s)dsd\xi = \int_0^t \int_0^{t-u} f(u)dsdu$$
$$= \int_0^t f(u)(t - u)du$$
$$\le C\int_0^t f(u)du \qquad \text{for } t, u \in [0,T].$$

Therefore

$$\int_0^t |T_4(\xi)|d\xi \le K_3 \int_0^t |\alpha_n(u) - \alpha(u)|_H^2 du + K_4 \int_0^t |\dot{E}_m^n(\xi) - \dot{E}_m(\xi)|_H^2 d\xi.$$

Using the above bounds, we find that (4.10) becomes

$$|\dot{E}_m^n(t) - \dot{E}_m(t)|_H^2 + c_1|E_m^n(t) - E_m(t)|_V^2$$

$$+ 2\int_0^t |\sqrt{\gamma}(\dot{E}_m^n(s) - \dot{E}_m(s))|_H^2 ds + 2c|\dot{E}_m^n(\cdot,0) - \dot{E}_m(\cdot,0)|_{L^2(0,t)}^2$$

$$\leq C_1 \int_0^t |E_m^n(s) - E_m(s)|_H^2 ds + C_2 \int_0^t |\dot{E}_m^n(s) - \dot{E}_m(s)|_H^2 ds$$

$$+ C_3 \int_0^t |\alpha_n(s) - \alpha(s)|_H^2 ds. \quad (4.11)$$

Noting that $|\cdot|_H \leq \mu|\cdot|_V$ for some constant μ and letting

$$\kappa_n := \int_0^T |\alpha_n(s) - \alpha(s)|_H^2 ds = |\alpha_n - \alpha|_{L^2([0,T],H)}^2 \quad ,$$

we then have that (4.11) implies

$$|\dot{E}_m^n(t) - \dot{E}_m(t)|_H^2 + |E_m^n(t) - E_m(t)|_V^2$$

$$\leq \nu\kappa_n + \nu \int_0^t \left[|E_m^n(s) - E_m(s)|_V^2 + |\dot{E}_m^n(s) - \dot{E}_m(s)|_H^2\right] ds$$

for some $\nu > 0$ independent of m and n. Using Gronwall's Inequality we have

$$|\dot{E}_m^n(t) - \dot{E}_m(t)|_H^2 + |E_m^n(t) - E_m(t)|_V^2 \leq \nu\kappa_n e^{\nu T} \qquad \text{for } t \in [0,T]. \quad (4.12)$$

From Theorem 1 we have that for each fixed n, $E_m^n \rightharpoonup E^n$ in $L^2([0,T],V)$. Therefore using weak lower semicontinuity of norms we have

$$|E^n - E|_{L^2([0,T],V)}^2 \leq \liminf_m |E_m^n - E_m|_{L^2([0,T],V)}^2 \quad ,$$

with a similar estimate holding for $\dot{E}^n - \dot{E}$ in the $L^2([0,T],H)$ norm. We may apply these results to the integral of (4.12) from 0 to T to finally obtain

$$|\dot{E}^n - \dot{E}|_{L^2([0,T],H)}^2 + |E^n - E|_{L^2([0,T],V)}^2 \leq \nu\kappa_n T e^{\nu T}.$$

Since $\alpha_n \to \alpha$ in L^2, then by definition $\kappa_n \to 0$ as $n \to \infty$, which in turn implies $|\dot{E}^n - \dot{E}|_{L^2([0,T],H)}^2 \to 0$ and $|E^n - E|_{L^2([0,T],V)}^2 \to 0$. This gives continuous dependence of $(E, \dot{E})$ on α. Similar arguments can be used to show that $(E, \dot{E})$ depend continuously on γ

and β as well. Thus we have that solutions of (4.6) with (4.3) depend continuously on the probability measure F in the sense that the map

$$F \to (E, \dot{E})$$

is continuous from $\mathcal{P}(\mathcal{T})$ to $L^2([0,T],V) \times L^2([0,T],H)$.

□

This result further yields that $F \to J(F) = \sum_j |E(t_j, 0; F) - \hat{E}_j|^2$ is continuous from $\mathcal{P}(\mathcal{T})$ to $\mathbb{R}^1$, where $\mathcal{P}(\mathcal{T})$, with the Prohorov metric, is compact for $\mathcal{T}$ compact by Lemma 1. Continuity of this map, along with compactness of $\mathcal{P}(\mathcal{T})$ in the ρ metric, is sufficient to establish existence of a solution to the inverse problem (4.8). Then the general theory of Banks-Bihari in [BB01] as outlined in [BBPP03, BP04], and summarized below, can be employed to obtain stability for the inverse problem, as well as an approximation theory which can be used as a basis for a computational methodology.

4.4 Stability of the Inverse Problem

Recall our inverse problem

$$\min_{F \in \mathcal{P}(\mathcal{T})} J(F, \hat{E}) = \sum_{j=1}^{N} |E(t_j, 0; F) - \hat{E}_j|^2 \tag{4.13}$$

where $E(\cdot, \cdot; F)$ is the solution of (4.6) with (4.3) corresponding to the distribution F, and $\hat{E}_j$ represents observations of the electric field at $z = 0$ and times t_j. Given data $\hat{E}^k \in \mathbb{R}^N$ and $\hat{E} \in \mathbb{R}^N$ such that $\hat{E}^k \to \hat{E}$ as $k \to \infty$, and corresponding solutions $F^*(\hat{E}^k)$ and $F^*(\hat{E})$, we say that the inverse problem (4.13) is *continuously dependent on the data* (or *stable*) if $dist(F^*(\hat{E}^k), F^*(\hat{E})) \to 0$ (see [BK89, BSW96]). Here *dist* represents the usual Hausdorff distances between sets (as solutions to the inverse problem are not necessarily unique), given by $dist(A, B) := \inf\{\rho(F_1, F_2) : F_1 \in A, F_2 \in B\}$, for sets A and B.

We note that $\mathcal{P}(\mathcal{T})$ with the ρ metric is in general an infinite dimensional space, thus we must consider approximation techniques to address computional concerns. We will make use of the following density theorem proved in [BB01].

Theorem 4 *Let Q be a complete, separable metric spcae with metric d, $\mathbb{S}$ be the class of all Borel subsets of Q and $\mathcal{P}(Q)$ be the space of probability measures on $(Q, \mathbb{S})$. Let $Q_0 = \{q_i\}_{i=1}^{\infty}$ be a countable, dense subset of Q, and define Δ_{q_i} to be a distribution, corresponding to the density δ_{q_i}, with atom at q_i. Then the set of $P \in \mathcal{P}(Q)$ such that P has finite support in Q_0, and rational masses, is dense in $\mathcal{P}(Q)$ in the ρ metric. That is,*

$$P_0(Q) := \left\{ F \in \mathcal{P}(Q) : F = \sum_{i=1}^{k} p_i \Delta_{q_i}, k \in \mathbb{N}^+, q_i \in Q_0, p_i \in \mathfrak{R}, p_i \geq 0, \sum_{i=1}^{k} p_i = 1 \right\} \quad (4.14)$$

is dense in $\mathcal{P}(Q)$ relative to ρ (note that $\mathfrak{R}$ denotes the rational numbers).

Theorem 4 provides a mechanism for constructing approximate solution sets to be used in tractable computational methods for the inverse problem (4.13). First we define the space

$$Q_d := \bigcup_{M=1}^{\infty} Q_M \quad (4.15)$$

where $Q_M := \{q_i^M\}_{i=1}^{M}$, $M = 1, 2, \ldots$, are chosen so that Q_d is dense in Q. Note that Q_d is countable. Then for each positive integer M define

$$\mathcal{P}^M(Q) := \left\{ F \in \mathcal{P}(Q) : F = \sum_{i=1}^{M} p_i \Delta_{q_i^M}, q_i^M \in Q_M, p_i \in \mathfrak{R}, p_i \geq 0, \sum_{i=1}^{k} p_i = 1 \right\}. \quad (4.16)$$

If we let

$$P_d(Q) := \bigcup_{M=1}^{\infty} \mathcal{P}^M(Q), \quad (4.17)$$

then by Theorem 4 we have that $P_d(Q)$ is dense in $\mathcal{P}(Q)$. Now we may approximate any $F \in \mathcal{P}(Q)$ by a sequence $\{F_{M_\ell}\}$, with $F_{M_\ell} \in \mathcal{P}^{M_\ell}(Q)$, such that $\rho(F_{M_\ell}, F) \to 0$ as $M_\ell \to \infty$.

We may also construct a sequence of approximate problems as follows: for each positive integer M find the solution to

$$\min_{F_M \in \mathcal{P}^M(\mathcal{T})} J(F_M, \hat{E}) = \sum_{j=1}^{N} |E(t_j, 0; F_M) - \hat{E}_j|^2. \quad (4.18)$$

Let $F_M^*(\hat{E})$ denote the solution set to the problem corresponding to data $\hat{E}$. These problems are said to be *method stable* (again, see [BK89, BSW96]) if for any data $\hat{E}_k$ and $\hat{E}$ such that $\hat{E}_k \to \hat{E}$ as $k \to \infty$ we have that $dist(F_M^*(\hat{E}_k), F^*(\hat{E})) \to 0$ as $k \to \infty$ and $M \to \infty$.

The following theorem, proved in [BB01], gives the main result on the stability of the inverse problem in (4.13)

Theorem 5 *Let Q be a compact metric space and assume solutions $E(\cdot,\cdot;F)$ of* (4.6) *with* (4.3) *are continuous in F on $\mathcal{P}(Q)$, the set of all probability measures on Q. Let Q_d be a countable, dense subset of Q as defined in* (4.15) *with $Q_M := \{q_i^M\}_{i=1}^M$, and let $P_d(Q)$ be a dense subset of $\mathcal{P}(Q)$ as defined in* (4.17) *with $P^M(Q)$ as defined in* (4.16). *Suppose $F_M^*(\hat{E}_k)$ is the set of minimizers for $J(F_M)$ over $F_M \in P^M(Q)$ corresponding to the data $\{\hat{E}_k\}$, and $F^*(\hat{E})$ is the set of minimizers for $J(F)$ over $F \in P(Q)$ corresponding to the data $\{\hat{E}\}$, where $\{\hat{E}_k\}$, $\{\hat{E}\} \in \mathbb{R}^N$ are the observed data such that $\hat{E}_k \to \hat{E}$ as $k \to \infty$. Then $dist(F_M^*(\hat{E}_k), F^*(\hat{E})) \to 0$ as $k \to \infty$ and $M \to \infty$. Thus the solutions depend continuously on the data (are* stable*). Further the approximate problems are* method stable.

Using these results we may describe a computational methodology which approximates the solution to the inverse problem (4.13). In particular, any element of $\mathcal{P}(Q)$ may be approximated arbitrarily closely (in the Prohorov metric) by a finite linear combinations of Dirac measures. If Q_d, $\mathcal{P}^M(Q)$, and $\mathcal{P}_d(Q)$ are defined as above, then for M sufficiently large, we can approximate the inverse problem for $J(F)$ by the inverse problem for

$$J^M(\bar{p}) = \sum_{j=1}^{N} |E(t_j, 0; F_M) - \hat{E}_j|^2, \tag{4.19}$$

where $\bar{p} = \{p_i\}_{i=1}^M$ and $F_M = \sum_{i=1}^M p_i \Delta_{q_i^M}$, with $p_i \in \mathfrak{R}$, $p_i \geq 0$ and $\sum_{i=1}^k p_i = 1$. Thus we have an M dimensional optimization problem

$$\min_{\bar{p} \in \mathbb{R}^M} J^M(\bar{p}). \tag{4.20}$$

However, as explained in [BP04], for some problems it is more natural to minimize $J(F)$ over a subset of $\mathcal{P}(Q)$ consisting of only absolutely continuous probability densities, i.e., those that have continuous densities f such that $Prob[a,b] = \int_a^b f(x)dx$. With this in mind, we will make use of the following theorem proven in [BP04]

Theorem 6 *Let $\mathcal{F}$ be a weakly compact subset of $L^2(Q)$, with Q compact, and let $\mathcal{P}_{\mathcal{F}}(Q)$ be the family of probability functions on Q generated by $\mathcal{F}$ as a set of densities*

$$\mathcal{P}_{\mathcal{F}}(Q) := \{F \in \mathcal{P}(Q) : F = \int f, f \in \mathcal{F}\}. \tag{4.21}$$

Then $\mathcal{P}_{\mathcal{F}}(Q)$ is a ρ compact subset of $(\mathcal{P}(Q), Q)$, where ρ is the Prohorov metric.

This result, combined with the continuous depence of the map $F \to J(F)$ guarantees the existence of a solution in $\mathcal{P}_{\mathcal{F}}(Q) \subset \mathcal{P}(Q)$. We may now approximate functions $f \in \mathcal{F}$ with smooth functions, such as linear splines. For example, since $\mathcal{F} \in L^2(Q)$ we can define

$$f^K(\tau) = \sum_{k=0}^{K} b_k^K \ell_k^K(\tau), \tag{4.22}$$

(where ℓ_k^K's are the usual piecewise linear splines and the b_k^K's are rational numbers), such that $f^K \to f$ in $L^2(Q)$. This implies that

$$\int_Q g f^K d\tau \to \int_Q g f d\tau$$

for all $g \in L^2(Q)$, hence for all $g \in C(Q)$, which yields

$$\rho(F^K, F) \to 0$$

where $F^K = \int_Q f^K$ and $F = \int_Q f$. If we let $\mathcal{F}^K := \{h \in L^2(Q) : h(\tau) = \sum_{k=0}^{K} b_k^K \ell_k^K(\tau)\}$ then we have that the set

$$\tilde{\mathcal{P}}(Q) := \left\{ F \in \mathcal{P}(Q) : F = \int_Q f d\tau, f \in \bigcup_{K=1}^{\infty} \mathcal{F}^K \right\}$$

is dense in $\mathcal{P}_{\mathcal{F}}(Q)$ in the ρ-metric. Therefore piecewise linear splines provides an alternative to using Dirac measures to approximate the densities of absolutely continuous probability distribution candidates in an inverse problem formulation.

4.5 Conclusion

We have presented theoretical results on a model for the electric field with multiple electric polarization mechanisms in a dielectric material. This provides a firm foundation

for an inverse problem formulation to determine an unknown probability distribution of parameters which describe the dielectric properties of the material. To this end, we have proven the continuous dependence of the solutions with respect to the unknown distributions in the Prohorov metric. This argument, combined with previous results on existence and uniqueness in Maxwell systems, demonstrate the well-posedness of the model. Moreover, we have shown that the theory described in [BB01, BBPP03, BP04] can be combined with our results here to provide existence, stability, and an approximation theory for the associated inverse problems.

Chapter 5

Multiple Debye Polarization Inverse Problems

In this section we attempt to demonstrate the feasibility of an inverse problem for a distribution of dielectric parameters. We start in Section 5.1 with an example in which we assume a discrete distribution with two atoms. In a manner similar to our inverse problem for gap detection above, we generate data by simulating our model assuming fixed proportions of polarization contribution involving two fixed relaxation times in a Debye polarization equation, and then attempt to recover these relaxation times using a least squares inverse problem formulation. Next we assume the relaxation times are known, but the relative volume proportions of each material is unknown. Numerical results are given for this inverse problem, as well as the inverse problem where neither the relaxation times, nor the volume proportions, are known. Lastly, we assume a uniform distribution of relaxation times and attempt to resolve the endpoints of this distribution.

5.1 Relaxation Time Inverse Problem

As above, we decompose the electric polarization into two components, each dependent on distinct relaxation times as follows:

$$P = \alpha_1 P_1(\tau_1) + \alpha_2 P_2(\tau_2), \tag{5.1}$$

where each P_i satisfies a Debye polarization equation with parameter τ_i. For now we assume the proportions α_1 and $\alpha_2 = 1-\alpha_1$ are known. Thus we are attempting to solve the following least squares optimization problem:

$$\min_{(\tau_1,\tau_2)} \sum_j |E(t_j, 0; (\tau_1, \tau_2)) - \hat{E}_j|^2 \tag{5.2}$$

where $\hat{E}_j$ is data generated using (τ_1, τ_2) in our simulator, and $E(t_j, 0; (\tau_1, \tau_2))$ depends on each τ_i through its dependence on P, see for example, Equation (4.1). Figures 5.1 and 5.2 depict an example of the objective function and the log of the objective function respectively, both plotted versus the logs of τ_1 and τ_2 (using a frequency of $10^{11}Hz$, $\alpha_1 = \alpha_2 = .5$, $\tau_1^* = 10^{-7.5}$ and $\tau_2^* = 10^{-7.8}$).

5.1.1 Analysis of Objective Function

We can see clearly from the log surface plot in Figure 5.2 that simulations corresponding to relaxation times satisfying a certain relation more closely match the data than those off of this "best fit curve". Note that the appearance of many local minima is due to the steep decent near the "best fit curve" since the lattice points of the mesh used do not always lie on the line. However, the exact solution of $\log(\tau_1) = -7.5$ and $\log(\tau_2) = -7.8$ is evident. If we trace along this curve, as displayed in Figure 5.3, we see that there are actually two global minima, the exact solution mentioned above, and since the proportion used in this case was $\alpha_1 = \alpha_2 = .5$, we also have the symmetric solution where τ_1 and τ_2 are swapped. Unfortunately, the scale of the plot shows that the difference between the objective function at the minimizers and any other point on this curve in our parameter space is less than 4×10^{-10}. Therefore the minimizing parameters are not likely to be identifiable in a practical, experimental setting.

The equation for this "best fit curve" can be derived by examining equation (3.10). For large frequencies, the term given by $\tilde{\lambda}\epsilon_d\langle I_\Omega \dot{E}, \phi\rangle$ dominates. We can see this by consid-

ering the frequency domain where the time derivative causes an increase by a factor of ω. Thus the equation for the "curve of best fit" is simply that of constant a $\tilde{\lambda}$, in particular

$$\frac{\alpha_1}{c\tau_1} + \frac{\alpha_2}{c\tau_2} = \frac{\alpha_1}{c\tau_1^*} + \frac{\alpha_2}{c\tau_2^*}. \tag{5.3}$$

This is precisely the curve that is plotted above the surface in Figure 5.2.

The frequency dependence of the term suggests that for smaller frequencies it may not be the dominant contributor, and therefore, there may be a fundamentally different structure to the surface plot. This is in fact what we observe in our simulations. Figures 5.4 through 5.7 display the surface plots and the log surface plots for frequencies of $10^9 Hz$ and $10^6 Hz$. Note that in the latter case the concavity of the "curve of best fit" has swapped orientation!

Through our numerical calculations we have determined that for the case using a frequency of $10^6 Hz$ the "curve of best fit" is instead that of constant $\tilde{\tau} := \alpha_1\tau_1 + \alpha_2\tau_2$. For the example given here, $\tilde{\tau} \approx 2.37000 \times 10^{-8}$. In our simulations, frequencies less than one divided by this number were characterized by a constant $\tilde{\tau}$ while larger frequencies resulted in dominance by the $\tilde{\lambda}$ term given above. The fact that the regime characterized by $\omega\tau < 1$ is fundamentally different in many respects from that of the $\omega\tau > 1$ regime is well documented (see, for example, [BB78]). However, the behavior of the objective function for each frequency along its corresponding "curve of best fit" is similar, despite the curves themselves being fundamentally different, as demonstrated by comparing Figure 5.3 to Figure 5.8 which uses a frequency of $10^6 Hz$.

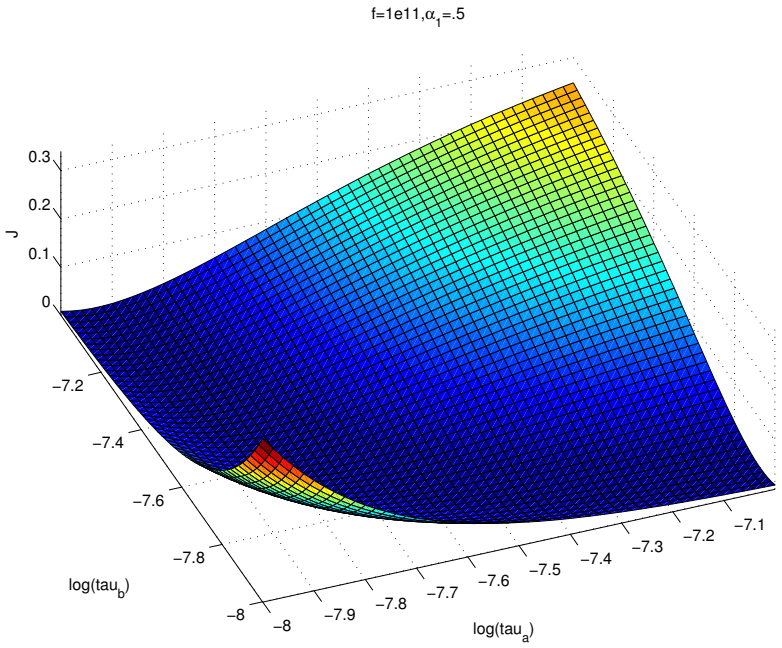

Figure 5.1: The objective function for the relaxation time inverse problem plotted versus the log of τ_1 and the log of τ_2 using a frequency of $10^{11} Hz$.

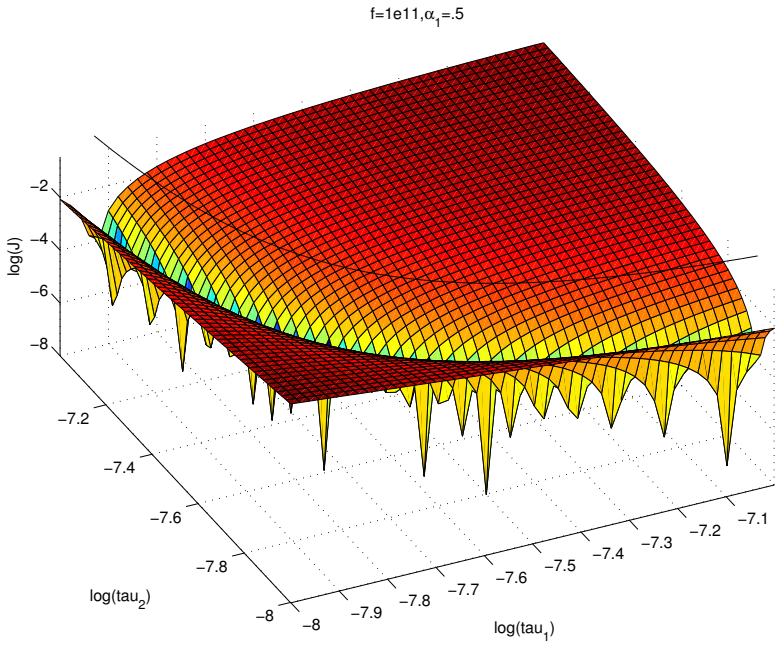

Figure 5.2: The log of the objective function for the relaxation time inverse problem plotted versus the log of τ_1 and the log of τ_2 using a frequency of $10^{11} Hz$. The solid line above the surface represents the curve of constant $\tilde{\lambda}$.

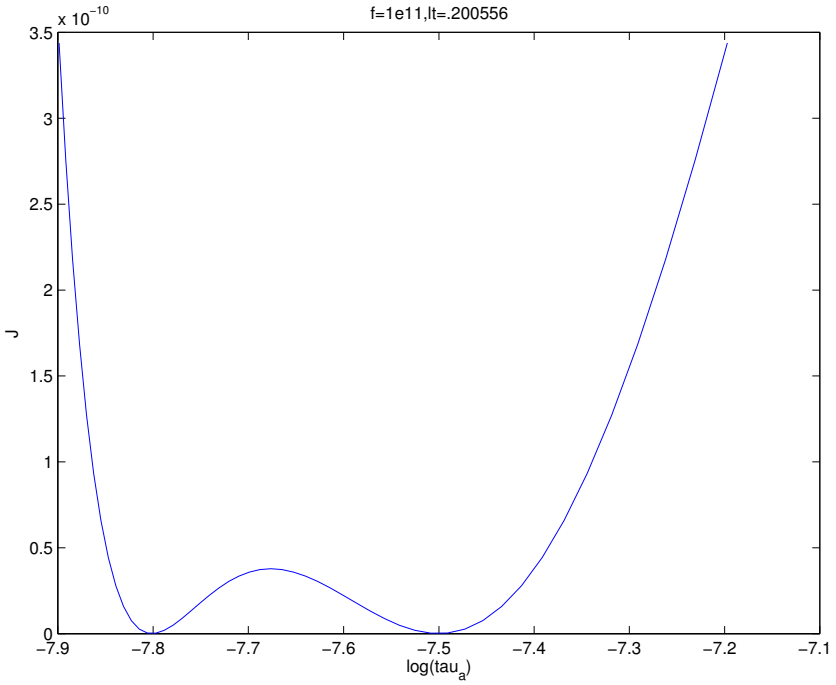

Figure 5.3: The objective function for the relaxation time inverse problem plotted along the curve of constant $\tilde{\lambda}$ using a frequency of $10^{11} Hz$.

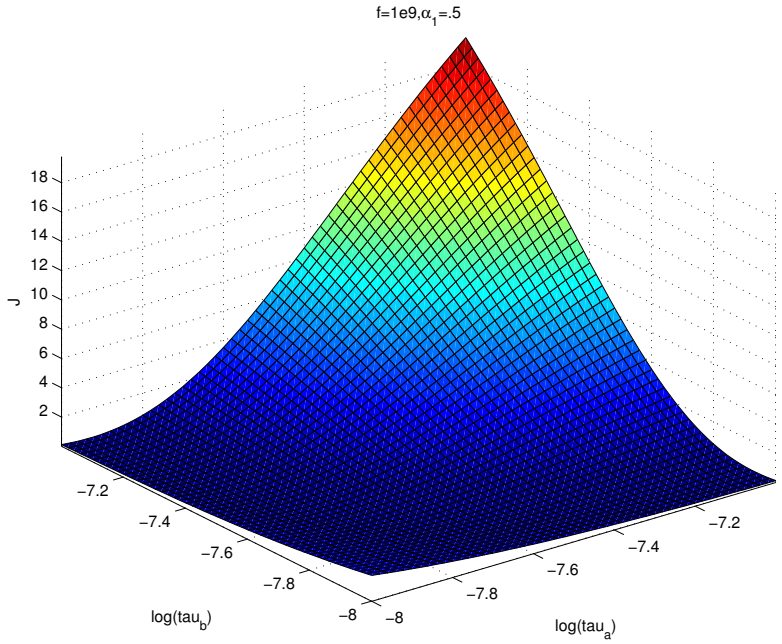

Figure 5.4: The objective function for the relaxation time inverse problem plotted versus the log of τ_1 and the log of τ_2 using a frequency of $10^9 Hz$.

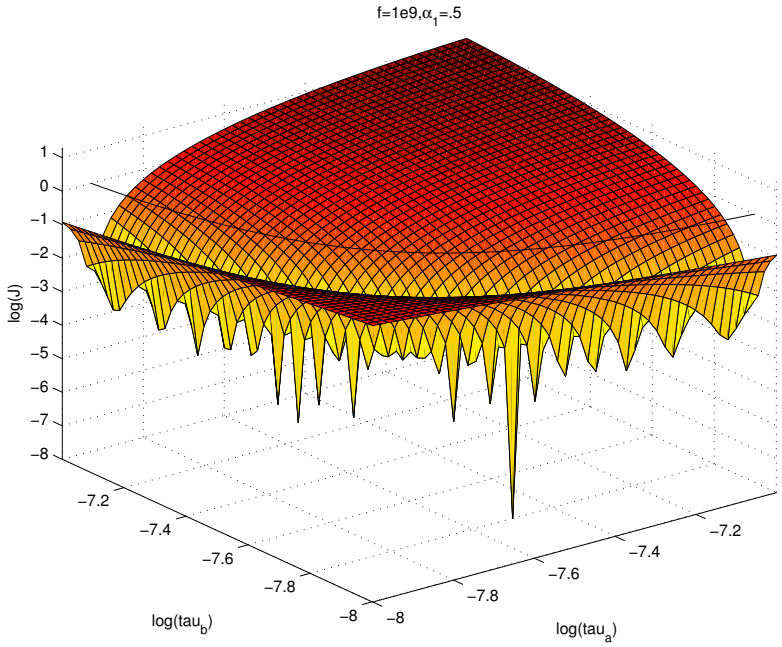

Figure 5.5: The log of the objective function for the relaxation time inverse problem plotted versus the log of τ_1 and the log of τ_2 using a frequency of $10^9 Hz$. The solid line above the surface represents the curve of constant $\tilde{\lambda}$.

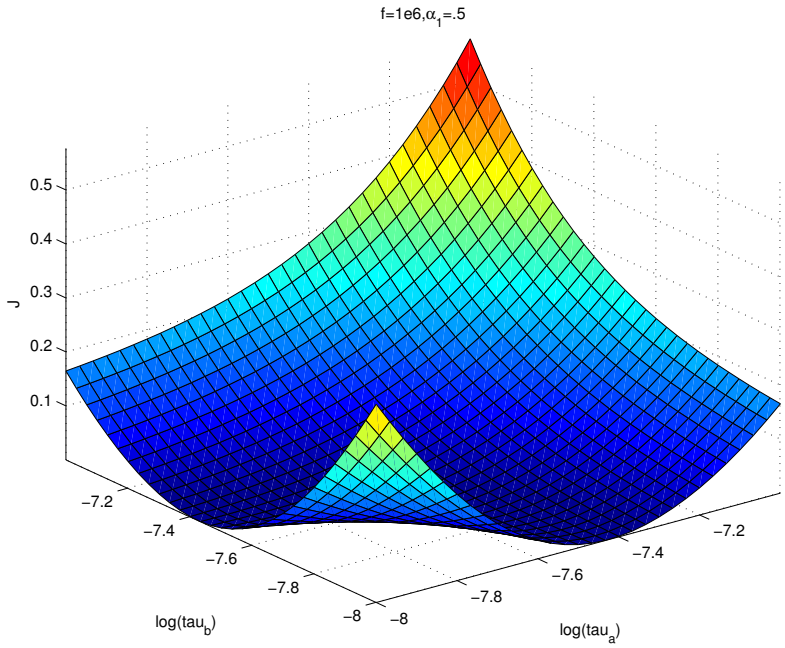

Figure 5.6: The objective function for the relaxation time inverse problem plotted versus the log of τ_1 and the log of τ_2 using a frequency of $10^6 Hz$.

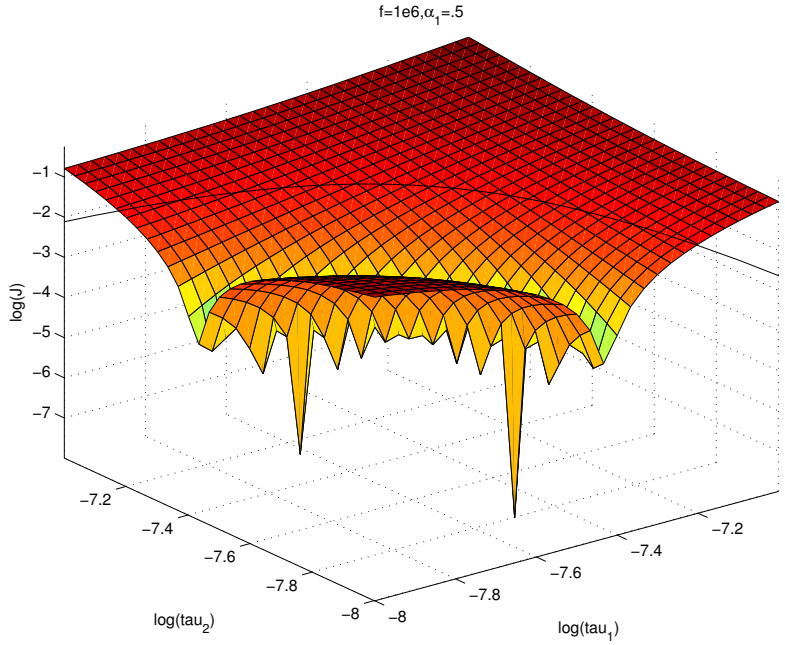

Figure 5.7: The log of the objective function for the relaxation time inverse problem plotted versus the log of τ_1 and the log of τ_2 using a frequency of $10^6 Hz$. The solid line above the surface represents the curve of constant $\tilde{\tau}$.

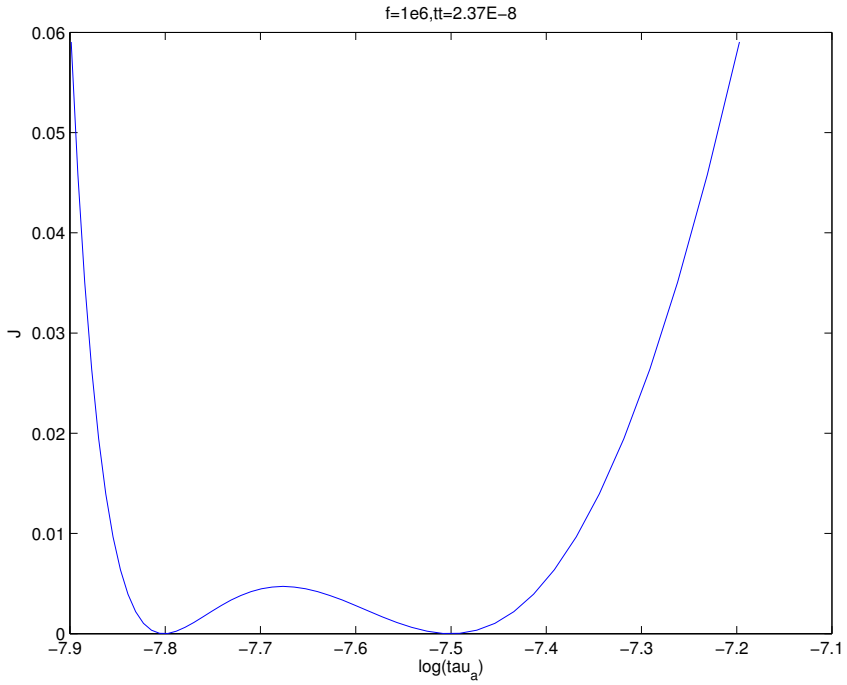

Figure 5.8: The objective function for the relaxation time inverse problem plotted along the curve of constant $\tilde{\tau}$ using a frequency of $10^6 Hz$.

5.1.2 Optimization Procedure and Results

We attempt to apply a two parameter Levenberg-Marquardt optimization routine to the least squares error between the given data and our simulations to try to identify the two distinct relaxation times that generated the data. We are assuming that the corresponding volume proportions of the two materials (α_1 and $\alpha_2 := 1 - \alpha_1$) are known. We consider three different scenarios with respect to the volume proportions: $\alpha_1 \in \{.1, .5, .9\}$. We also perform our inverse problem using the frequencies $10^{11}Hz$, $10^{9}Hz$ and $10^{6}Hz$. Lastly we test the optimization procedure with three various initial conditions given in Table 5.1. The actual values are $\tau_1 = 10^{-7.50031} \approx 3.16 \times 10^{-8}$ and $\tau_2 = 10^{-7.80134} \approx 1.58 \times 10^{-8}$. Note that the first set of initial conditions is the farthest from the exact solution, while the third is the closest.

Table 5.1: Three sets of initial conditions for the relaxation time inverse problem representing $(\tau_1^0, \tau_2^0) = (C\tau_1^*, \tau_2^*/C)$ for $C \in \{5, 2, 1.25\}$ respectively (case 0 represents exact solution), also given are the $\log_{10}$ of each relaxation time, as well as the % relative error from the exact value.

case	τ_1	τ_2	$\log(\tau_1)$	$\log(\tau_2)$	% τ_1	% τ_2
0	3.1600e-8	1.5800e-8	-7.50031	-7.80134	0	0
1	1.5800e-7	3.1600e-9	-6.80134	-8.50031	400	80
2	6.3200e-8	7.9000e-9	-7.19928	-8.10237	100	50
3	3.9500e-8	1.2640e-8	-7.40340	-7.89825	25	20

The results of the optimization are given in Tables 5.2 through 5.7. Most of the cases appear not to have converged. Only a few of the closest initial conditions even came close to resolving the original values of the relaxation times. But if we recall the shape of the objective function that we are trying to minimize (for example see Figures 5.1 and 5.2) then it is understandable how a gradient based method may converge directly to the "curve of best fit". However, due to the difference in scales once it reaches this curve, the optimization routine may not be able to traverse the curve to find the true global minimum. This is in fact what is occurring.

Table 5.8 displays the values of $\tilde{\lambda}$ corresponding to each set of initial conditions, where case 0 denotes the exact solution. Tables 5.10 and 5.11 display the resulting values of $\tilde{\lambda}$ after the Levenberg-Marquardt routine using frequencies $10^{11}Hz$ and $10^{9}Hz$ respectively. Since smaller frequencies are expected to converge to the curve of constant $\tilde{\tau}$, we give the

Table 5.2: Resulting values of τ_1 after the Levenberg-Marquardt routine using a frequency of $10^{11}Hz$ (recall the exact solution τ_1^* =3.1600e-8).

	α_1		
case	.1	.5	.9
1	1.57218e-07	1.7488e-07	2.26538e-07
2	6.34973e-08	9.73445e-08	4.90169e-08
3	3.98062e-08	4.13321e-08	3.43569e-08

Table 5.3: Resulting values of τ_1 after the Levenberg-Marquardt routine using a frequency of $10^{9}Hz$ (recall the exact solution τ_1^* =3.1600e-8).

	α_1		
case	.1	.5	.9
1	1.60128e-07	1.60397e-07	7.0395e-08
2	6.37815e-08	6.68561e-08	3.99819e-08
3	3.97416e-08	4.03239e-08	3.59503e-08

Table 5.4: Resulting values of τ_1 after the Levenberg-Marquardt routine using a frequency of $10^{6}Hz$ (recall the exact solution τ_1^* =3.1600e-8).

	α_1		
case	.1	.5	.9
1	3.79957e-08	3.23393e-08	3.16236e-08
2	3.17753e-08	3.32218e-08	3.21036e-08
3	3.17897e-08	3.19001e-08	3.16068e-08

initial values of $\tilde{\tau}$ as well, in Table 5.9, and Table 5.12 displays the resulting values of $\tilde{\tau}$ after running the Levenberg-Marquardt routine using a frequency of $10^{6}Hz$. Note that while the initial values in case 1 are farthest from the exact solution, some of the corresponding $\tilde{\tau}$ are actually closest to the actual value (for example, $\alpha_1 = .1$). While this suggests that this should more easily converge to the "curve of best fit", it will most likely be farther away from the exact solution on this curve, and therefore is still considered the hardest of the cases to solve.

Recognizing that we have converged to the "curve of best fit" in each of the above cases, we may now restart an optimization routine that traverses this curve. Some modifications to the optimization parameters are required to address the vast difference in scales of this subproblem as compared to the two parameter optimization problem. The final results of this two step optimization approach are given in Tables 5.13 through 5.18. As expected, the results from case 3 are generally better than the other two sets of initial

Table 5.5: Resulting values of τ_2 after the Levenberg-Marquardt routine using a frequency of $10^{11}Hz$ (recall the exact solution τ_2^* =1.5800e-8).

	α_1		
case	.1	.5	.9
1	1.51271e-08	1.1208e-08	3.2429e-09
2	1.53697e-08	1.18119e-08	6.10283e-09
3	1.56197e-08	1.41322e-08	1.1607e-08

Table 5.6: Resulting values of τ_2 after the Levenberg-Marquardt routine using a frequency of $10^{9}Hz$ (recall the exact solution τ_2^* =1.5800e-8).

	α_1		
case	.1	.5	.9
1	1.51255e-08	1.12739e-08	4.54532e-09
2	1.53692e-08	1.25029e-08	8.12599e-09
3	1.56222e-08	1.4257e-08	1.02271e-08

Table 5.7: Resulting values of τ_2 after the Levenberg-Marquardt routine using a frequency of $10^{6}Hz$ (recall the exact solution τ_2^* =1.5800e-8).

	α_1		
case	.1	.5	.9
1	1.51064e-08	1.50634e-08	1.63437e-08
2	1.57826e-08	1.41845e-08	1.12902e-08
3	1.57792e-08	1.55032e-08	1.57796e-08

Table 5.8: The initial values of $\tilde{\lambda} := \frac{\alpha_1}{c\tau_1} + \frac{\alpha_2}{c\tau_2}$ for each set of initial conditions (case 0 represents the exact solution).

case	.1	.5	.9
0	0.200556	0.158333	0.116111
1	0.952112	0.538334	0.124556
2	0.385278	0.237500	0.0897223
3	0.245945	0.174167	0.102389

Table 5.9: The initial values of $\tilde{\tau} := \alpha_1\tau_1 + \alpha_2\tau_2$ for each set of initial conditions (case 0 represents the exact solution).

case	.1	.5	.9
0	1.7380e-08	2.3700e-08	3.0020e-08
1	1.8644e-08	8.0580e-08	1.42516e-07
2	1.3430e-08	3.5550e-08	5.7670e-08
3	1.5326e-08	2.6070e-08	3.6814e-08

Table 5.10: Resulting values of $\tilde{\lambda}$ after the Levenberg-Marquardt routine using a frequency of $10^{11}Hz$ for each set of initial conditions (case 0 represents the exact solution).

	α_1		
case	.1	.5	.9
0	0.200556	0.158333	0.116111
1	0.200573	0.15834	0.116109
2	0.200573	0.158327	0.1159
3	0.200573	0.158363	0.116114

Table 5.11: Resulting values of $\tilde{\lambda}$ after the Levenberg-Marquardt routine using a frequency of $10^{9}Hz$ for each set of initial conditions (case 0 represents the exact solution).

	α_1		
case	.1	.5	.9
0	0.200556	0.158333	0.116111
1	0.200555	0.158331	0.116029
2	0.200556	0.158337	0.116132
3	0.200556	0.158339	0.116119

Table 5.12: Resulting values of $\tilde{\tau}$ after the Levenberg-Marquardt routine using a frequency of $10^{6}Hz$ for each set of initial conditions (case 0 represents the exact solution).

	α_1		
case	.1	.5	.9
0	1.7380e-08	2.3700e-08	3.0020e-08
1	1.73954e-08	2.37014e-08	3.00956e-08
2	1.73819e-08	2.37031e-08	3.00222e-08
3	1.73803e-08	2.37016e-08	3.00241e-08

conditions. The highest frequency attempted, $10^{11}Hz$ seemed to perform the most poorly. This suggests that the higher the frequency, the more difficult to accurately resolve the polarization mechanisms. Although the $10^{6}Hz$ case used the curve of constant $\tilde{\tau}$ while the $10^{9}Hz$ case used the curve of constant $\tilde{\lambda}$, there was no evidence to suggest that one case performed better than the other. Lastly, it appears that when material 1 (corresponding to relaxation parameter τ_1) is of the highest proportion, the optimization routine is best able to resolve τ_1. Likewise, if material 1 is of a lower proportion, the routine instead does a better job of resolving τ_2. Note that there are several instances where the optimizer "switched" τ_1 and τ_2, for example in case 1 of frequency $10^{9}Hz$ with $\alpha_1 = .5$. In this scenario each material comprises 50% of the whole, so the problem is symmetric and swapping τ_1 and τ_2 has no effect. However, in case 1 of frequency $10^{9}Hz$ with $\alpha_1 = .1$, it appears that τ_1 is

converging toward the exact τ_2^* value, but since this problem is not symmetric, τ_2 converges to a meaningless solution.

Table 5.13: Final estimates for τ_1 after two step optimization approach using a frequency of $10^{11}Hz$ for each set of initial conditions (recall the exact solution τ_1^* =3.1600e-8).

	α_1		
case	.1	.5	.9
1	1.57221e-07	2.81579e-08	2.61108e-08
2	6.34951e-08	4.63981e-08	3.15232e-08
3	3.98043e-08	3.33803e-08	3.2833e-08

Table 5.14: Final estimates for τ_1 after two step optimization approach using a frequency of $10^{9}Hz$ for each set of initial conditions (recall the exact solution τ_1^* =3.1600e-8).

	α_1		
case	.1	.5	.9
1	1.12709e-08	1.58005e-08	3.15929e-08
2	3.1574e-08	3.16002e-08	3.16017e-08
3	3.16009e-08	3.16009e-08	3.16009e-08

Table 5.15: Final estimates for τ_1 after two step optimization approach using a frequency of $10^{6}Hz$ for each set of initial conditions (recall the exact solution τ_1^* =3.1600e-8).

	α_1		
case	.1	.5	.9
1	3.17673e-08	3.16031e-08	3.16986e-08
2	3.16206e-08	3.16068e-08	3.16031e-08
3	3.16031e-08	3.16039e-08	3.16053e-08

Table 5.16: Final estimates for τ_2 after two step optimization approach using a frequency of $10^{11}Hz$ for each set of initial conditions (recall the exact solution τ_2^* =1.5800e-8).

	α_1		
case	.1	.5	.9
1	1.51273e-08	1.68275e-08	2.93245e-07
2	1.53699e-08	1.36276e-08	1.61391e-08
3	1.56196e-08	1.53854e-08	1.35142e-08

Table 5.17: Final estimates for τ_2 after two step optimization approach using a frequency of $10^{9}Hz$ for each set of initial conditions (recall the exact solution τ_2^* =1.5800e-8).

	α_1		
case	.1	.5	.9
1	1.75594e-08	3.15995e-08	1.58782e-08
2	1.58008e-08	1.57994e-08	1.57801e-08
3	1.58001e-08	1.5799e-08	1.57925e-08

Table 5.18: Final estimates for τ_2 after two step optimization approach using a frequency of $10^{6}Hz$ for each set of initial conditions (recall the exact solution τ_2^* =1.5800e-8).

	α_1		
case	.1	.5	.9
1	1.52384e-08	1.52286e-08	1.61666e-08
2	1.5787e-08	1.45007e-08	1.18861e-08
3	1.57845e-08	1.55744e-08	1.5783e-08

5.2 Determination of Volume Proportions

We now attempt to apply a one parameter Levenberg-Marquardt optimization routine to our problem to identify the relative amounts of two materials with known, distinct relaxation times. Thus we are trying to find the corresponding volume proportions of the two materials (α_1 and $\alpha_2 := 1 - \alpha_1$). We again consider the three scenarios with respect to the exact volume proportions: $\alpha_1 \in \{.1, .5, .9\}$. We also perform our inverse problem using the frequencies $10^{11}Hz$, $10^{9}Hz$ and $10^{6}Hz$. Lastly we test the optimization procedure with three various initial conditions: $\alpha_1^0 \in \{.9999, .0001, .5\}$ (except in the case when $\alpha_1^* = .5$ in which case we used $\alpha_1^0 \in \{.9999, .0001, .4\}$). We refer to these as Cases 1, 2, and 3, respectively. In all of the following we assume that the known relaxation times are $\tau_1 = 10^{-7.50031} \approx 3.16 \times 10^{-8}$ and $\tau_2 = 10^{-7.80134} \approx 1.58 \times 10^{-8}$.

Figures 5.9 through 5.11 depict the curves that we are attempting to minimize. For each case the curves appear well behaved. The results for this one parameter inverse problem, displayed in Tables 5.19 through 5.21, verify that the relative proportions of known materials are generally easily identifiable. Tables 5.22 through 5.24 display the final objective function values for each case. Note that typical initial values for J were around 0.1, further, the tolerance was set at 10^{-9}, thus all but a few cases converged before reaching the maximum of 20 iterations.

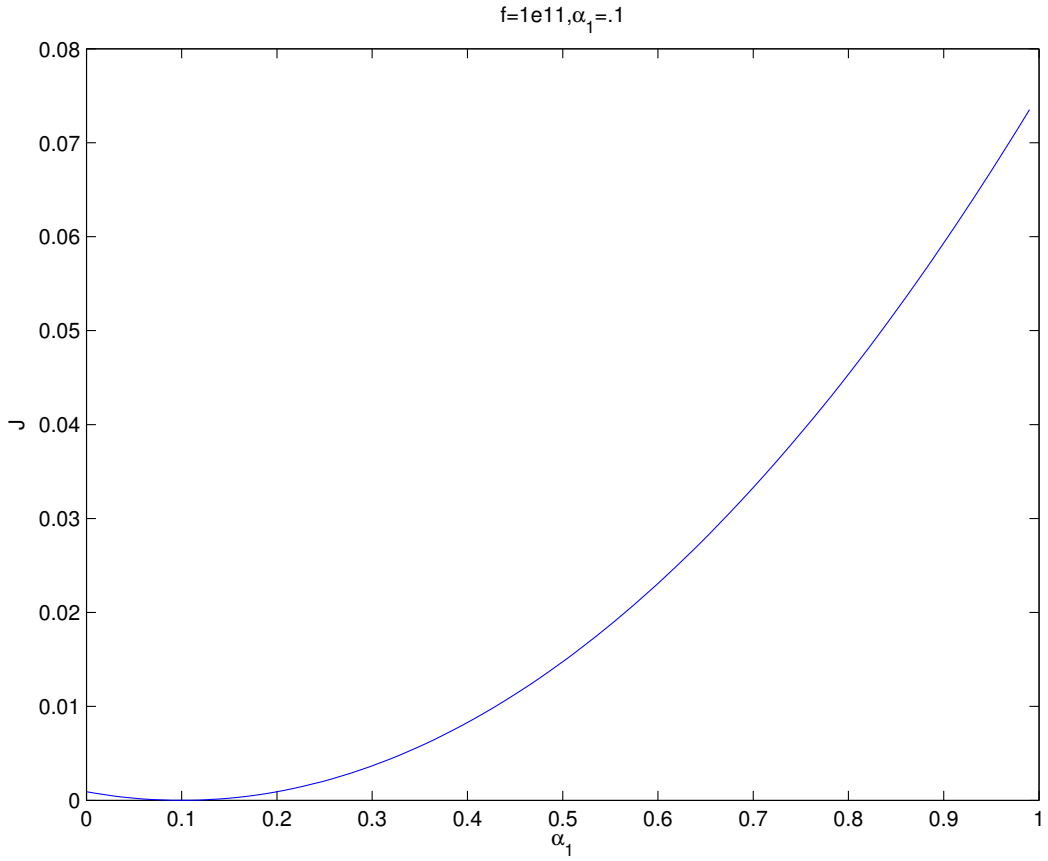

Figure 5.9: The objective function for the relaxation time inverse problem plotted versus α_1 using a frequency of $10^{11}Hz$ and $\alpha_1^* = .1$.

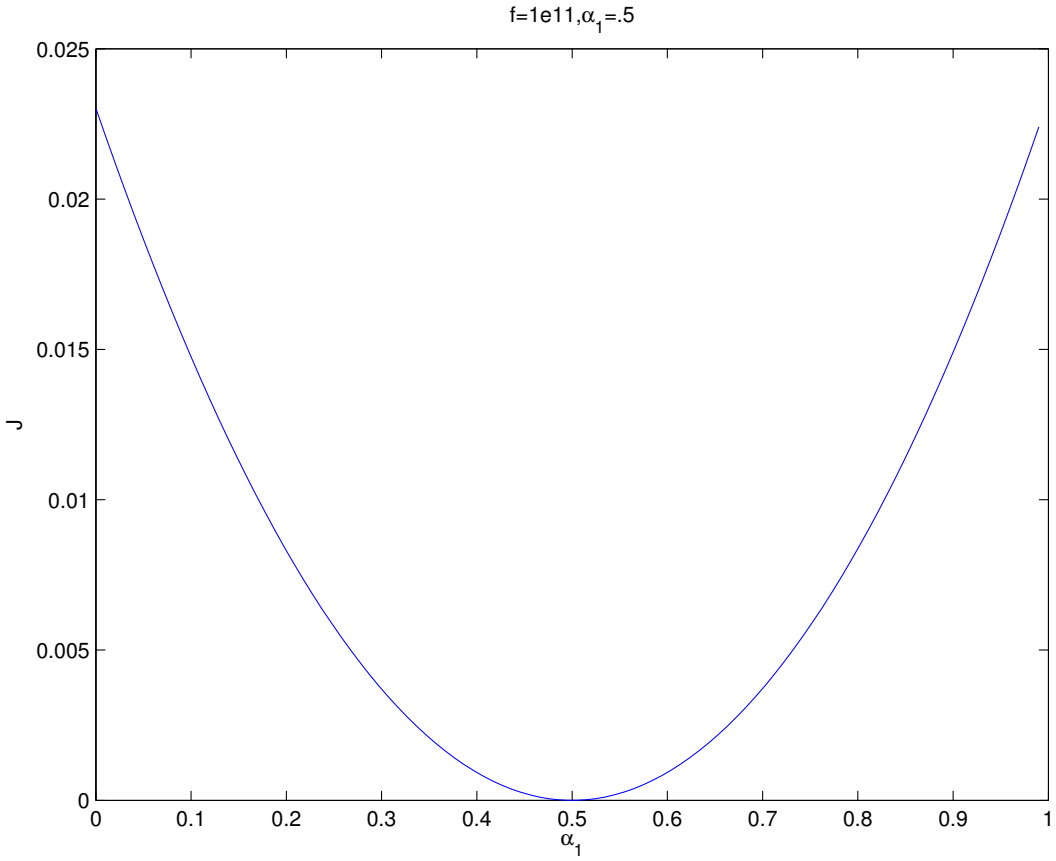

Figure 5.10: The objective function for the relaxation time inverse problem plotted versus α_1 using a frequency of $10^{11}Hz$ and $\alpha_1^* = .5$.

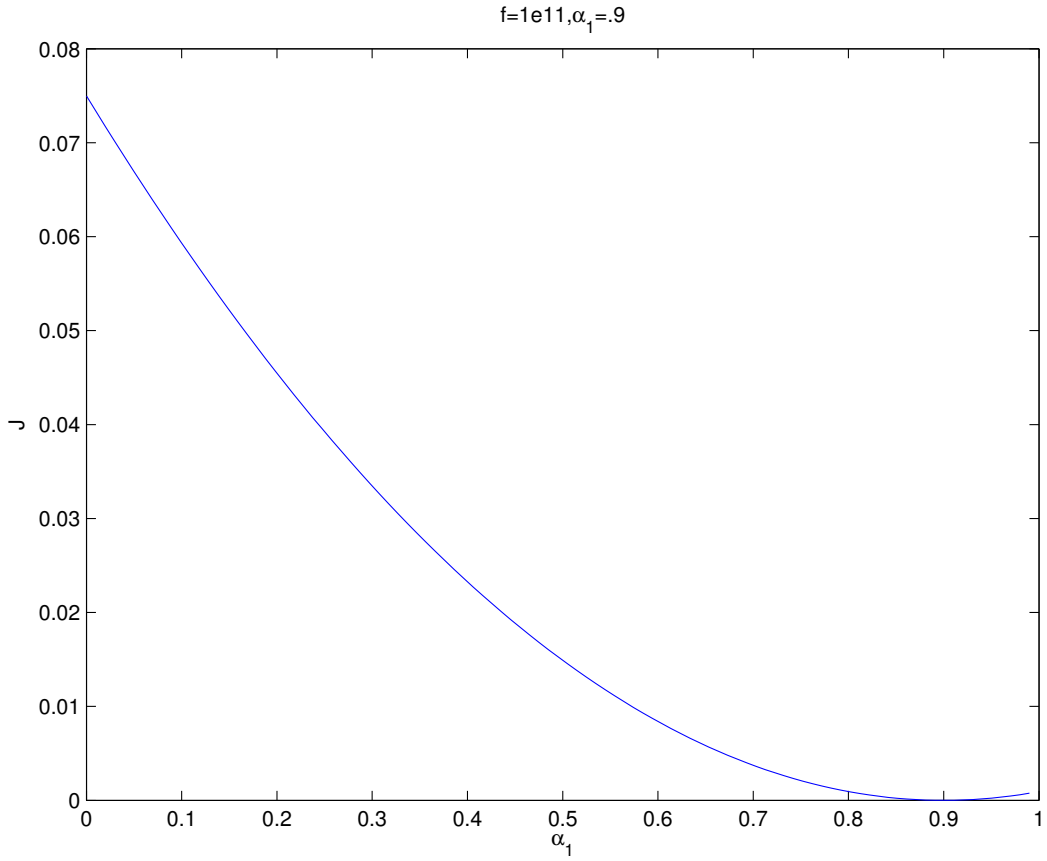

Figure 5.11: The objective function for the relaxation time inverse problem plotted versus α_1 using a frequency of $10^{11}Hz$ and $\alpha_1^* = .9$.

Table 5.19: Results for the one parameter inverse problem to determine the relative proportion of two known Debye materials using a frequency of $10^{11}Hz$ (α_1 estimates are shown).

	α_1		
case	.1	.5	.9
1	0.10095	0.501353	0.900013
2	0.0999994	0.5	0.9
3	0.100643	0.499994	0.899994

Table 5.20: Results for the one parameter inverse problem to determine the relative proportion of two known Debye materials using a frequency of $10^{9}Hz$ (α_1 estimates are shown).

	α_1		
case	.1	.5	.9
1	0.10086	0.5	0.9
2	0.0999161	0.5	0.9
3	0.100017	0.5	0.9

Table 5.21: Results for the one parameter inverse problem to determine the relative proportion of two known Debye materials using a frequency of $10^{6}Hz$ (α_1 estimates are shown).

	α_1		
case	.1	.5	.9
1	0.0995386	0.5	0.900008
2	0.0999965	0.499969	0.899996
3	0.100013	0.499999	0.899999

Table 5.22: Final objective function values for the inverse problem to determine the relative proportion of two known Debye materials using a frequency of $10^{11} Hz$.

	α_1		
case	.1	.5	.9
1	8.27897e-08	1.69802e-07	1.81577e-11
2	3.46217e-14	1.64325e-18	1.8982e-15
3	3.79016e-08	3.76649e-12	2.91698e-12

Table 5.23: Final objective function values for the inverse problem to determine the relative proportion of two known Debye materials using a frequency of $10^{9} Hz$.

	α_1		
case	.1	.5	.9
1	1.63248e-05	1.25127e-12	6.89036e-14
2	1.55308e-07	5.89446e-13	5.8576e-14
3	6.53272e-09	2.37274e-12	5.77714e-15

Table 5.24: Final objective function values for the inverse problem to determine the relative proportion of two known Debye materials using a frequency of $10^{6} Hz$.

	α_1		
case	.1	.5	.9
1	7.74602e-08	7.31725e-15	4.39638e-12
2	4.51572e-12	1.40031e-10	1.03552e-12
3	6.11308e-11	2.0608e-13	1.53426e-13

5.3 Determination of Volume Proportions and Relaxation Times Simultaneously

Although we anticipate this problem formulation to be underdetermined, we run our optimization routine again for the problem where neither the relaxation times, nor the relative volume proportions, of two distinct Debye materials are known. Thus this is a three parameter inverse problem for $\{\tau_1, \tau_2, \alpha_1\}$ (since $\alpha_2 = 1 - \alpha_1$). Again we consider the following scenarios with respect to the actual volume proportions: $\alpha_1 \in \{.1, .5, .9\}$. We also perform our inverse problem using the frequencies $10^{11}Hz$, 10^9Hz and 10^6Hz. Lastly we test the optimization procedure with the three various initial conditions that were given in Table 5.1. Note that the actual values are still $\tau_1 = 10^{-7.50031} \approx 3.16 \times 10^{-8}$ and $\tau_2 = 10^{-7.80134} \approx 1.58 \times 10^{-8}$.

Our initial condition for the volume distribution is $\alpha_1^0 = .9999$, which means there is essentially only material 1. We chose this initial condition mainly to see whether the optimization routine would try to compensate for the altered volume distribution by significantly changing the relaxation times and not sufficiently correcting the volume distribution. This is in fact what seems to have occurred. The final α_1 values are given in Tables 5.25 through 5.27, while the final τ_1 and τ_2 values are in Tables 5.28 through 5.30 and 5.31 through 5.33 respectively. Tables 5.34 through 5.36 display the final objective function values. Any values of the final objective function under the tolerance of 10^{-9} should be considered as indicative of convergence, while values greater than 1 clearly indicate stagnation, (e.g., 10^9Hz: case 1).

Of the cases that converged, none converged to the correct solution. For example, the final values of α_1 were all greater than .6, (although the estimates corresponding to a smaller α_1^* were on average less than the estimates corresponding to $\alpha_1^* = .9$). When looking at the final estimates for the relaxation times, however, there appears to be no rhyme nor reason. This is quite similar to what happened when we first tried to determine unknown relaxation times, but with a fixed volume proportion, in Section 5.1. Thus we may expect that here again no single parameter, τ_1, τ_2, nor α_1, may converge, but instead we may see convergence of a general relation involving them all, namely $\tilde{\lambda} := \frac{\alpha_1}{c\tau_1} + \frac{\alpha_2}{c\tau_2}$ (or respectively $\tilde{\tau} := \alpha_1\tau_1 + \alpha_2\tau_2$ for angular frequencies less than $\frac{1}{\tilde{\tau}}$).

We redisplay the exact values of $\tilde{\lambda}$ and $\tilde{\tau}$ in Table 5.37 for reference. Also, the

Table 5.25: Resulting values of α_1 for the underdetermined inverse problem using a frequency of $10^{11}Hz$.

	α_1^*		
case	.1	.5	.9
1	0.606255	0.881722	0.912728
2	0.761665	0.817744	0.877667
3	0.818091	0.879896	0.942175

Table 5.26: Resulting values of α_1 for the underdetermined inverse problem using a frequency of $10^{9}Hz$.

	α_1		
case	.1	.5	.9
1	0.941041	0.941091	0.880293
2	0.999811	0.993342	0.994368
3	0.990988	0.96514	0.965754

Table 5.27: Resulting values of α_1 for the underdetermined inverse problem using a frequency of $10^{6}Hz$.

	α_1		
case	.1	.5	.9
1	0.687959	0.746478	0.956578
2	0.83678	0.900072	0.908588
3	0.890569	0.841634	0.945684

initial values of $\tilde{\lambda}$ and $\tilde{\tau}$ for each case of initial conditions (recall Table 5.1) is given in Table 5.38. Finally, Tables 5.39 through 5.41 display the error of the final resulting $\tilde{\lambda}$ (or $\tilde{\tau}$ appropriately) estimates from the exact solutions (i.e., the absolute values of the differences). We show the errors instead of the actual values because some cases converged so well that the number of decimal places required to see discrepancies is impractical to show! Thus while the inverse problem was unable to accurately resolve the individual values τ_1, τ_2, and α_1, in all but a few cases (particularly in the 10^9Hz scenario) the optimization routine did converge as well as to be expected. In the previous section, with the fixed volume proportions, we were able to traverse the curve of constant $\tilde{\lambda}$ (or $\tilde{\tau}$ appropriately) to find the global minimum. However, here we truly have an underdetermined problem, and all attempts on our part to further minimize the objective function have been futile.

Table 5.28: Resulting values of τ_1 for the underdetermined inverse problem using a frequency of $10^{11} Hz$ (recall the exact solution τ_1^* =3.1600e-8).

	α_1		
case	.1	.5	.9
1	3.9469e-08	5.28765e-07	3.23635e-08
2	1.52948e-08	2.49314e-08	2.60749e-08
3	1.79134e-08	2.40213e-08	3.06153e-08

Table 5.29: Resulting values of τ_1 for the underdetermined inverse problem using a frequency of $10^{9} Hz$ (recall the exact solution τ_1^* =3.1600e-8).

	α_1		
case	.1	.5	.9
1	1.2046e-07	1.24415e-07	5.50848e-07
2	1.67567e-08	2.16631e-08	2.93323e-08
3	1.65557e-08	2.25001e-08	3.0285e-08

Table 5.30: Resulting values of τ_1 for the underdetermined inverse problem using a frequency of $10^{6} Hz$ (recall the exact solution τ_1^* =3.1600e-8).

	α_1		
case	.1	.5	.9
1	2.12522e-08	2.81013e-08	3.10195e-08
2	1.91221e-08	2.3216e-08	3.15199e-08
3	2.58248e-08	2.67889e-08	3.11248e-08

Table 5.31: Resulting values of τ_2 for the underdetermined inverse problem using a frequency of $10^{11} Hz$ (recall the exact solution τ_2^* =1.5800e-8).

	α_1		
case	.1	.5	.9
1	8.79556e-09	2.58245e-09	1.32076e-08
2	2.30775e-08	1.24249e-08	1.06318e-07
3	1.25825e-08	1.10813e-08	1.4329e-08

Table 5.32: Resulting values of τ_2 for the underdetermined inverse problem using a frequency of $10^{9} Hz$ (recall the exact solution τ_2^* =1.5800e-8).

	α_1		
case	.1	.5	.9
1	1.81687e-10	2.32623e-10	1.2353e-09
2	4.08525e-10	4.11677e-09	6.18566e-09
3	3.36629e-08	7.61993e-09	1.17231e-08

Table 5.33: Resulting values of τ_2 for the underdetermined inverse problem using a frequency of $10^{6} Hz$ (recall the exact solution τ_2^* =1.5800e-8).

	α_1		
case	.1	.5	.9
1	8.82441e-09	1.06962e-08	7.87058e-09
2	8.40313e-09	2.78555e-08	1.5107e-08
3	6.19113e-09	7.15491e-09	1.0713e-08

Table 5.34: Resulting values of the objective function J for the underdetermined inverse problem using a frequency of $10^{11}Hz$.

	α_1^*		
case	.1	.5	.9
1	1.87304e-09	1.39638e-07	2.96012e-12
2	1.87016e-15	3.3089e-14	1.60601e-17
3	2.79754e-14	2.80156e-16	1.38435e-13

Table 5.35: Resulting values of the objective function J for the underdetermined inverse problem using a frequency of $10^{9}Hz$.

	α_1		
case	.1	.5	.9
1	9.59505	13.787	25.045
2	0.00021558	2.49585e-06	2.03659e-07
3	3.48546e-06	5.0347e-07	1.18429e-08

Table 5.36: Resulting values of the objective function J for the underdetermined inverse problem using a frequency of $10^{6}Hz$.

	α_1		
case	.1	.5	.9
1	1.19225e-05	4.76542e-07	1.18516e-07
2	6.34493e-07	3.86474e-05	4.41757e-10
3	4.07294e-06	1.99923e-06	2.75692e-08

Table 5.37: The exact values of $\tilde{\lambda} := \frac{\alpha_1}{c\tau_1} + \frac{\alpha_2}{c\tau_2}$ (first row) and $\tilde{\tau} := \alpha_1\tau_1 + \alpha_2\tau_2$ (second row) for each set of volume distributions.

	α_1^*		
	.1	.5	.9
$\tilde{\lambda}^*$	0.200556	0.158333	0.116111
$\tilde{\tau}^*$	1.7380e-08	2.3700e-08	3.0020e-08

Table 5.38: The initial values of $\tilde{\lambda} := \frac{\alpha_1}{c\tau_1} + \frac{\alpha_2}{c\tau_2}$ (first column) and $\tilde{\tau} := \alpha_1\tau_1 + \alpha_2\tau_2$ (second column) for each set of initial conditions.

case	$\tilde{\lambda}^0$	$\tilde{\tau}^0$
1	0.0212146	1.57985e-07
2	0.0528147	6.31945e-08
3	0.0844624	3.94973e-08

Table 5.39: Error of the resulting values of $\tilde{\lambda}$ from the exact values for the underdetermined inverse problem using a frequency of $10^{11}Hz$ for each set of initial conditions.

	α_1		
case	.1	.5	.9
1	2.99851e-08	7.35704e-08	3.49983e-09
2	1.23759e-10	4.68118e-10	2.30235e-10
3	1.14292e-09	2.16657e-10	1.273e-10

Table 5.40: Error of the resulting values of $\tilde{\lambda}$ from the exact values for the underdetermined inverse problem using a frequency of $10^{9}Hz$ for each set of initial conditions.

	α_1		
case	.1	.5	.9
1	0.907928	0.711589	0.212452
2	4.93369e-06	1.05337e-05	1.47737e-06
3	3.86466e-06	4.68234e-06	6.40273e-08

Table 5.41: Error of the resulting values of $\tilde{\tau}$ from the exact values for the underdetermined inverse problem using a frequency of $10^{6}Hz$ for each set of initial conditions.

	α_1		
case	.1	.5	.9
1	5.78065e-12	1.12783e-11	5.70111e-12
2	7.42983e-12	2.03867e-11	4.54227e-13
3	2.3737e-11	2.04292e-11	3.88617e-12

5.4 Inverse Problem Using Uniform Distribution

The previous polarization inverse problems have assumed a discrete distribution with two atoms. According to experimental reports [BB78], most materials demonstrate polarization effects described by a range of relaxation times. Here we consider the simplest of distributions by exploring the possibility of a uniform distribution of relaxations times (τ) between a lower and upper limit (τ_a and τ_b respectively). This presents us again with a two parameter inverse problem, namely, to try to resolve the end points of the distribution used to generate the given data. Computationally we still approximate this distribution with discrete nodes, but instead of just one at each endpoint, we use $N = 11$ uniformly distributed within the interval. Thus the total polarization (see Section 4.1 for the formulation of our model using distributions of relaxation parameters)

$$P(t,z) = \int_0^t \mathcal{G}(t-s,z)E(s,z)ds$$

is now approximated by

$$P^N(t,z) = \int_0^t \mathcal{G}^N(t-s,z)E(s,z)ds$$

where $\mathcal{G}^N$ is a quadrature rule approximation to

$$\mathcal{G}(t,z;F) = \int_{\tau_a}^{\tau_b} g(t,z;\tau)dF(\tau)$$

with $dF(\tau) = \frac{d\tau}{\tau_b - \tau_a}$ for a uniform distribution. Note: use of a rectangular quadrature rule did not produce good results in the inverse problem, therefore we chose to use the Composite Simpson's rule.

Figures 5.12 and 5.13 depict the objective function and the log of the objective function, respectively, for a frequency of $10^{11}Hz$. The solid line in figure 5.12 is the curve of constant $\tilde{\lambda}$. Given a uniform distribution of relaxation times in a Debye media, this parameter is given by

$$\tilde{\lambda} := \frac{1}{c(\tau_b - \tau_a)} \int_{\tau_a}^{\tau_b} \frac{d\tau}{\tau} = \frac{\ln \tau_b - \ln \tau_a}{c(\tau_b - \tau_a)}. \tag{5.4}$$

While the curve appears slightly different from the discrete distribution case in Figure 5.2, the fact that this objective function is also small along this curve suggests that this problem should behave similarly to the discrete distribution case in Section 5.1. Figures 5.14 and 5.15 depict the objective function and the log of the objective function, respectively, for

a frequency of $10^6 Hz$. We notice that again the orientation of the "curve of best" fit is different from the higher frequency case. The solid line in figure 5.14 is the curve of constant $\tilde{\tau} := \int_{\tau_a}^{\tau_b} \tau dF(\tau) = \frac{\tau_b - \tau_a}{2}$. Again, the fact that the $\tilde{\lambda}$ term only dominates the behavior when the interrogating frequency is greater than $\frac{1}{2\pi\tilde{\tau}}$ is consistent with the discrete distribution case.

Anticipating from our previous experience with the discrete distribution, we decided not to perform the two parameter inverse problem as before, expecting it to simply converge to the "line of best fit". Instead, we minimized over just one parameter, τ_a, leaving τ_b fixed at its initial value. In this way we still converge to the "line of best fit" but theoretically use half as many function evaluations since we only compute one gradient at each step (in practice, actually a third as many function evaluations were needed to get the same order of accuracy as the two parameter inverse problem).

We performed the one parameter inverse problem using the three initial condition cases described above in Table 5.1 and again using frequencies $10^{11} Hz$, $10^9 Hz$ and $10^6 Hz$. The τ_a estimates after running Levenberg-Marquardt on the modified least squares objective function are given in Table 5.42. Again, as in the discrete case, the values of the relaxation times do not appear to be converging to the correct solution. But we expect that the optimization routine is converging to the "curve of best fit". To test this we must look at the approximations to $\tilde{\lambda}$ and $\tilde{\tau}$.

Table 5.42: Resulting values of τ_a after the one parameter Levenberg-Marquardt routine for the inverse problem to determine the endpoints of a uniform distribution of relaxation times (recall the exact solution τ_a^* =3.16000e-8).

	Initial	Frequency (Hz)		
case		10^{11}	10^9	10^6
1	1.58000e-7	5.41874e-8	5.40910e-8	3.59781e-8
2	6.32000e-8	4.01846e-8	4.01788e-8	3.43510e-8
3	3.95000e-8	3.41828e-8	3.41820e-8	3.27009e-8

The initial values of $\tilde{\lambda}$ and $\tilde{\tau}$ are given in Tables 5.43 and 5.44 respectively (note that these values were computed by $\tilde{\lambda} \approx \sum_i \frac{\alpha_i}{c\tau_i}$ and $\tilde{\tau} \approx \sum_i \alpha_i \tau_i$ using appropriately defined $\{\alpha_i\}_{i=0}^{N-1}$ determined by the Composite Simpson's rule). The exact values of each are $\tilde{\lambda}^* = 0.248369$ and $\tilde{\tau}* = 5.42467 \times 10^{-8}$. The resulting $\tilde{\lambda}$ and $\tilde{\tau}$ values after running the one parameter Levenberg-Marquardt routine are given in Tables 5.45 and 5.46 respectively. Clearly each case has converged to the "line of best fit"; in general the closer initial

conditions converged closer to the actual value of $\tilde{\lambda}$ (or $\tilde{\tau}$ for $f = 10^6 Hz$).

Table 5.43: The initial values of $\tilde{\lambda} := \sum_i \frac{\alpha_i}{c\tau_i}$ for each set of initial conditions for the inverse problem to determine the endpoints of a uniform distribution of relaxation times (case 0 represents the exact solution).

case	Frequency (Hz) $10^{11} - 10^9$
0	0.248369
1	0.115739
2	0.176705
3	0.223136

Table 5.44: The initial values of $\tilde{\tau} := \sum_i \alpha_i \tau_i$ for each set of initial conditions for the inverse problem to determine the endpoints of a uniform distribution of relaxation times (case 0 represents the exact solution).

case	Frequency (Hz) 10^6
0	5.42467e-8
1	2.33313e-7
2	9.66433e-8
3	6.42533e-8

After our one parameter optimization routine resolved $\tilde{\lambda}$ (or $\tilde{\tau}$ for $f = 10^6 Hz$), we minimized for τ_a along the line of constant $\tilde{\lambda}$ (or $\tilde{\tau}$). Again, this is a one parameter inverse problem, and therefore very efficient. The results of these computations are given in Tables 5.47 and 5.48, for τ_a and the corresponding τ_b (given constant $\tilde{\lambda}$ or $\tilde{\tau}$), respectively.

Finally, for fine tuning, we apply the full two parameter Levenberg-Marquardt routine using the estimates from minimizing along constant $\tilde{\lambda}$ (or $\tilde{\tau}$). We see that the estimates change very little, if at all, which suggests that our approximation method is not only efficient, but quite accurate as well.

Table 5.45: Resulting values of $\tilde{\lambda}$ after the Levenberg-Marquardt routine for the inverse problem to determine the endpoints of a uniform distribution of relaxation times for each set of initial conditions (case 0 represents the exact solution). The values in parenthesis denote the absolute value of the difference as the number of digits shown here would not suffuciently distinguish the approximations from the exact solution.

	Frequency (Hz)	
case	10^{11}	10^{9}
0	0.248369	0.248369
1	(1.64144e-8)	0.248701
2	(1.51187e-9)	0.248396
3	(5.12895e-11)	0.248373

Table 5.46: Resulting values of $\tilde{\tau}$ after the Levenberg-Marquardt routine for the inverse problem to determine the endpoints of a uniform distribution of relaxation times using a frequency of $10^6 Hz$ for each set of initial conditions (case 0 represents the exact solution).

	Frequency (Hz)
case	10^{6}
0	5.42467e-8
1	5.43479e-8
2	5.43315e-8
3	5.42813e-8

Table 5.47: Resulting values of τ_a after minimizing along the line of constant $\tilde{\lambda}$ (or $\tilde{\tau}$ for $f = 10^6 Hz$), for the inverse problem to determine the endpoints of a uniform distribution of relaxation times (recall the exact solution τ_a^* =3.16000e-8).

	Frequency (Hz)		
case	10^{11}	10^{9}	10^{6}
1	3.08694e-08	3.1653e-08	3.17617e-08
2	3.16401e-08	3.16043e-08	3.17357e-08
3	3.15905e-08	3.16007e-08	3.16559e-08

Table 5.48: Resulting values of τ_b after the minimizing along the line of constant $\tilde{\lambda}$ (or $\tilde{\tau}$ for $f = 10^6 Hz$), for the inverse problem to determine the endpoints of a uniform distribution of relaxation times (recall the exact solution τ_b^* =1.5800e-8).

	Frequency (Hz)		
case	10^{11}	10^{9}	10^{6}
1	1.68829e-08	1.56448e-08	1.55282e-08
2	1.57433e-08	1.57874e-08	1.55715e-08
3	1.58134e-08	1.5798e-08	1.57053e-08

Table 5.49: Resulting values of τ_a after the two parameter Levenberg-Marquardt routine for the inverse problem to determine the endpoints of a uniform distribution of relaxation times (recall the exact solution τ_a^* =3.16000e-8).

	Frequency (Hz)		
case	10^{11}	10^9	10^6
1	3.08694e-08	3.15996e-08	3.16014e-08
2	3.16401e-08	3.16005e-08	3.16008e-08
3	3.15905e-08	3.16008e-08	3.16002e-08

Table 5.50: Resulting values of τ_b after the two parameter Levenberg-Marquardt routine for the inverse problem to determine the endpoints of a uniform distribution of relaxation times (recall the exact solution τ_b^* =1.58000e-8).

	Frequency (Hz)		
case	10^{11}	10^9	10^6
1	1.68829e-08	1.58005e-08	1.57988e-08
2	1.57433e-08	1.57993e-08	1.57991e-08
3	1.58134e-08	1.57988e-08	1.57998e-08

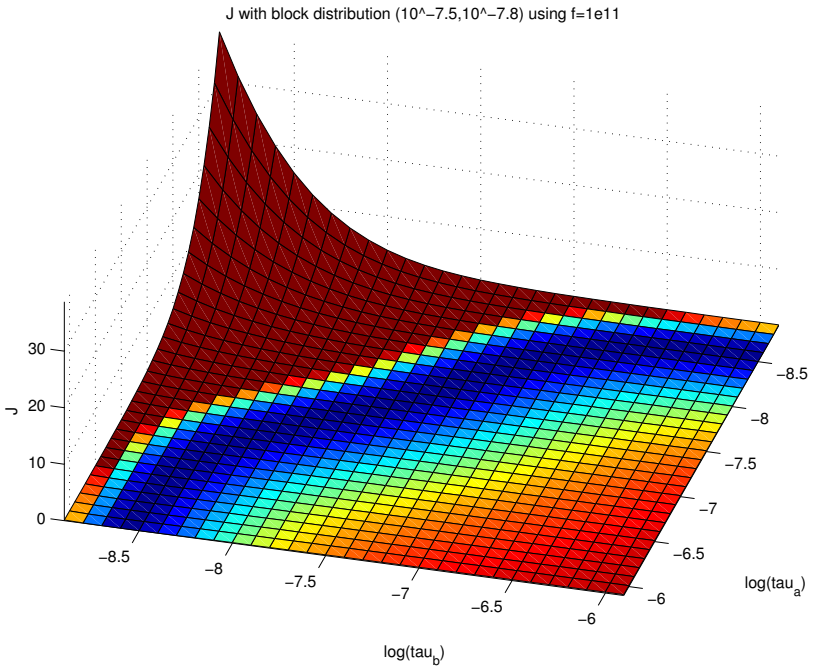

Figure 5.12: The objective function for the uniform distribution inverse problem plotted versus the log of τ_a and the log of τ_b using a frequency of $10^{11} Hz$.

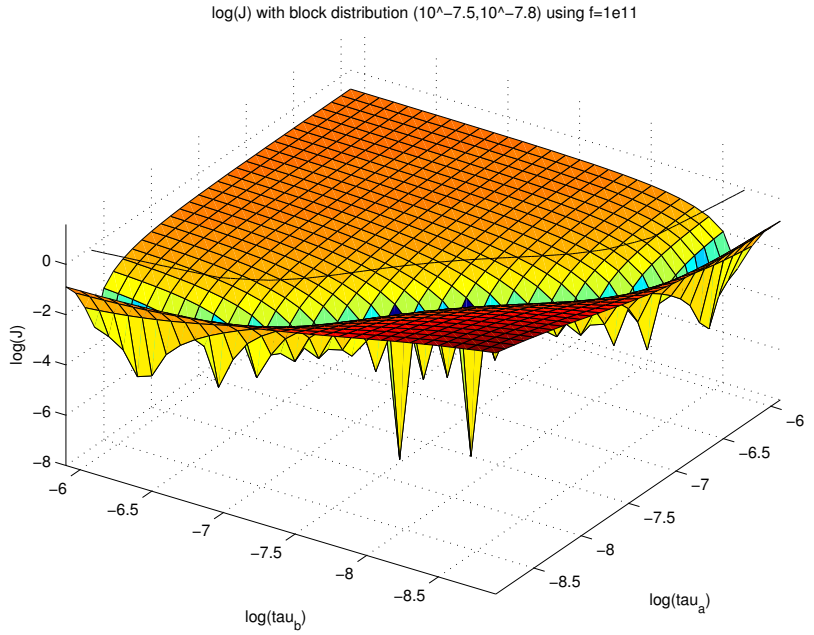

Figure 5.13: The log of the objective function for the uniform distribution inverse problem plotted versus the log of τ_a and the log of τ_b using a frequency of $10^{11} Hz$. The solid line above the surface represents the curve of constant $\tilde{\lambda}$.

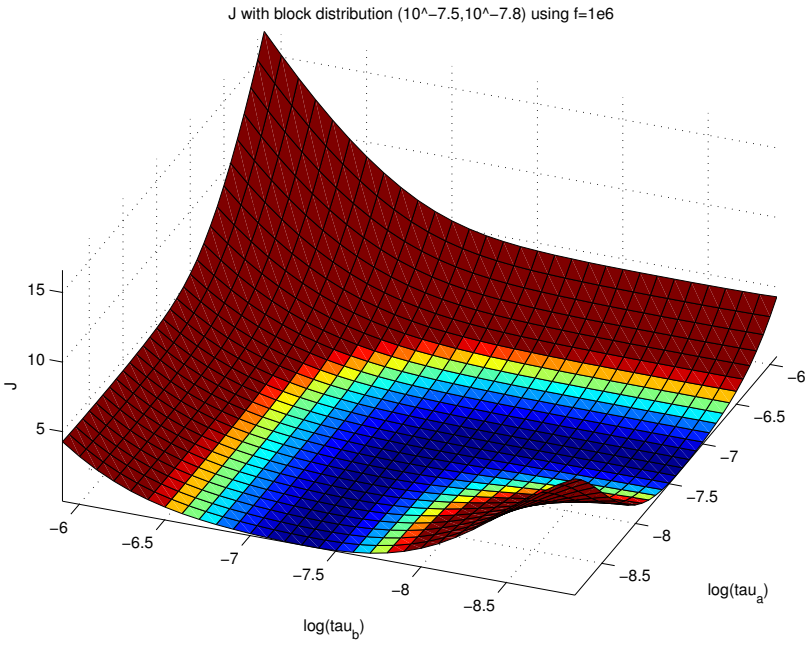

Figure 5.14: The objective function for the uniform distribution inverse problem plotted versus the log of τ_a and the log of τ_b using a frequency of $10^6 Hz$.

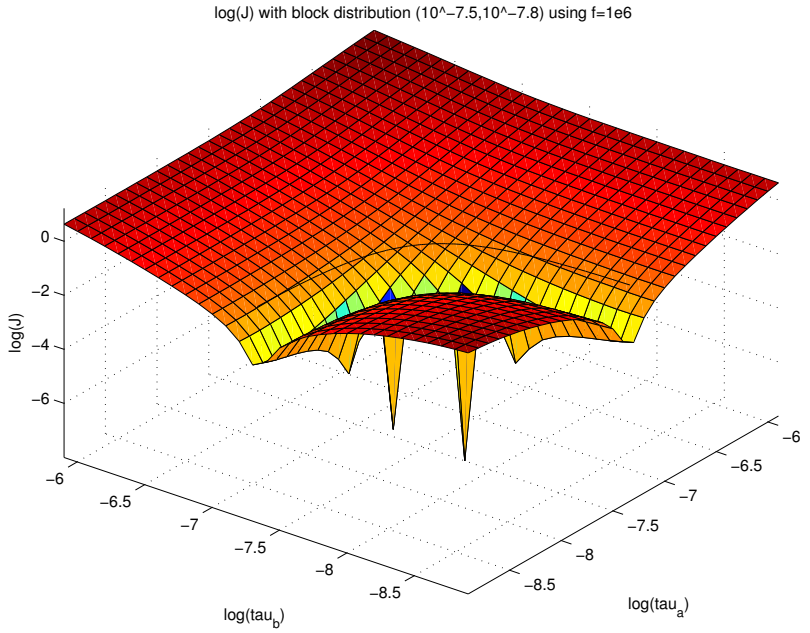

Figure 5.15: The log of the objective function for the uniform distribution inverse problem plotted versus the log of τ_a and the log of τ_b using a frequency of $10^6 Hz$. The solid line above the surface represents the curve of constant $\tilde{\tau}$.

Chapter 6

Homogenization of Periodically Varying Coefficients in Electromagnetic Materials

Another way to model a heterogeneous material is with homogenization techniques. We now consider the behavior of the electromagnetic field in a material presenting heterogeneous microstructures (composite materials) which are described by spatially periodic parameters $\epsilon_r(\mathbf{x})$, $\sigma(\mathbf{x})$ and $g(t, \mathbf{x})$. We will subject such composite materials to electromagnetic fields generated by currents of varying frequencies. When the period of the structure is small compared to the wavelength, the coefficients in Maxwell's equations oscillate rapidly. These oscillating coefficients are difficult to handle numerically, especially when the period is very small compared to the wavelength. Homogenization techniques attempt to replace the varying parameters with new effective, constant coefficients. The approach we employ is based on the periodic unfolding method presented in [CDG04]. The homogenized parameters will depend on corrector terms which are solutions to local problems posed on the reference cell Y in a periodic structure.

6.1 Introduction

In [SEK03], a method based on spectral expansions for Maxwell's equations is presented, which utilizes eigenvectors of the curl operators combined with the microscopic description of the material. The homogenized material is represented using mean values of only a few eigenvectors. This method relies on the material being lossless, in which case Maxwell's equations can be associated with a self-adjoint partial differential operator. However, most materials usually have losses due to a small conductitvity or dispersive effects, which makes the corresponding operator in Maxwell's equations non-selfadjoint. In [S04] the author uses a singular value decomposition for the analyzing non-selfadjoint operators that arise in Maxwell's equations. The author expands the electromagnetic field in the modes corresponding to the singular values, and shows that only the smallest singular values make a significant contibution to the total field when the scale is small. Using this approach the author finds effective, or homogenized, material parameters for Maxwell's equations when the microscopic scale becomes small compared to the scale induced by the frequencies of the imposed currents. In [ES04], the authors compare two different homogenization methods for Maxwell's equations in two and three dimensions. The first method is the classical way of determining the homogenized coefficients [CD99], which consists of solving an elliptic problem in a unit cell, and the second is the method described in [SEK03]. See also [WK02, K04, K01] for other approaches/techniques for homogenization of Maxwell's equations.

In the following sections, we present the problem that is of interest to us and then set up the corresponding homogenized problem to be solved. We refer the reader to [BGM04] for the relevant theory.

6.2 Maxwell's Equations in a Continuous Medium

We describe Maxwell's equations for a linear and isotropic medium in a form that includes terms for the electric polarization as

$$\frac{\partial \mathbf{D}}{\partial t} + \mathbf{J}_c - \nabla \times \mathbf{H} = \mathbf{J}_s \quad \text{in } (0,T) \times \Omega, \tag{6.1a}$$

$$\frac{\partial \mathbf{B}}{\partial t} + \nabla \times \mathbf{E} = 0 \quad \text{in } (0,T) \times \Omega, \tag{6.1b}$$

$$\nabla \cdot \mathbf{D} = \rho \quad \text{in } (0,T) \times \Omega, \tag{6.1c}$$

$$\nabla \cdot \mathbf{B} = 0 \quad \text{in } (0,T) \times \Omega, \tag{6.1d}$$

$$\mathbf{E} \times \mathbf{n} = 0 \quad \text{on } (0,T) \times \partial\Omega, \tag{6.1e}$$

$$\mathbf{E}(0,\mathbf{x}) = \mathbf{0} \quad \text{in } \Omega, \tag{6.1f}$$

$$\mathbf{H}(0,\mathbf{x}) = \mathbf{0} \quad \text{in } \Omega. \tag{6.1g}$$

The vector valued functions $\mathbf{E}$ and $\mathbf{H}$ represent the strengths of the electric and magnetic fields, respectively, while $\mathbf{D}$ and $\mathbf{B}$ are the electric and magnetic flux densities, respectively. The conduction current density is denoted by $\mathbf{J}_c$, while the source current density is provided by $\mathbf{J}_s$. The scalar ρ represents the density of free electric charges unaccounted for in the electric polarization. We assume perfectly conducting boundary conditions (6.1e), on the boundary $\partial\Omega$. We also assume zero initial conditions, (6.1f) and (6.1g), for all the unknown fields. System (6.1) is completed by constitutive laws that embody the behavior of the material in response to the electromagnetic fields. These are given in the form

$$\mathbf{D} = \epsilon_0 \epsilon_r(\mathbf{x})\mathbf{E} + \mathbf{P} \quad \text{in } (0,T) \times \Omega, \tag{6.2a}$$

$$\mathbf{B} = \mu_0 \mathbf{H} \quad \text{in } (0,T) \times \Omega. \tag{6.2b}$$

For the media that is of interest to us, we can neglect magnetic effects; we also assume that Ohms's law governs the electric conductivity, i.e.,

$$\mathbf{J}_c = \sigma(\mathbf{x})\mathbf{E} \text{ in } (0,T) \times \Omega. \tag{6.3}$$

We will modify system (6.1) and the constitutive laws (6.2) by performing a change of variables that renders the system in a form that is convenient for analysis and computation.

From (6.1a) we have

$$\frac{\partial}{\partial t}\left(\mathbf{D}+\int_0^t \mathbf{J}_c(s,\mathbf{x})\ \mathrm{ds}\right)-\nabla\times\mathbf{H}=\mathbf{J}_s \text{ in } (0,T)\times\Omega. \tag{6.4}$$

Next, we define the new variable

$$\widetilde{\mathbf{D}}(t,\mathbf{x})=\mathbf{D}(t,\mathbf{x})+\int_0^t \mathbf{J}_c(s,\mathbf{x})\ \mathrm{ds}. \tag{6.5}$$

Using definition (6.5) in (6.4) and (6.1) we obtain the modified system

$$\frac{\partial\widetilde{\mathbf{D}}}{\partial t}-\nabla\times\mathbf{H}=\mathbf{J}_s \quad \text{in } (0,T)\times\Omega, \tag{6.6a}$$

$$\frac{\partial\mathbf{B}}{\partial t}+\nabla\times\mathbf{E}=0 \quad \text{in } (0,T)\times\Omega, \tag{6.6b}$$

$$\nabla\cdot\widetilde{\mathbf{D}}=0 \quad \text{in } (0,T)\times\Omega, \tag{6.6c}$$

$$\nabla\cdot\mathbf{B}=0 \quad \text{in } (0,T)\times\Omega, \tag{6.6d}$$

$$\mathbf{E}\times\mathbf{n}=0 \quad \text{on } (0,T)\times\partial\Omega, \tag{6.6e}$$

$$\mathbf{E}(0,\mathbf{x})=\mathbf{0} \quad \text{in } \Omega, \tag{6.6f}$$

$$\mathbf{H}(0,\mathbf{x})=\mathbf{0} \quad \text{in } \Omega. \tag{6.6g}$$

We note that equation (6.6c) follows from the continuity equation $\frac{\partial\rho}{\partial t}+\nabla\cdot\mathbf{J}_c=0$, the assumption that $\rho(0)=0$, and the assumption that $\nabla\cdot\mathbf{J}_s=0$ (in the sense of distributions). The modified constitutive law (6.2a) after substitution of (6.3) and (6.5) becomes

$$\widetilde{\mathbf{D}}(t,\mathbf{x})=\epsilon_0\epsilon_r(\mathbf{x})\mathbf{E}(t,\mathbf{x})+\int_0^t \sigma(\mathbf{x})\mathbf{E}(s,\mathbf{x})\ \mathrm{ds}+\mathbf{P}(t,\mathbf{x}).$$

To describe the behavior of the media's macroscopic electric polarization $\mathbf{P}$, we employ a general integral equation model in which the polarization explicitly depends on the past history of the electric field. This model is sufficiently general to include microscopic polarization mechanisms such as dipole or orientational polarization as well as ionic and electronic polarization and other frequency dependent polarization mechanisms. The resulting constitutive law can be given in terms of a polarization or displacement susceptibility kernel ν as

$$\mathbf{P}(t,\mathbf{x})=\int_0^t \nu(t-s,\mathbf{x})\mathbf{E}(s,\mathbf{x})\ \mathrm{ds}.$$

Thus the modified constitutive laws are

$$\mathbf{D}(t,\mathbf{x}) = \epsilon_0\epsilon_r(\mathbf{x})\mathbf{E}(t,\mathbf{x}) + \int_0^t \{\sigma(\mathbf{x}) + \nu(t-s,\mathbf{x})\}\,\mathbf{E}(s,\mathbf{x})\ \mathrm{ds}, \tag{6.7a}$$

$$\mathbf{B} = \mu_0\mathbf{H}, \tag{6.7b}$$

where, in the above and henceforth we have dropped the $\widetilde{\ }$ symbol over $\mathbf{D}$, at the same time keeping in mind that $\widetilde{\mathbf{D}}$ in definition (6.5) is the modified electric flux density. Let us define the vector of fields

$$\mathbf{u} = (\mathbf{u}_1, \mathbf{u}_2)^T = (\mathbf{E}, \mathbf{H})^T \ \in\ L^2(\Omega; \mathbb{R}^6),$$

and the operator

$$\mathbf{Lu}(t,\mathbf{x}) = \begin{pmatrix} \mathbf{D}(t,\mathbf{x}) \\ \\ \mathbf{B}(t,\mathbf{x}) \end{pmatrix},$$

which from (6.7) can be written as:

$$\begin{aligned}\mathbf{Lu}(t,\mathbf{x}) = &\begin{bmatrix} \epsilon_0\epsilon_r(\mathbf{x})\mathbf{I}_3 & \mathbf{0}_3 \\ \mathbf{0}_3 & \mu_0\mathbf{I}_3 \end{bmatrix} \begin{pmatrix} \mathbf{E}(t,\mathbf{x}) \\ \mathbf{H}(t,\mathbf{x}) \end{pmatrix} \\ &+ \int_0^t \left\{ \begin{bmatrix} \sigma(\mathbf{x})\mathbf{I}_3 & \mathbf{0}_3 \\ \mathbf{0}_3 & \mathbf{0}_3 \end{bmatrix} + \begin{bmatrix} \nu(t-s,\mathbf{x})\mathbf{I}_3 & \mathbf{0}_3 \\ \mathbf{0}_3 & \mathbf{0}_3 \end{bmatrix} \right\} \begin{pmatrix} \mathbf{E}(s,\mathbf{x}) \\ \mathbf{H}(s,\mathbf{x}) \end{pmatrix} \mathrm{ds}. \end{aligned} \tag{6.8}$$

We label the three 6×6 coefficient matrices in (6.8) as

$$\mathbf{A}(\mathbf{x}) = \begin{bmatrix} \epsilon_0\epsilon_r(\mathbf{x})\mathbf{I}_3 & \mathbf{0}_3 \\ \\ \mathbf{0}_3 & \mu_0\mathbf{I}_3 \end{bmatrix},$$

$$\mathbf{B}(\mathbf{x}) = \begin{bmatrix} \sigma(\mathbf{x})\mathbf{I}_3 & \mathbf{0}_3 \\ \\ \mathbf{0}_3 & \mathbf{0}_3 \end{bmatrix},$$

$$\mathbf{C}(t,\mathbf{x}) = \begin{bmatrix} \nu(t,\mathbf{x})\mathbf{I}_3 & \mathbf{0}_3 \\ \\ \mathbf{0}_3 & \mathbf{0}_3 \end{bmatrix},$$

where, in the above definitions $\mathbf{I}_n$ is an $n\times n$ identity matrix and $\mathbf{0}_n$ is an $n\times n$ matrix of zeros, $n\in\mathbb{N}$. Using these definitions we may rewrite (6.8) as

$$\mathbf{Lu}(t,\mathbf{x}) = \mathbf{A}(\mathbf{x})\mathbf{u}(t,\mathbf{x}) + \int_0^t \mathbf{B}(\mathbf{x})\mathbf{u}(s,\mathbf{x})\ \mathrm{ds} + \int_0^t \mathbf{C}(t-s,\mathbf{x})\mathbf{u}(s,\mathbf{x})\ \mathrm{ds}. \tag{6.10}$$

Next, we define the Maxwell operator $\mathbf{M}$ as

$$\mathbf{M}\mathbf{u}(t,\mathbf{x}) = \mathbf{M}\begin{pmatrix} \mathbf{E}(t,\mathbf{x}) \\ \\ \mathbf{H}(t,\mathbf{x}) \end{pmatrix} = \begin{pmatrix} \nabla\times\mathbf{H}(t,\mathbf{x}) \\ \\ -\nabla\times\mathbf{E}(t,\mathbf{x}) \end{pmatrix} \tag{6.11}$$

and the vector $\mathbf{J}_s$ as

$$\mathbf{J}_s(t) = -J_s(t)\mathbf{e}_1 \tag{6.12}$$

where, $\mathbf{e}_1 = (1,0,0,0,0,0)^T \in \mathbb{R}^6$, is a unit basis vector. Thus Maxwell's equation with initial and boundary conditions can be rewritten in the form

$$\frac{d}{dt}\mathbf{L}\mathbf{u} = \mathbf{M}\mathbf{u} + \mathbf{J}_s(t) \quad \text{in } (0,T)\times\Omega, \tag{6.13a}$$

$$\mathbf{u}(0,\mathbf{x}) = \mathbf{0} \quad \text{in } \Omega, \tag{6.13b}$$

$$\mathbf{u}_1(t,\mathbf{x})\times\mathbf{n}(\mathbf{x}) = \mathbf{0} \quad \text{on } (0,T)\times\partial\Omega. \tag{6.13c}$$

where L is the operator associated with the constitutive law (6.10), and M is the Maxwell operator (6.11). Note that the exterior source term $\mathbf{J}_s$ has only one non-zero component.

We assume that the structure that occupies the domain Ω presents periodic microstructures leading to matrices $\mathbf{A}, \mathbf{B}$ and $\mathbf{C}$ with spatially oscillatory coefficients. Namely, we will assume that ϵ_r and σ are rapidly oscillating spatial functions.

6.3 The Homogenized Problem

We denote by Y the reference cell of the periodic structure that occupies Ω. The construction of the homogenized problem involves solving for the *corrector* subterms $\bar{w}_k^A \in H^1_{\text{per}}(Y;\mathbb{R}^2)$, $\bar{w}_k$ and $\bar{w}_k^0 \in W^{1,1}(0,T;H^1_{\text{per}}(Y;\mathbb{R}^2))$, solutions to the corrector equations

$$\int_Y \mathbf{A}(\mathbf{y})\nabla_y\bar{w}_k^A\cdot\nabla_{\mathbf{y}}\bar{v}(\mathbf{y})\mathrm{d}\mathbf{y} = -\int_Y \mathbf{A}(\mathbf{y})\mathbf{e}_k\cdot\nabla_{\mathbf{y}}\bar{v}(\mathbf{y})\mathrm{d}\mathbf{y}, \tag{6.14a}$$

$$\begin{aligned}\int_Y \left\{\mathbf{A}(\mathbf{y})\nabla_{\mathbf{y}}\bar{w}_k(t,\mathbf{y}) + \int_0^t \left\{\mathbf{B}(\mathbf{y}) + \mathbf{C}(t-s,\mathbf{y})\right\}\nabla_{\mathbf{y}}\bar{w}_k(s,\mathbf{y})\mathrm{ds}\right\}\cdot\nabla_{\mathbf{y}}\bar{v}(\mathbf{y})\mathrm{d}\mathbf{y} \\ = -\int_Y \left\{\mathbf{B}(\mathbf{y}) + C(t,\mathbf{y})\right\}\left\{\mathbf{e}_k + \nabla_{\mathbf{y}}\bar{w}_k^A\right\}\cdot\nabla_{\mathbf{y}}\bar{v}(\mathbf{y})\ \mathrm{d}\mathbf{y},\end{aligned} \tag{6.14b}$$

$$\begin{aligned}\int_Y \left\{\mathbf{A}(\mathbf{y})\nabla_{\mathbf{y}}\bar{w}_k^0(t,\mathbf{y}) + \int_0^t \left\{\mathbf{B}(\mathbf{y}) + \mathbf{C}(t-s,\mathbf{y})\right\}\nabla_y\bar{w}_k^0(s,\mathbf{y})\mathrm{ds}\right\}\cdot\nabla_{\mathbf{y}}\bar{v}(\mathbf{y})\mathrm{d}\mathbf{y} \\ = -\int_Y \mathbf{A}(\mathbf{y})\mathbf{e}_k\cdot\nabla_{\mathbf{y}}\bar{v}(\mathbf{y})\mathrm{dy},\end{aligned} \tag{6.14c}$$

$\forall \bar{v} \in H^1_{\text{per}}(Y)$ and $k \in \{1, \ldots, 6\}$. Here, $H^1_{\text{per}}(Y)$ denotes the space of periodic functions with vanishing mean value. Note that if we decompose $\bar{v}$ into $c_1\bar{v}_1 + c_2\bar{v}_2$ where $\bar{v}_1 = [v_1, 0]$ and $\bar{v}_2 = [0, v_2]$, then each set of equations above decouple into an equation for $\bar{w}_{k,1}$ and one for $\bar{w}_{k,2}$. For example, equation (6.14a) becomes

$$\int_Y \mathbf{A}_{11}(\mathbf{y})\nabla_{\mathbf{y}}\bar{w}^A_{k,1} \cdot \nabla_{\mathbf{y}}\bar{v}_1(\mathbf{y})\ \mathrm{d}\mathbf{y} = -\int_Y \mathbf{A}_{11}(\mathbf{y})\mathbf{e}_{k,1} \cdot \nabla_{\mathbf{y}}\bar{v}_1(\mathbf{y})\mathrm{d}\mathbf{y}$$
$$\int_Y \mathbf{A}_{22}(\mathbf{y})\nabla_{\mathbf{y}}\bar{w}^A_{k,2} \cdot \nabla_{\mathbf{y}}\bar{v}_2(\mathbf{y})\ \mathrm{d}\mathbf{y} = -\int_Y \mathbf{A}_{22}(\mathbf{y})\mathbf{e}_{k,2} \cdot \nabla_{\mathbf{y}}\bar{v}_2(\mathbf{y})\mathrm{d}\mathbf{y},$$

where $\mathbf{A}_{11}$ denotes the first 3×3 block of $\mathbf{A}$ and $\mathbf{e}_{k,1}$ is the first half of $\mathbf{e}_k$, and similarly for $\mathbf{A}_{22}$ and $\mathbf{e}_{k,2}$. The first corrector term $\bar{\mathbf{u}}$, from the expansion

$$\mathbf{u}^\alpha = \mathbf{u}(\mathbf{x}) + \nabla_{\mathbf{y}}\bar{\mathbf{u}}(\mathbf{x}, \mathbf{y}) + \ldots, \tag{6.15}$$

is given as

$$\bar{\mathbf{u}}(t, \mathbf{x}, \mathbf{y}) = \bar{w}^A_k(\mathbf{y})u_k(t, \mathbf{x}) + \int_0^t \bar{w}_k(t - s, \mathbf{y})u_k(s, \mathbf{x})\ \mathrm{d}s + \bar{w}^0_k(t, \mathbf{y})u^0_k(\mathbf{x}), \tag{6.16}$$

where we have considered the decompositions $\mathbf{u}(t, \mathbf{x}) = u_k(t, \mathbf{x})\mathbf{e}_k$ and $\mathbf{u}^0(\mathbf{x}) = u^0_k(\mathbf{x})\mathbf{e}_k$. Rewriting (6.16) in matrix form we have

$$\bar{\mathbf{u}}(t, \mathbf{x}, \mathbf{y}) = \bar{w}^A(\mathbf{y})u(t, \mathbf{x}) + \int_0^t \bar{w}(t - s, \mathbf{y})u(s, \mathbf{x})\ \mathrm{d}s + \bar{w}^0(t, \mathbf{y})u^0(\mathbf{x}),$$

where $\bar{w}^A \in \mathbb{R}^{2\times 6}$ with columns $\{\bar{w}^A_k\}_{k=1}^6$. Similarly $\bar{w}^0, \bar{w} \in \mathbb{R}^{2\times 6}$. Now the expansion (6.15) can be written as

$$E^\alpha_{x_1} = E_{x_1} + \partial_{y_1}\bar{u}_1(\mathbf{x}, \mathbf{y}) + \ldots \tag{6.17a}$$

$$E^\alpha_{x_2} = E_{x_2} + \partial_{y_2}\bar{u}_1(\mathbf{x}, \mathbf{y}) + \ldots \tag{6.17b}$$

$$E^\alpha_{x_3} = E_{x_3} + \partial_{y_3}\bar{u}_1(\mathbf{x}, \mathbf{y}) + \ldots \tag{6.17c}$$

$$H^\alpha_{x_1} = H_{x_1} + \partial_{y_1}\bar{u}_2(\mathbf{x}, \mathbf{y}) + \ldots \tag{6.17d}$$

$$H^\alpha_{x_2} = H_{x_2} + \partial_{y_2}\bar{u}_2(\mathbf{x}, \mathbf{y}) + \ldots \tag{6.17e}$$

$$H^\alpha_{x_3} = H_{x_3} + \partial_{y_3}\bar{u}_2(\mathbf{x}, \mathbf{y}) + \ldots. \tag{6.17f}$$

We now define a new operator

$$\mathcal{L}\mathbf{u}(t, \mathbf{x}) = \mathcal{A}\mathbf{u} + \mathcal{B}\int_0^t \mathbf{u}(s)\ \mathrm{d}s + \int_0^t \mathcal{C}(t - s)\mathbf{u}(s)\ \mathrm{d}s, \tag{6.18}$$

where the 6×6 matrices $\mathcal{A}, \mathcal{B}$ and $\mathcal{C}$ are computed using the solution of system (6.14) as

$$\begin{aligned}
\mathcal{A}_k &= \int_Y \mathbf{A}(\mathbf{y}) \left\{ \mathbf{e}_k + \nabla_{\mathbf{y}} \bar{w}_k^A(\mathbf{y}) \right\} \mathrm{d}\mathbf{y}, \\
\mathcal{B}_k &= \int_Y \mathbf{B}(\mathbf{y}) \left\{ \mathbf{e}_k + \nabla_{\mathbf{y}} \bar{w}_k^A(\mathbf{y}) \right\} \mathrm{d}\mathbf{y}, \\
\mathcal{C}_k &= \int_Y \mathbf{C}(t, \mathbf{y}) \left\{ \mathbf{e}_k + \nabla_{\mathbf{y}} \bar{w}_k^A(\mathbf{y}) \right\} \mathrm{d}\mathbf{y} + \int_Y \mathbf{A}(\mathbf{y}) \nabla_{\mathbf{y}} \bar{w}_k(t, \mathbf{y}) \mathrm{d}\mathbf{y} \\
&\quad + \int_Y \int_0^t \left\{ \mathbf{B}(\mathbf{y}) + \mathbf{C}(t-s, \mathbf{y}) \right\} \nabla_{\mathbf{y}} \bar{w}_k(s, \mathbf{y}) \mathrm{d}s \mathrm{d}\mathbf{y},
\end{aligned}$$

for $k = 1, 2, \ldots, 6$, and where $\mathcal{A}_k, \mathcal{B}_k, \mathcal{C}_k$ are the kth columns of the matrices $\mathcal{A}, \mathcal{B}$, and $\mathcal{C}$, respectively. In the homogenized problem, the electromagnetic field $\mathbf{u}$ is the solution of the system

$$\frac{d}{dt} \mathcal{L}\mathbf{u} = \mathbf{M}\mathbf{u} + \mathbf{J}_s \quad \text{in } (0,T) \times \Omega, \tag{6.20a}$$

$$\mathbf{u}(0, \mathbf{x}) = \mathbf{0} \quad \text{in } \Omega, \tag{6.20b}$$

$$\mathbf{u}_1(t) \times \mathbf{n} = \mathbf{0} \quad \text{on } (0,T) \times \partial\Omega, \tag{6.20c}$$

where $\mathbf{J}_s$ is as defined in (6.12), $\mathbf{M}$ is as defined in (6.11), and $\mathcal{L}$ is as defined in (6.18). We note that if the initial conditions are nonzero, then there is a supplementary source term $\mathcal{J}^0$ that is introduced in the right hand side of (6.20a), which is given to be

$$\mathcal{J}^0(t, \mathbf{x}) = u_k^0(\mathbf{x}) \frac{d}{dt} \left\{ \int_Y \left(\mathbf{A} \nabla_{\mathbf{y}} \bar{w}_k^0(t) + \int_0^t (\mathbf{B} + \mathbf{C}(t-s)) \nabla_{\mathbf{y}} \bar{w}_k^0(s) \, \mathrm{d}s \right) \right\}.$$

See [BGM04] for details.

6.4 Reduction to Two Spatial Dimensions

We now assume our problem to possess uniformity in the x_2-direction. Thus, we assume all derivatives with respect to x_2 (or y_2) to be zero. In this case Maxwell's equations decouple into two different modes, the TE and TM modes. Here, we are interested in the TE_y mode. The TE_y mode involves the components E_x, E_z for the electric field and the component H_y of the magnetic field. We will denote (x, y, z) by (x_1, x_2, x_3). Then equation

(6.13, i) can be written in scalar form as

$$\begin{bmatrix} \partial_t D_{x_1} \\ \partial_t D_{x_2} \\ \partial_t D_{x_3} \\ \partial_t B_{x_1} \\ \partial_t B_{x_2} \\ \partial_t B_{x_3} \end{bmatrix} = \begin{bmatrix} \partial_{x_3} H_{x_2} - J_s \\ \partial_{x_3} H_{x_1} - \partial_{x_1} H_{x_3} \\ \partial_{x_1} H_{x_2} \\ -\partial_{x_3} E_{x_2} \\ -\partial_{x_3} E_{x_1} + \partial_{x_1} E_{x_3} \\ -\partial_{x_1} E_{x_2} \end{bmatrix}, \tag{6.21}$$

with $\mathbf{Lu} = (\mathbf{D}, \mathbf{B})^T$. Recall here that $\mathbf{D}$ is the modified electric flux density, where we have dropped the $\tilde{}$ notation. We may decouple system (6.21) into the TE mode,

$$\begin{bmatrix} \partial_t D_{x_1} \\ \partial_t B_{x_2} \\ \partial_t D_{x_3} \end{bmatrix} = \begin{bmatrix} \partial_{x_3} H_{x_2} - J_s \\ -\partial_{x_3} E_{x_1} + \partial_{x_1} E_{x_3} \\ \partial_{x_1} H_{x_2} \end{bmatrix}$$

and the TM mode

$$\begin{bmatrix} \partial_t B_{x_1} \\ \partial_t D_{x_2} \\ \partial_t B_{x_3} \end{bmatrix} = \begin{bmatrix} -\partial_{x_3} E_{x_2} \\ \partial_{x_3} H_{x_1} - \partial_{x_1} H_{x_3} \\ -\partial_{x_1} E_{x_2} \end{bmatrix}.$$

We assume that our pulse is polarized to only have an x_1-component. In this case the component that is of interest in our problem is the E_{x_1} component.

6.5 Homogenization Model in Two Dimensions

In a similiar manner to the three dimensional case, we may construct matrices $\mathbf{A}^{\mathrm{TE}}$, $\mathbf{B}^{\mathrm{TE}}$, and $\mathbf{C}^{\mathrm{TE}}$ that represent the constitutive relations in two dimensions. Thus the

constitutive matrices are

$$\mathbf{A}^{\mathrm{TE}} = \begin{bmatrix} \mathbf{A}_{11}^{\mathrm{TE}} & 0 \\ 0 & \mu_0 \end{bmatrix}$$

$$\mathbf{B}^{\mathrm{TE}} = \begin{bmatrix} \mathbf{B}_{11}^{\mathrm{TE}} & 0 \\ 0 & 0 \end{bmatrix}$$

$$\mathbf{C}^{\mathrm{TE}} = \begin{bmatrix} \mathbf{C}_{11}^{\mathrm{TE}} & 0 \\ 0 & 0 \end{bmatrix},$$

where

$$\mathbf{A}_{11}^{\mathrm{TE}} = \begin{bmatrix} \epsilon_0\epsilon_r(\mathbf{x}) & 0 \\ 0 & \epsilon_0\epsilon_r(\mathbf{x}) \end{bmatrix}$$

$$\mathbf{B}_{11}^{\mathrm{TE}} = \begin{bmatrix} \sigma(\mathbf{x}) & 0 \\ 0 & \sigma(\mathbf{x}) \end{bmatrix}$$

$$\mathbf{C}_{11}^{\mathrm{TE}} = \begin{bmatrix} \nu(t,\mathbf{x}) & 0 \\ 0 & \nu(t,\mathbf{x}) \end{bmatrix}.$$

The homogenized solution for the TE_y mode is obtained from the formal asymptotic expansion (6.17) as

$$E_{x_1}^{\alpha} = E_{x_1} + \partial_{y_1}\bar{u}_1(\mathbf{x},\mathbf{y}) + \ldots \tag{6.24a}$$

$$E_{x_3}^{\alpha} = E_{x_3} + \partial_{y_3}\bar{u}_1(\mathbf{x},\mathbf{y}) + \ldots \tag{6.24b}$$

$$H_{x_2}^{\alpha} = H_{x_2} + \partial_{y_2}\bar{u}_2(\mathbf{x},\mathbf{y}) + \ldots. \tag{6.24c}$$

Also, since we are assuming uniformity in the x_2 direction we set the term $\partial_{y_2}\bar{u}_2(\mathbf{x},\mathbf{y})$ to zero. So (6.24) becomes

$$E_{x_1}^{\alpha} = E_{x_1} + \partial_{y_1}\bar{u}_1(\mathbf{x},\mathbf{y}) + \ldots$$

$$E_{x_3}^{\alpha} = E_{x_3} + \partial_{y_3}\bar{u}_1(\mathbf{x},\mathbf{y}) + \ldots$$

$$H_{x_2}^{\alpha} = H_{x_2}.$$

Hence the homogenized electric field for the TE_y mode is

$$\mathbf{E}^\alpha = \mathbf{E} + \nabla_{\mathbf{y}} \bar{u}_1(\mathbf{x}, \mathbf{y}) + \ldots,$$

where the gradient operator in this case is $\nabla_{\mathbf{y}} = (\partial_{y_1}, \partial_{y_3})^T$. Therefore we only need to solve for $\bar{u}_1(\mathbf{x}, \mathbf{y})$, which in turn only depends on the first component of $\bar{w}_k^A$, $\bar{w}_k^0$, and $\bar{w}_k$, for $k = 1, 2$.

Let us again denote by Y the reference cell of the periodic structure that occupies $\Omega \subset \mathbb{R}^2$. The construction of the two-dimensional homogenized problem involves solving for the *corrector* subterms $\bar{w}_k^A \in H^1_{\mathrm{per}}(Y; \mathbb{R})$, $\bar{w}_k$ and $\bar{w}_k^0 \in W^{1,1}(0, T; H^1_{\mathrm{per}}(Y; \mathbb{R}))$, solutions to the corrector equations

$$\begin{aligned}
&\int_Y \mathbf{A}_{11}^{\mathrm{TE}}(\mathbf{y}) \nabla_y \bar{w}_k^A \cdot \nabla_{\mathbf{y}} \bar{v}(\mathbf{y}) \mathrm{d}\mathbf{y} = -\int_Y \mathbf{A}_{11}^{\mathrm{TE}}(\mathbf{y}) \mathbf{e}_k \cdot \nabla_{\mathbf{y}} \bar{v}(\mathbf{y}) \mathrm{d}\mathbf{y}, \\
&\int_Y \mathbf{A}_{11}^{\mathrm{TE}}(\mathbf{y}) \nabla_{\mathbf{y}} \bar{w}_k(t, \mathbf{y}) \cdot \nabla_{\mathbf{y}} \bar{v}(\mathbf{y}) \mathrm{d}\mathbf{y} \\
&\qquad + \int_Y \int_0^t \left\{ \mathbf{B}_{11}^{\mathrm{TE}}(\mathbf{y}) + \mathbf{C}_{11}^{\mathrm{TE}}(t-s, \mathbf{y}) \right\} \nabla_{\mathbf{y}} \bar{w}_k(s, \mathbf{y}) \mathrm{d}s \cdot \nabla_{\mathbf{y}} \bar{v}(\mathbf{y}) \mathrm{d}\mathbf{y} \\
&\qquad = -\int_Y \left\{ \mathbf{B}_{11}^{\mathrm{TE}}(\mathbf{y}) + C_{11}^{\mathrm{TE}}(t, \mathbf{y}) \right\} \left\{ \mathbf{e}_k + \nabla_{\mathbf{y}} \bar{w}_k^A \right\} \cdot \nabla_{\mathbf{y}} \bar{v}(\mathbf{y}) \mathrm{d}\mathbf{y}, \\
&\int_Y \mathbf{A}_{11}^{\mathrm{TE}}(\mathbf{y}) \nabla_{\mathbf{y}} \bar{w}_k^0(t, \mathbf{y}) \cdot \nabla_{\mathbf{y}} \bar{v}(\mathbf{y}) \mathrm{d}\mathbf{y} \\
&\qquad + \int_Y \int_0^t \left\{ \mathbf{B}_{11}^{\mathrm{TE}}(\mathbf{y}) + \mathbf{C}_{11}^{\mathrm{TE}}(t-s, \mathbf{y}) \right\} \nabla_y \bar{w}_k^0(s, \mathbf{y}) \mathrm{d}s \cdot \nabla_{\mathbf{y}} \bar{v}(\mathbf{y}) \mathrm{d}\mathbf{y} \\
&\qquad = -\int_Y \mathbf{A}_{11}^{\mathrm{TE}}(\mathbf{y}) \mathbf{e}_k \cdot \nabla_{\mathbf{y}} \bar{v}(\mathbf{y}) \ \mathrm{d}y,
\end{aligned}$$

$\forall \bar{v} \in H^1_{\mathrm{per}}(Y; \mathbb{R})$ and $k = 1, 2$. and $\mathbf{e}_1 = [1, 0]^T, \mathbf{e}_2 = [0, 1]^T$. Once we have solved for the corrector terms, we can then construct the homogenized matrices from

$$\begin{aligned}
(\mathcal{A}_{11}^{\mathrm{TE}})_k &= \int_Y \mathbf{A}_{11}^{\mathrm{TE}}(\mathbf{y}) \left\{ \mathbf{e}_k + \nabla_{\mathbf{y}} \bar{w}_k^A(\mathbf{y}) \right\} \mathrm{d}\mathbf{y}, \\
(\mathcal{B}_{11}^{\mathrm{TE}})_k &= \int_Y \mathbf{B}_{11}^{\mathrm{TE}}(\mathbf{y}) \left\{ \mathbf{e}_k + \nabla_{\mathbf{y}} \bar{w}_k^A(\mathbf{y}) \right\} \mathrm{d}\mathbf{y}, \\
(\mathcal{C}_{11}^{\mathrm{TE}})_k &= \int_Y \mathbf{C}_{11}^{\mathrm{TE}}(t, \mathbf{y}) \left\{ \mathbf{e}_k + \nabla_{\mathbf{y}} \bar{w}_k^A(\mathbf{y}) \right\} \mathrm{d}\mathbf{y} + \int_Y \mathbf{A}_{11}^{\mathrm{TE}}(\mathbf{y}) \nabla_{\mathbf{y}} \bar{w}_k(t, \mathbf{y}) \mathrm{d}\mathbf{y} \\
&\qquad + \int_Y \int_0^t \left\{ \mathbf{B}_{11}^{\mathrm{TE}}(\mathbf{y}) + \mathbf{C}_{11}^{\mathrm{TE}}(t-s, \mathbf{y}) \right\} \nabla_{\mathbf{y}} \bar{w}_k(s, \mathbf{y}) \mathrm{d}s \mathrm{d}\mathbf{y},
\end{aligned}$$

where $\mathbf{e}_k$, $k = 1, 2$ are the basis vectors in $\mathbb{R}^2$, $(\mathcal{A}_{11}^{\mathrm{TE}})_k, (\mathcal{B}_{11}^{\mathrm{TE}})_k$, and $(\mathcal{A}_{11}^{\mathrm{TE}})_k$ are the kth columns of the matrices $\mathcal{A}_{11}^{\mathrm{TE}}, \mathcal{B}_{11}^{\mathrm{TE}}$, and $\mathcal{C}_{11}^{\mathrm{TE}}$, respectively, and the homogenized matrices

are given as

$$\mathcal{A}^{\mathrm{TE}} = \begin{bmatrix} \mathcal{A}_{11}^{\mathrm{TE}} & 0 \\ 0 & \mu_0 \end{bmatrix}$$

$$\mathcal{B}^{\mathrm{TE}} = \begin{bmatrix} \mathcal{B}_{11}^{\mathrm{TE}} & 0 \\ 0 & 0 \end{bmatrix}$$

$$\mathcal{C}^{\mathrm{TE}} = \begin{bmatrix} \mathcal{C}_{11}^{\mathrm{TE}} & 0 \\ 0 & 0 \end{bmatrix}.$$

The corresponding system of equations in the TE_y mode are

$$\begin{aligned} \frac{d}{dt}\mathcal{L}^{\mathrm{TE}}\mathbf{v} = \mathbf{M}^{\mathrm{TE}}\mathbf{v} + \mathbf{J}_s^{\mathrm{TE}} \quad & \text{in } (0,T)\times\Omega, \\ \mathbf{v}(0,\mathbf{x}) = \mathbf{0} \quad & \text{in } \Omega, \\ \mathrm{v}_3 n_{x_1} - \mathrm{v}_1 n_{x_3} = 0 \quad & \text{on } (0,T)\times\partial\Omega, \end{aligned}$$

where $\mathbf{v} = (E_{x_1}, H_{x_2} E_{x_3})^T$, $\mathbf{n} = (n_{x_1}, n_{x_3})^T$ is the unit outward normal vector to $\partial\Omega$, the operator $\mathcal{L}^{\mathrm{TE}}$ is defined as

$$\mathcal{L}^{\mathrm{TE}}\mathbf{u}(t,\mathbf{x}) = \mathcal{A}^{\mathrm{TE}}\mathbf{u} + \mathcal{B}^{\mathrm{TE}} \int_0^t \mathbf{u}(s)\ \mathrm{ds} + \int_0^t \mathcal{C}^{\mathrm{TE}}(t-s)\mathbf{u}(s)\ \mathrm{ds},$$

and M^{TE} is the two-dimensional curl operator

$$\begin{pmatrix} 0 & -\partial_{x_3} & 0 \\ \partial_{x_3} & 0 & -\partial_{x_1} \\ 0 & \partial_{x_1} & 0 \end{pmatrix}.$$

Chapter 7

Conclusions and Futher Directions

In this thesis, we have mainly explored a "proof of concept" formulation of an inverse problem to detect and characterize voids or gaps inside of, or behind, a Dielectric medium. We have simplified the problem to one dimension and used Maxwell's equations to model a pulsed, normally incident electromagnetic interrogating signal. We have successfully demonstrated that it is possible to resolve gap widths on the order of $.2mm$ between a dielectric slab of $20cm$ and a metal (perfectly conducting) surface using an interrogating signal with a $3mm$ wavelength.

Our modified Least Squares objective function corrects for peaks in J which contribute to the ill-posedness. Further, we are able to test on both sides of any detected minima to ensure global minimization. We refer to this procedure as a "check point" method. Although gap widths close to $\frac{\lambda}{8}$ are the most difficult for us to initially estimate, our optimization routine still converged to the correct minimizer in this regime. Ultimately we were able to detect a $.0002m$ wide crack behind a $20cm$ deep slab, however the inverse problem took approximately $10hrs$ to complete.

Future work on this problem will require a better characterization of the material in question (in our case, foam). Experiments must be performed, and data collected, to learn more about the physical problem and to accurately estimate the parameters involved. Further, more sophisticated models for describing the polarization mechanisms in non-homogeneous materials must be developed. Toward this end we discussed here two modeling approaches to deal with heterogeneous materials: homogenization and distribu-

tions of parameters.

Homogenization techniques attempt to replace spatially periodic parameters by new effective constant parameters. We discussed current efforts in this field and presented the equations necessary to solve in order to determine these homogenized parameters. Once these equations are solved, the parameters may be inserted into existing simulators of Maxwell's equations and tested against actual data.

Regarding the distributions of parameters, we demonstrated with examples the necessity in some cases of multiple polarization parameters (i.e., a discrete distribution with multiple atoms), specifically multiple relaxation times for a heterogeneous Debye medium. Further, we presented a parameter identification problem to determine a general polarization term which includes uncertainty in the dielectric parameters. We demonstrated the well-posedness of this inverse problem by use of the Prohorov metric. Using the theory as a basis for our computational method, we solved several examples of the parameter identification problem in the context of a Debye polarization model, in particular a discrete distribution with two atoms, as well as a simple uniform distribution of relaxation times.

Future research may require either, or both, of homogenizations and the use of distributions of parameters for proper modeling of the dielectric and polarization mechanisms involved in heterogenous materials. Also, in order to take scattering and non-normally incident electromagnetic signals into account, higher dimensional models will be necessary. However higher dimensional models will require even more computational time, and currently the inverse problem involving a $20cm$ slab already takes too long to be practically useful. Additional modeling approaches, such as the use of Green's functions, need to be developed to avoid computationally expensive time stepping methods. Lastly, any models developed and computational techniques used must be validated against data in appropriately designed experiments.

Bibliography

[ABBS03] B. M. Adams, H. T. Banks, J. E. Banks and J. D. Stark, *Population Dynamics Models in Plant-Insect Herbivore-Pesticide Interactions*, CRSC Technical Report CRSC-TR03-12, North Carolina State University, August, 2003.

[BB01] H. T. Banks and K. L. Bihari, *Modeling and Estimating Uncertainty in Parameter Estimation*, Inverse Problems, 17 (2001), pp. 95-111.

[BBPP03] H. T. Banks, D. M. Bortz, G. A. Pinter, L. K. Potter, *Modeling and Imaging Techniques with Potential for Application in Bioterrorism*, CRSC Technical Report CRSC-TR03-02, North Carolina State University, January, 2003; Chapter 6 in *Bioterrorism: Mathematical Modeling Applications in Homeland Security*, (H.T. Banks and C. Castillo-Chavez, eds.), SIAM Frontiers in Applied Math, FR28, pp. 129-154, SIAM, Philadelphia, 2003.

[BBL00] H. T. Banks, M. W. Buksas, and T. Lin, *Electromagnetic Material Interrogation Using Conductive Interfaces and Acoustic Wavefronts*, SIAM: Frontiers in Applied Mathematics, Philadelphia, 2000.

[BG04] H. T. Banks and N. L. Gibson, *Well-Posedness in Maxwell Systems with Distributions of Polarization Relaxation Parameters*, CRSC Technical Report CRSC-TR04-41, NCSU, January, 2004; Applied Math Letters, to appear.

[BGW03] H. T. Banks, N. L. Gibson, and W. P. Winfree, *Electromagnetic Crack Detection Inverse Problems using Terahertz Interrogating Signals*, CRSC Technical Report CRSC-TR03-40, North Carolina State University, October, 2003.

[BK89] H. T. Banks and K. Kunisch, *Estimation Techniques for Distributed Parameter Systems*, Birkhäuser, Boston, 1989.

[BP04] H. T. Banks and G. A. Pinter, *A Probabilistic Multiscale Approach to Hysteresis in Shear Wave Propagation in Biotissue*, CRSC Technical Report CRSC-TR04-03, North Carolina State University, January, 2004.

[BSW96] H. T. Banks, R. C. Smith, and Y. Wang, *Smart Materials Structures Modeling, Estimation and Control*, Masson, Paris, 1996.

[B68] P. Billingsley, *Convergence of Probability Measures*, Wiley, New York, 1968.

[BGM04] A. Bossavit, G. Griso, and B. Miara, *Modelling of Periodic Electromagnetic Structures Bianisotropic Material with Memory Effects*, in preparation, 2004.

[BB78] C. J. F. Böttcher and P. Bordewijk, *Theory of Electric Polarization, Volume II*, Elsevier, New York, 1978.

[BF93] R. L. Burden and J. D. Faires, *Numerical Analysis*, PWS, Boston, 1993.

[CD99] D. Cioranescu and P. Donato, *An Introduction to Homogenization*, Number 17 in Oxford Lecture Series in Mathematics and its Applications, Oxford University Press, 1999.

[CDG04] D. Cioranescu, A. Damlamian, and G. Griso, *Periodic Unfolding and Homogenization*, in preparation, 2004.

[DG95] M. Davidian and D. M. Giltinan, *Nonlinear Models for Repeated Measurement Data*, Chapman and Hall: Monographs on Statistics and Applied Probability 62, New York, 1995.

[E93] R. S. Elliot, *Electromagnetics: History, Theory and Applications*, IEEE Press, New York, 1993.

[ES04] C. Engström and D. Sjöberg. *A comparison of two numerical methods for homogenization of maxwell's equations*, Technical Report LUTEDX/(TEAT-7121)/1-10/(2004), Department of Electroscience, Lund Institute of Technology, Sweden, 2004.

[J95] C. Johnson, *Numerical Solution of Partial Differential Equations by the Finite Element Method*, Cambridge University Press, New York, 1995.

[K99] C. T. Kelley, *Iterative Methods for Optimization*, SIAM: Frontiers in Applied Mathematics, Philadelphia, 1999.

[K01] G. Kristensson, *Homogenization of the Maxwell Equations in an Anisotropic Material,* Technical Report LUTEDX/(TEAT-7104)/1-12/(2001), Department of Electroscience, Lund Institute of Technology, Sweden, 2001.

[K04] G. Kristensson, *Homogenization of Corrugated Interfaces in Electomagnetics*, Technical Report LUTEDX/(TEAT-7122)/1-29/(2004), Department of Electroscience, Lund Institute of Technology, Sweden, 2004.

[L71] J. L. Lions, *Optimal Control of Systems Governed by Partial Differential Equations*, Springer-Verlag, New York, 1971.

[M03] D. Mittleman, *Sensing with Terahertz Radiation*, Springer-Verlag, New York, 2003.

[MM94] K. W. Morton and D. F. Mayers, *Numerical Solution of Partial Differential Equations*, Cambridge University Press, 1994.

[QSS00] A. Quarteroni, R. Sacco, and F. Saleri, *Numerical Mathematics*, Springer, 2000.

[S04] D. Sjöberg, *Homogenization of Dispersive Material Parameters for Maxwell's Equations using a Singular Value Decomposition*, Technical Report LUTEDX/(TEAT-7124)/1-24/(2004), Department of Electroscience, Lund Institute of Technology, Sweden, 2004.

[SEK03] D. Sjöberg, C. Engström, G. Kristensson, D. J. N. Wall, and N. Wellander, *A Floquet-Bloch Decomposition of Maxwell's Equations, Applied to Homogenization*, Technical Report LUTEDX/(TEAT-7119)/1-27/(2003), Department of Electroscience, Lund Institute of Technology, Sweden, 2003.

[S92] W. A. Strauss, *Partial Differential Equations*, Wiley, 1992.

[WK02] N. Wellander and G. Kristensson, *Homogenization of the Maxwell Equations at Fixed Frequency*, Technical Report LUTEDX/(TEAT-7103)/1-38/(2001), Department of Electroscience, Lund Institute of Technology, Sweden, September 2002.

[W92] J. Wloka, *Partial Differential Equations*, Cambridge University Press, 1992.